Spring 1-1-2013

Electrostatic In ation of Membrane Space Structures

Laura Ann Stiles
University of Colorado at Boulder, lastiles@gmail.com

Electrostatic Inflation of Membrane Space Structures

by

Laura A. Stiles

B.S., Engineering Physics, University of Kansas, 2008

M.S., Aerospace Engineering, University of Colorado, 2011

A thesis submitted to the

Faculty of the Graduate School of the

University of Colorado in partial fulfillment

of the requirements for the degree of

Doctor of Philosophy

Department of Aerospace Engineering Sciences

2013

This thesis entitled:
Electrostatic Inflation of Membrane Space Structures
written by Laura A. Stiles
has been approved for the Department of Aerospace Engineering Sciences

Prof. Hanspeter Schaub

Prof. Zoltan Sternovsky

Prof. Kurt Maute

Prof. Dejan Filipovic

Dr. Daniel Moorer

Date

The final copy of this thesis has been examined by the signatories, and we find that both the content and the form meet acceptable presentation standards of scholarly work in the above mentioned discipline.

Stiles, Laura A. (Ph.D., Aerospace Engineering Sciences)

Electrostatic Inflation of Membrane Space Structures

Thesis directed by Prof. Hanspeter Schaub

Membrane space structures provide a lightweight and cost effective alternative to traditional mechanical systems. The low-mass and high deployed-to-stored volume ratios allow for larger structures to be launched, expanding on-orbit science and technology capabilities. This research explores a novel method for deployment of membrane space structures using electrostatic pressure as the inflation mechanism. Applying electric charge to a layered gossamer structure provides an inflationary pressure due to the repulsive electrostatic forces between the charged layers. The electrostatic inflation of membrane structures (EIMS) concept is particularly applicable to non-precision structures such as sunshields or drag de-orbiting devices. This research addresses three fundamental topics: necessary conditions for EIMS in a vacuum, necessary conditions for EIMS in a plasma, and charging methods.

Atmospheric and vacuum demonstrations show that less than 10 kiloVolts are required for electrostatic inflation of decimeter scale membrane structures in 1-g. On-orbit perturbation forces can be much smaller than the limiting 1-g, suggesting feasible voltage requirements. Charge distributions are numerically determined for the different configurations enabling a relationship between required inflation pressure (to offset disturbances) and required voltage. It was found that 100's of Volts are required to offset orbital pressures to maintain inflation in geosynchronous orbits (GEO) and a few kiloVolts in low Earth orbit (LEO).

While GEO plasma has only a small impact on the EIMS performance, Debye shielding at LEO reduces the electrostatic pressure. Through numerical simulation, it is found that the classic Debye shielding prediction is far worse than actual shielding, raising the 'effective' Debye length to the meter scale in LEO as opposed to centimeter levels, aiding feasibility of EIMS in LEO. Interesting electro-mechanical interactions were discovered between EIMS and the charge

flux which are concluded to be a result of coupling between changing electrostatic fields and the flow of electrons, though the structure remains inflated.

Charged particle emission and remote charging methods are explored as inflation mechanisms. Secondary electron emission characteristics of EIMS materials were determined experimentally. Nonlinear fits to the Sternglass curve determined a maximum yield of 1.83 at 433 eV for Aluminized Kapton and a maximum yield of 1.78 at 511 eV for Aluminized Mylar. Remote charging was demonstrated to -500 V with a 5 keV electron beam. Charge emission was also determined a feasible charging method, with power levels below 1 Watt in GEO and from 10's of Watt to a kiloWatt in LEO.

Acknowledgements

I would like to first thank my research advisor and mentor, Dr. Hanspeter Schaub. You have been an inspiration to me in your dedication to teaching and research. I feel extremely lucky to have worked with you and appreciate all you have done: with helping to see the potential in this research topic, providing guidance throughout the work, always answering questions with extreme efficiency and also being supportive and caring regarding everything beyond school and research. Thank you to Dr. Zoltan Sternovsky for providing research direction, guidance on building and executing the experiments, and answering my somewhat endless questions. Being able to work with you and the extremely helpful students at the NPL (Keith, Anthony, Mark, Andrew) made me look forward to the days in the lab. Thank you also to the other members of my committee: Dr. Kurt Maute, Dr. Daniel Moorer, and Dr. Dejan Filipovic. I deeply appreciate your time and the input that you have provided throughout this research.

A huge amount of gratitude goes to the undergraduate research assistants that have worked with me over the years. I hope that each of you got as much out of the experience as I did. Nic Zinner: you were critical to get first experiments off the ground. Thank you for your ideas and hard work. Jack Mills: thank you for the hard work on the (often tedious) experiments through the charge shielding project and also for understanding and sharing my tendency to be late and to prioritize the need for food. Matt Holmes: I wouldn't have been able to do the remote charging experiment without you. You have a keen eye for hardware design and were always asking important questions to contribute to this project. I feel lucky to have had the opportunity to work with all 3 of you. Thank you also to the other students of the AVS lab: for those days of sitting and staring at

equations on the white board, the input on presentations and papers (especially the tough questions in research group meetings), and for good company everyday in the lab.

Endless thanks go to my friends that have supported me through this chapter of my life. To the skydivers, climbing/hiking/skiing/biking partners, and intramural teammates: thank you for joining me in the outlets that keep me sane and keep my passion for life alive. Thank you to the friends who told me I could when I doubted myself, listened when I needed shoulder to lean (or cry) on, and grabbed a beer with me when life became too crazy.

Last but not least, my family. I have had more support than anyone could ask for from my parents and grandparents, who always go out of their way to help and encourage me. To my mom for her endless encouragement in learning (from quizzing me with spelling words in elementary school to pretending to be interested in heavy ion collisions at my talks), her caring heart, and all the cards in the mail telling me how proud she is. To my Dad for helping me to find this path (from watching meteor showers in kindergarten to finding the right undergraduate major), sharing in my love for bikes, the outdoors, building things, and Led Zeppelin, and for being an inspiration to me. And my sister, who provides comfort in knowing that I can talk to her about anything and would never be judged.

This research was funded by the National Science Foundation's Graduate Research Fellowship, the GAANN fellowship, and the NASA Advanced and Innovative Concepts program. Thank you also to the Zonta International organization who supported my tenure through the Amelia Earhart Fellowship program and the P.E.O. Women's organization for support from the Scholar Award.

Contents

Chapter

Tables

Table

Figures

Figure

Chapter 1

Introduction

1.1 Motivation

Gossamer spacecraft structures have enabled consideration of much larger and lower mass structures on-orbit than traditional mechanical systems allow. The low-mass and high deployed-to-stored volume ratios help expand on-orbit science and technology capabilities in a wide range of applications. Gossamer is a general term for several classes of space structures, such as expandable composite booms[3], membrane sails[4], inflatable solar arrays[5], or space habitats[6]. Here, a subset of gossamer structures, inflatable structures, is considered for which many different applications have been explored and a select few have been successfully employed in space.

Examples of early work on inflatable structures include the development of the mylar ECHO balloons in 1958 at NASA. The ECHO I sphere, which was launched in 1960, successfully served as a communications reflector in space for several months[7]. L'Garde Inc. made early contributions to the field of deployable technology, including the support for NASA to the launch an inflatable antenna from the Space Shuttle[8], shown in Figure 1.1(a). An example of present day inflatable gossamer structure research is the Global Aerospace's Gossamer Orbit Lowering Device (GOLD) concept for drag augmentation devices for satellite de-orbit, as illustrated in Figure 1.1(b). The variety in applications of these inflatable structures demonstrates a broad utility of lightweight technologies.

Common methods for deployment of inflatable gossamer structures include inflation via pressurized gas from tanks, sublimating chemicals, or evaporating liquids[9]. This research explores a

(a) L'Garde gas inflatable antenna experiment demonstration (lgarde.com)

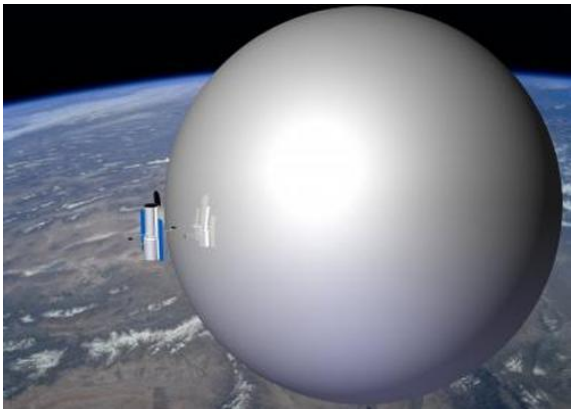

(b) GOLD Gossamer Orbit Lowering Device concept (gaerospace.com)

Figure 1.1: Examples of inflatable gossamer structures in recent research

novel inflation method for a membrane space structure which uses electrostatic repulsion to create inflationary forces. Applying absolute electric charge to a layered gossamer structure provides an inflationary pressure due to the repulsive electrostatic forces between the charged layers, as per Coulomb's law. The electrostatic pressure inflates the membranes to a stable structure, much like inflation of an airbag with gas. The separation distance due to inflation of the membranes can be constrained by an internal membrane structure. In contrast to gas-inflated structures, the electrostatically inflated membrane structure (or EIMS) does not suffer from sensitivities to membrane punctures from orbital debris and micrometeorites or the requirement to be a closed structure. The membrane structures considered for EIMS are open-ended membrane structures resembling in one configuration the ribbed, open structure of a ram-air parachute than that of a fully enclosed balloon. Electrostatic inflation of a membrane space structure is illustrated in Figure 1.2.

The electrostatic inflation concept is particularly applicable to non-precision structures such as sunshields or drag augmentation devices for de-orbiting and space debris avoidance purposes. Further, Tripathi discusses in Reference 10 using large, charged space structures to perform active radiation shielding to protect humans during space flight. Here, the EIMS concept would enable novel structural solutions where charging is used both for active radiation shielding as well as

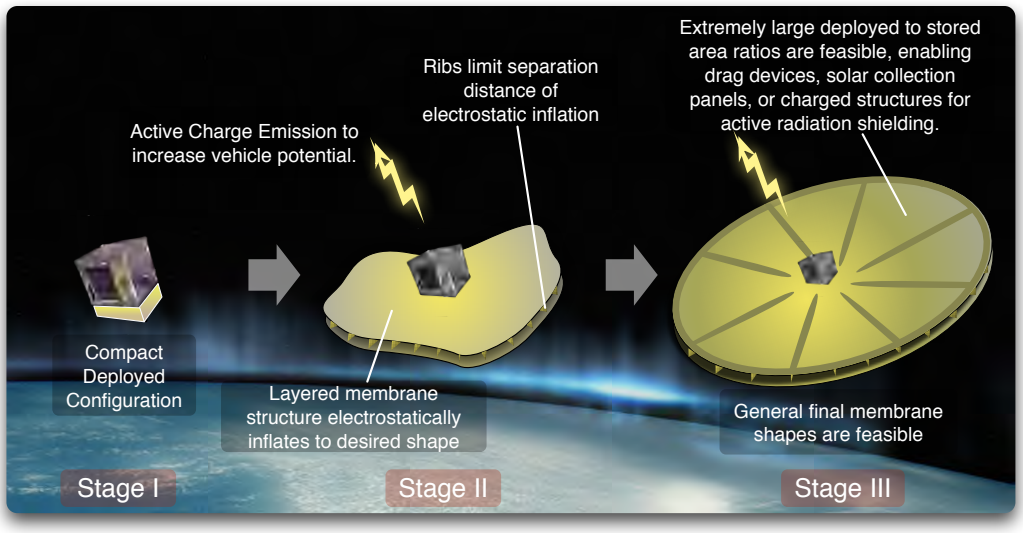

Figure 1.2: Illustration of Electrostatically Inflated Membrane Structure (EIMS) concept

providing lightweight membrane structure shape stability. Application of the electrostatic inflation concept for these and other space apertures presents the potential to significantly decrease overall mass, while reducing the associated deployment-oriented power and packaging volume for lightweight deployable structures. A large ratio of deployed volume to stowed volume is very advantageous, especially in highly volume-constrained spacecraft such as Nanosats or CubeSats.

There are many challenges, however, associated with electrostatic inflation. The challenges range across many fields of engineering and science, thus requiring a broad spectrum of research to address even the most fundamental challenges. Some of the top-level challenges include:

- Space plasma interactions such as Debye shielding which weaken electrostatic forces
- Modeling plasma conditions and the interactions with changing charge distributions on moving structures
- Non-linear structural modeling of thin membrane materials coupled with the electrostatic solution
- Requirement of microgravity and a plasma chamber for realistic testing environment
- Material challenges including membrane wrinkling and tearing

The contribution of this research is to address the most fundamental questions related to the concept of electrostatic inflation. As there does not exist literature beyond conceptual discussion of electrostatic inflation, a multitude of avenues for research exist. There are many topics which remain to be answered in future research.

1.2 Electrostatic Inflation of Membrane Space Structures

Electrostatic inflation is a novel method for the deployment and shape maintenance of gossamer spacecraft structures. The pressure for deployment or maintaining a desired shape is provided by repulsive forces between electrostatically charged layers of membrane materials. This is illustrated in Figure 1.3 for one of the shape concepts explored within the scope of this research.

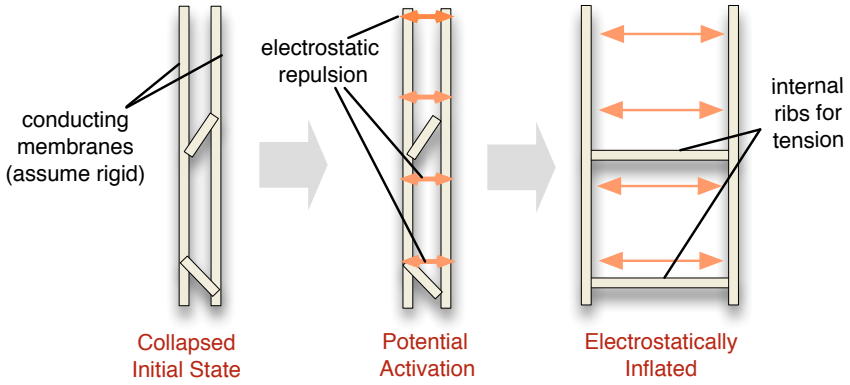

Figure 1.3: Simplified open-ended membrane rib structure undergoing electrostatic inflation

In contrast to many membrane space structures, no external tensioning system is required. The electrostatic pressure is envisioned as the sole mechanism to deploy the structure from a compact stowage for launch and maintain a desired, functional shape. Before changing the electrostatic potential of the membrane structure (through mechanisms such as charged particle emission or a remote charging beam), there is no stiffness to the body to maintain a desired shape. When the absolute potential has been raised, the electrostatic charge distributed across a layered structure results in electrostatic forces acting between the layers of the conducting material. These forces result in inflation pressure, similar to gas inflation, to unroll, unfold, or inflate a membrane structure.

Membrane materials have proven to be challenging for precision spacecraft applications and an external tensioning system may be required for precision applications (such as a mirror or antenna). The electrostatic inflation concept with no external tensioning, therefore, is most applicable to non-precision structures such as sunshields or drag augmentation devices for de-orbiting and space debris avoidance purposes. These applications do not typically have requirements for surface accuracy, they simply require a large surface area to increase drag or block solar radiation. EIMS can provide an extremely lightweight and compact method to enable these types of large structures on-orbit.

1.2.1 Prospects

The electrostatic inflation method benefits from many of the same advantages of a traditional gossamer system, particularly mass and volume savings. These two parameters (mass and volume) are top system drivers for designing a spacecraft.[11] Mass and volume savings in the structural subsystem of the spacecraft allow for larger spacecraft components and instruments to be packaged for launch, and having larger apertures on-orbit is critical in many science and engineering scenarios. For science purposes, larger mirrors on telescopes allow imaging objects at greater distances, solar sails can achieve further distances due to the larger surface area, and larger sun shields can allow larger instruments that need to be kept cold for operation.[2] For engineering, larger solar arrays generate great power and larger antenna enable high communication rates or communication over larger distances.

The cost of launching to orbit is $4,440 per pound to low Earth orbit and $17,032 per pound to a geosynchronous transfer orbit (on average over the last decade for a Western launch vehicle).[12] Due to this steep cost, it is critical to reduce mass wherever possible on a spacecraft system. The mass savings from employing an EIMS system comes from replacing traditional solid spacecraft parts with electrostatic inflatable structures. The James Webb Space Telescope (JSWT), for example, has a large sunshield to cool the instrument which requires booms, spreader bars, and cabling to deploy and tension the system[13]. The sub-components account for the majority of

the mass of the sunshield system, as the shield itself is extremely lightweight aluminized Kapton. Aluminized Kapton or aluminized Mylar are the materials which will be used for electrostatic inflation. The materials are extremely thin, on the order of tens of microns, therefore do not add significant mass to the system. Elimination of the deployment and tensioning mechanisms and replacement with electrostatically inflated structures could significantly reduce the overall mass of a subsystem such as a deployable sunshield.

Even the largest launch vehicles, such as the Atlas V and the Falcon Heavy, are highly volume constrained with only 4.57 and 4.60 meters (respectively) of usable diameter [14,15]. Any spacecraft, therefore, that has an on-orbit configuration larger than these restrictions must have some form of a deployment mechanism. Traditional deployable gossamer structures offer volume savings but often require an external tensioning system, such as the JSWT system. EIMS does not require an external tensioning system, which provides further mass savings and also allows more flexibility in the packaging of the structure, helping to meet tight launch volume constraints. Laboratory demonstrations of electrostatic inflation showed volume expansion in prototypes of multiple orders of magnitude.

1.2.2 Challenges

There are many challenges associated with gossamer structures in all phases of design, build, test, and flight. The gossamer materials which are considered for EIMS (metal coated polymer sheets) are extremely thin and delicate materials, causing challenges from structural modeling to handling and packaging. On-orbit, EIMS can suffer from interactions with the space plasma and on the ground, inflation is extremely inhibited by gravity. Some of these challenges are addressed in this research and are highlighted below. Other challenges, such as deployment dynamics or thermal stresses, are left for future work.

The gossamer materials which are used for EIMS are of thicknesses on the order of tens of microns. Due to the thinness, these materials require extreme delicacy in handling to avoid material tears. The materials are also very susceptible to wrinkling due to the little compression and bending

resistance.[16] Wrinkles in the material (as can be seen in Figure 1.4) can have a significant effect on the structure's shape and behavior. Both of these factors must be taken into account for the packaging and deployment of a gossamer structure.

Figure 1.4: L'Garde Solar Sail (lgarde.com)

The nature of a gossamer material (particularly the metal coated plastic films of an EIMS) makes finite element modeling a challenge. Displacements are large and material properties are non-linear[9]. Using the approach of shell elements (flat elements combining bending element and membrane element) has allowed improved modeling of such structures[17]. EIMS presents an additional challenge for structural modeling, as the coupled problem of electrostatics and structural mechanics must be solved simultaneously. While commercial code is available to solve ranges of multi-physics problems, they were not well suited for the challenging, non-linear membrane problem of interest. Another challenge for modeling EIMS or any membrane structure is capturing the effect of wrinkles. Reference 16 provides an overview of several methods which tend to fall into two groups: deformation tensor modification and stiffness/compliance modification. The advanced topic of modeling membrane wrinkles is, however, beyond the scope of this dissertation. Another challenge is understanding the dynamics of the flexible EIMS system. Understanding the dynamics is important for attitude maneuvering and control and can be challenging for a large flexible spacecraft component. Depending on the natural frequency of the flexible system and the rigid components, the effects of external forces can be greatly varied and an uncontrolled flexible com-

ponent can add energy to the system. For fully understanding the effects of a flexible spacecraft, computer simulation of an extended time is required [18]. This study falls beyond the scope of this dissertation.

In the testing phase of a gossamer structure, the issue of gravity arises. An inflatable structure, such as EIMS, is not designed to have inflation capabilities to overcome the 1-g forces on earth. The ability to realistically test deployment, therefore, requires a reduced gravity environment (such as a microgravity aircraft flight or sub-orbital flight). As many reduced gravity test options are both limited in availability and expensive, other methods must be considered. One option is a gravity off-loading system, such as the system described in Reference 19. An off-loading system, however, can interfere with the structural behavior. Alternatively, for electrostatic inflation, small scale prototypes can be used which have a larger deployment force to area ratio (due to higher charge densities). Also, configurations were designed to test electrostatic inflation in a horizontal direction to avoid overcoming gravity. In addition to the necessity of microgravity, a vacuum environment is also required for EIMS testing, as the charged membranes suffer from interactions with the air.

In the plasma environment of space, electrons and ions rearrange in the presence of a disturbing electric field to maintain macroscopic neutrality [20]. This phenomena, known as Debye shielding, will effectively shield the electrostatic potential of a charged object in a plasma, such as an charged membrane structure. In the Low Earth Orbit region, Debye lengths are typically on the order of milli- or centimeters, depending on the orbit altitude. If the separation distance between the layers of membrane in a gossamer structure in LEO is greater than a few centimeters, or on the order of the local Debye length, then the membranes may not experience a significant electrostatic force and the inflation concept would not be feasible. Numerical simulations described in the fourth chapter, however, show that actual Debye shielding is less than classically predicted when high voltages are employed. Large membrane separation distances, though, will still be challenging in this orbit regime. In the GEO regime, the Debye length is generally on the order of hundreds of meters. The small separation distances between proposed membrane structures compared to

the large Debye lengths yield nearly negligible effects from the shielding, and the field decreases proportional to the $1/r^2$ vacuum electrostatic field dropoff. This is true even for the very worst GEO plasma weather conditions. In addition to Debye shielding, the plasma interaction with the electrostatically charged membrane may cause complexities. Charge flux experiments (described in Chapter 4) demonstrate that the interactions are hard to predict. Advanced numerical plasma simulation will be required in the future to understand this dynamic scenario.

1.3 Literature Review

A review of relevant literature is presented in this section. The review is divided into two categories: membrane structures (including traditional inflatable structures) and Coulomb spacecraft applications.

1.3.1 Membrane Structures

Membrane space structures are a class of lightweight structures which encompasses many different architectures. This class of structures, also referred to as gossamer structures, can offer significant savings in weight and packaging volume in comparison to solid, rigid structures. When considering small spacecraft platforms, such as the CubeSat, mass and volume are critical design components. Deployable membrane structures allow the opportunity for large apertures which can still meet tight mass and volume constraints. Membrane structures have been used for applications such as solar sails, sunshades, reflectors, and inflatable habitats. Examples of various applications of membrane structures are presented and discussed.

One current area of development of membrane spacecraft is solar sail technology. A solar sail is a spacecraft that uses radiation pressure from a star as a form of propulsion, a concept dating back to 1865[21]. There are several on-going missions for solar sails, some of which have successfully launched. Launched in 2008, NASA's NanoSail-D mission would have been the first on-orbit demonstration of sail deployment[22]. Though the spacecraft was lost due to an unsuccessful Falcon rocket launch, the spare (Nanosail-D2) was successfully launched in 2010 and demonstrated

the de-orbit capabilities of a solar sail. Also in 2010, the first interplanetary solar power sail, IKAROS, was successfully launched and deployed. IKAROS (Interplanetary Kite-craft Accelerated by Radiation Of the Sun) is a project from the Japanese Space Agency (JAXA). The IKAROS project provided a multitude of information about membrane space structures, including topics such as folding techniques [23] and membrane dynamics [24] which will be important for future applications of membrane structures.

Another important application of a membrane structure is a solar shade (or thermal shield) for a spacecraft. Here, a surface is used to block radiation from the sun from reaching the spacecraft or spacecraft instrument either as a thermal shield or to decrease noise (stray light) in an optical instrument. A thermal shield can be created from just a few layers of metal-coated polymer films [9]. One current example of a membrane sunshade is the James Webb Space Telescope (JWST) shade, seen in Figure 1.5 This telescope has a large sunshield consisting of several layers of silicon-coated Kapton which is used to reflect the heat of the sun, keeping the telescope cool. The layers of Kapton are mechanically tensioned to maintain the desired shape.

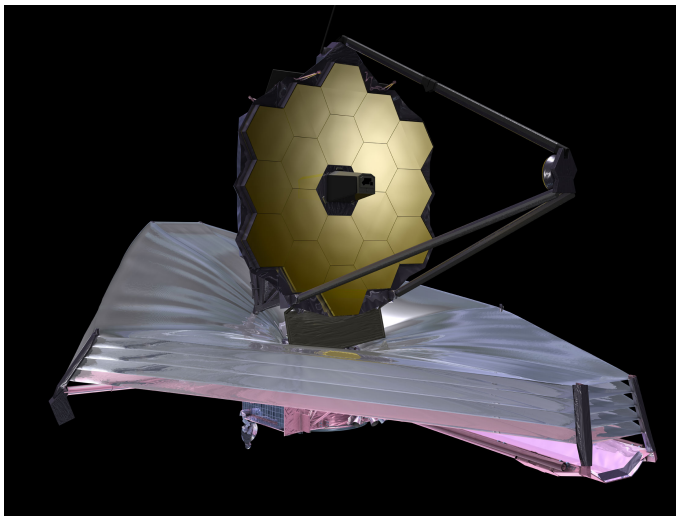

Figure 1.5: James Webb Space Telescope

Within the class of membrane structures are inflatable space structures. Inflatable space

[1] www.jwst.nasa.gov/images

Figure 1.6: NASA's PAGEOS inflated sphere (nasa.gov)

structures have extremely high deployed-to-stored volume ratios, allowing for very large apertures on-orbit. Common methods for deployment of inflatable structures include inflation via tanks of pressurized gas, sublimating chemicals, or evaporating liquids [9].

A first example of an inflatable membrane space structure is the ECHO balloon satellite project. The ECHO I sphere, which was launched in 1960, successfully served as a communications reflector in space for several months. ECHO II was a similar design, but larger than the ECHO I with a diameter of 41.1 m compared to the 30.5 m diameter of ECHO I. The balloons were constructed of aluminum deposited Mylar film that was 12.7 microns thick. The ECHO project was one of the first demonstrations of the capabilities of inflatable structures.

A similar project from NASA in the 1960s, the Passive Geodetic Earth-Orbiting Satellite (PAGEOS), is shown in Figure 1.6. PAGEOS carried no instruments, as it was only meant to be a reflective surface in orbit for triangulation and mapping purposes. The material used was

the same as the ECHO balloons and the sphere was the same size at ECHO I. The sphere was constructed from 84 gores of the aluminized Mylar each sealed together with tape and folded with pleats and accordion folds[25]. The inflated volume was 14838 m^3, but the packaged volume was only .14 m^3, an increase of seven orders of magnitude[25]. The inflation was accomplished with a chemical reaction between benzoic acid and anthraquinone, producing gas for inflation. The two solids were held in a canister with an explosive device for opening, with an inflation system mass of approximately 18 kg[25].

Another important mission in the development of inflatable space technology was L'Garde Inc.'s Inflatable Antenna Experiment (IAE). Made of the same aluminized Mylar material as the ECHO and PAGEOS balloons, the antenna consisted of a 14 m parabolic dish, an inflated support ring, and inflatable struts approximately 33 m long. The IAE was launched from the space shuttle (STS-77) and although there were complications with the inflation and the dynamics, was considered an overall success[26]. Complications with inflation were caused by some residual gas in the membrane structure and higher than expected strain energy upon deployment of the torus. The antenna, however, completed inflation at approximately 3 psi.[26]. The IAE was not only technically important, as much was learn about inflating large structures on orbit, but important also for motivating the field of inflatable and deployable structures.

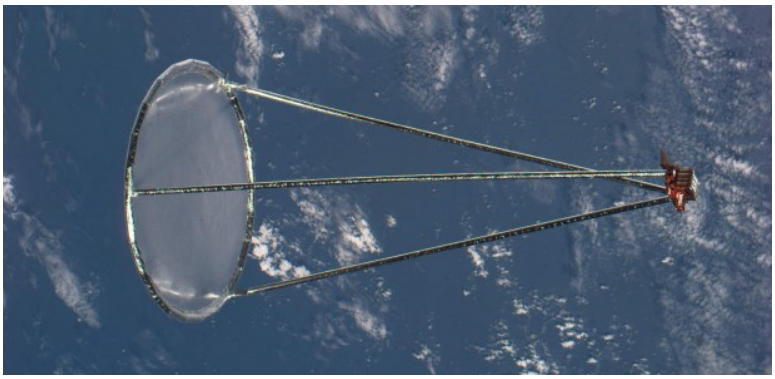

Figure 1.7: Inflatable Antenna Experiment deployed on-orbit (lgarde.com)

A last example application of a membrane inflatable structure is a drag/de-orbiting device for

a low-Earth orbit satellite. With this concept, the surface area of the satellite is greatly increased at the end-of-life in order to increase the atmospheric drag force. The increase in atmospheric drag slowly decreases the along-track orbital velocity and thus decreases orbital altitude. A drag device helps to expedite the natural re-entry process into the Earth's atmosphere in order to meet satellite de-orbit time requirements. De-orbit requirements apply to all satellites launched into orbit by any organization with the objective of limiting potentially hazardous orbital debris in important and increasingly congested orbits. An inflated membrane structure to increase the surface area and drag profile for a satellite is an attractive choice due to the small mass and volume for storing the end-of-life system. Additionally, reference 27 shows that when using the area-time product risk analysis for debris removal methods, an inflation-maintained ultra-thin envelope has the lowest risk of creating new debris (beyond using the satellite's propulsion system). One proposed concept for a drag device from the Global Aerospace Corporation is the Gossamer Orbit Lowering Device (GOLD), shown in Figure 1.8. The GOLD device has the potential to reduce orbit decay time by orders of magnitude for satellites in orbits up to 1,200 km.[28] The device could be attached before launch (as is describe in detail in U.S. Patent 6,830,222[29]) or attached via a separate robotic servicing satellite.

These and many other missions with membrane or inflatable membrane structures have provided technical background for materials, packaging, deployment dynamics, etc. that help to guide the design of electrostatically inflated membrane structures.

1.3.2 Coulomb and Electromagnetic Structures

The concept of electrostatic forces for control of space structures has been studied for many decades. Previous research has focused on using electrostatics to precisely control the shape of single-layer membrane surfaces whose outer edges are held in place by a rigid structure. A US patent by J.H. Cover filed in 1966 describes an invention for using electrostatics to control the surface of a reflector dish in space[1]. Here, a mesh made of thin conductors (aluminum coated quartz fibers suggested) is connected to a rigid ring with a similar mesh in proximity. When charged, electrostatic

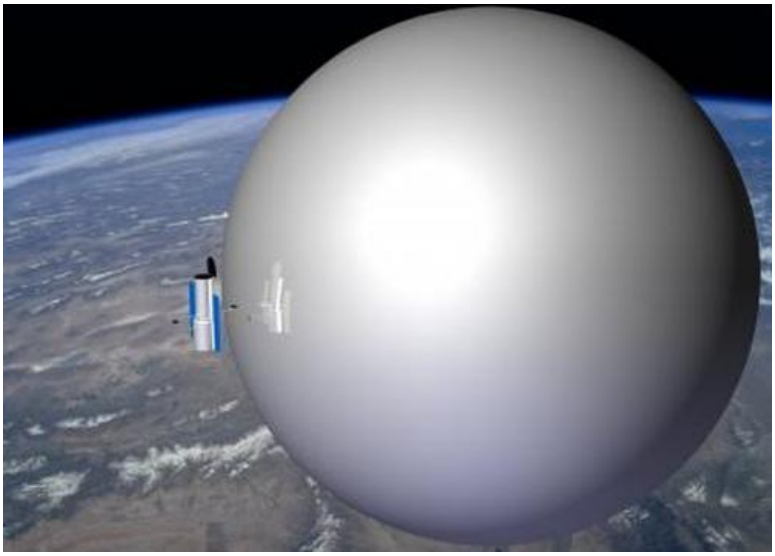

Figure 1.8: GOLD Gossamer Orbit Lowering Device concept (gaerospace.com)

forces between the two meshes are used to maintain the contour of the surface. In contrast, the EIMS concept uses electrostatics to inflate a layered membrane structure which does not require a rigid outer structure.This patent also discusses how sufficient electrostatic forces can be created at the kilovolt level via active charge emission using only Watt levels of power at geosynchronous orbit altitudes. Electrostatically controlling the surface of membrane mirrors in space has also been studied, such as the work of Errico, et. al. in Reference 30. These designs significantly differ from the proposed membrane structure inflation as the mirror and reflector technology requires a rigid external structure to support the surfaces. With EIMS, the gossamer structure is completely and compactly stowed until the charge level is increased to cause the entire structure to inflate.

Another application of electrostatic actuation is Coulomb control for free-flying flying spacecraft. This application aims to raise the absolute potential of the spacecraft to control the electrostatic interactions with surrounding vehicles. Actively charging a craft to a few kilovolts causes electrostatic forces between the craft of micro- to milli-Newton levels with millisecond charging time[31,32]. The concept is illustrated in Figure 1.10. In References 33 and 34 the Coulomb forces are explored to develop static virtual structures subject to both to the gravitational and electro-

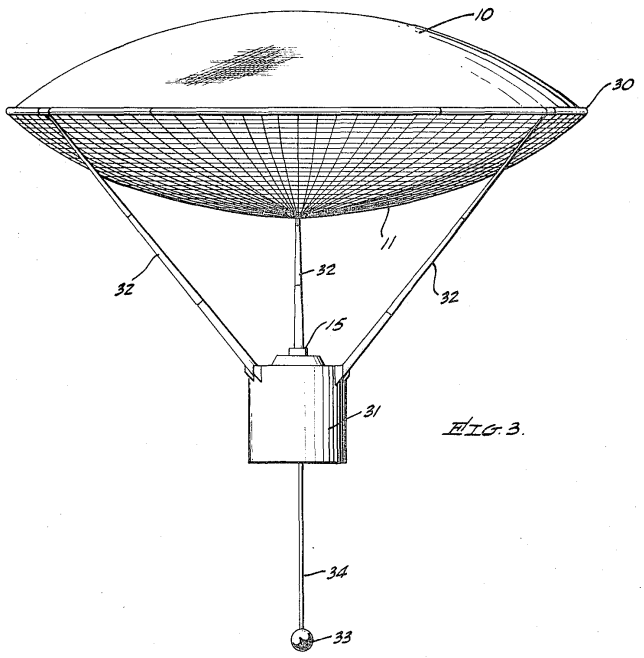

Figure 1.9: Cover's design for a electrostatically controlled antenna surface [1]

static force fields. Feedback control strategies of such virtual structures have only been developed for simple 2- and 3-craft systems thus far. [35,36] A related concept to the proposed electrostatic membrane structure is the Tethered Coulomb Structure (TCS). [37,38] Here the complex charged relative orbital motion is constrained through the use of tethers of sub-millimeter level thickness interconnecting the charged nodes. The electrostatic force is used to create an inflationary pressure to ensure positive tether tension at all times. Thus, the TCS can essentially be considered as a larger scale, discrete element precursor of EIMS. In contrast to the TCS concept, the EIMS differential orbital perturbations that drive charging requirements are different due to the larger mass and separation distances of the TCS system (50-100 kg nodes and multiple meters), versus the sub-kilogram membrane structure mass and centimeter separation considerations.

Another novel concept which utilizes electrostatics for space application is the electrostatic de-tumbling concept, explored in Reference 39. This patented concept utilizes a controlled, charged body in proximity to a second tumbling charged body. Electrostatic torques are utilized to arrest the

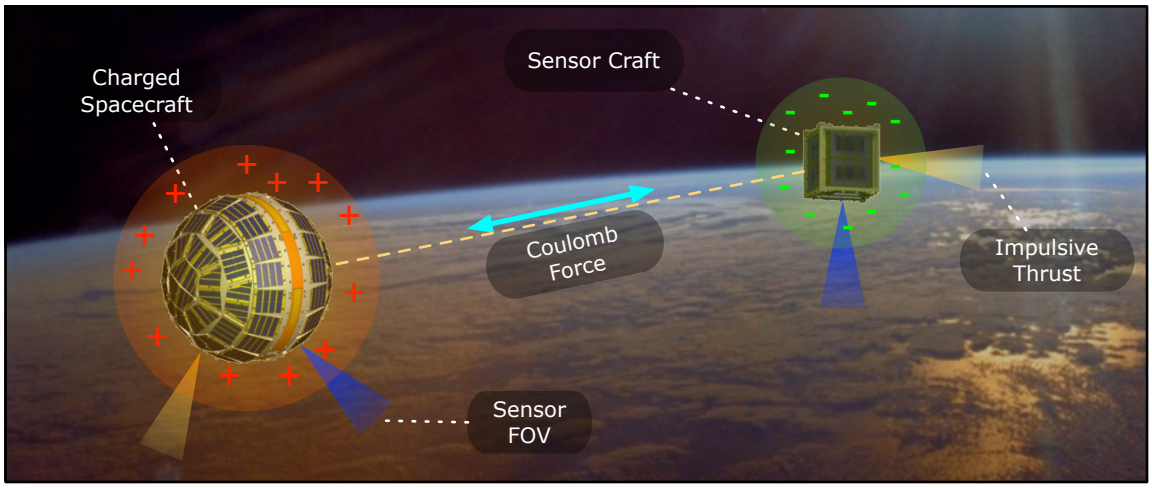

Figure 1.10: Illustration of the Coulomb Formation Flying concept

motion of the tumbling craft.[40] Reference 39 explores non-linear control strategies to accomplish de-tumbling by controlling the potential on the first craft.

Similar to the Coulomb relative attitude control concept, electrostatics could be used for re-orbiting a spacecraft. In Reference 39, the Geosynchronous Large Debris Reorbiter (GLiDeR) concept is described as a fuel-efficient method to re-orbit a debris object using electrostatic forces. Active charge control is used to change the potential of the GLiDeR craft and debris object, then a pusher or puller configuration can be employed to accomplish re-orbiting of a GEO object to a disposal orbit.

The challenge of controlling the potential of a body in space has been successfully flight tested. The SCATHA (Spacecraft Charging at High Altitudes) experiment was one of the spaceflight experiments that demonstrated use of ion and electron guns to control spacecraft surface potential to 10-20 kV[41,42]. Even without active charging, spacecraft can charge up to many kilovolts in the plasma environment. The highest recorded natural charging event occurred on the ATS-6 spacecraft, reaching a potential of -19 kV during an eclipse period of the GEO orbit[43]. While the previous two examples are space missions with active charge control at geosynchronous altitudes, the SPEAR I mission is an example of a charging experiment at Low Earth Orbit (LEO). The SPEAR

I mission employed active charging of test spheres in LEO with an altitude of approximately 350 km[44]. Using a capacitor, a positive potential of 45.3 kV was applied to two 10 cm radius spheres attached to a rocket body[44]. The current CLUSTER mission also employs active charge control through continuous charge emission to servo the spacecraft absolute potential to a desired near-zero charge level. The charge control of a spacecraft is, however, complicated by the presence of the plasma environment. While at geostationary altitudes the charge control can be achieved with low electrical power levels,[1,45] the relatively cold and dense plasma at low Earth orbits makes charge control more challenging. LEO applications would require more power, and the electrostatic field about a charged body is more quickly negated by the surrounding plasma charge.

In addition to the electrostatic space concepts discussed thus far, electromagnetics has similarly been considered for space applications. Two such examples are magnetic formation flight and electromagnetic deployment.

Electromagnetic deployment, illustrated in Figure 1.11, aims to decrease system mass and stowed volume by using a novel approach to unfolding or re-shaping a structure using electromagnetic forces. Electromagnetic deployment uses high-temperature superconductors to create magnetic fields from electrical current passing through coils[2]. Reference 2 describe several different functional uses of this concept such as deploying and holding the perimeter of a membrane structure with one single high-temperature superconducting coil. Other uses include unfolding a structure using a series of coils, creating distance between spacecraft parts with repelling coils, or changing the focal length of a mirror.

Electromagnetic formation flight is a concept similar to Coulomb formation flight. Here, electromagnetic forces between spacecraft (produced with superconducting electromagnetic coils) are used to control a formation of satellites[46]. The satellites could also take advantage of the Earth's magnetic field for passive formation manipulation.

The relevant literature review presented thus far provides much background information about related and enabling technologies for electrostatic inflation. There does not exist, however, detailed research on the concept of electrostatic inflation itself. The topic was found only briefly

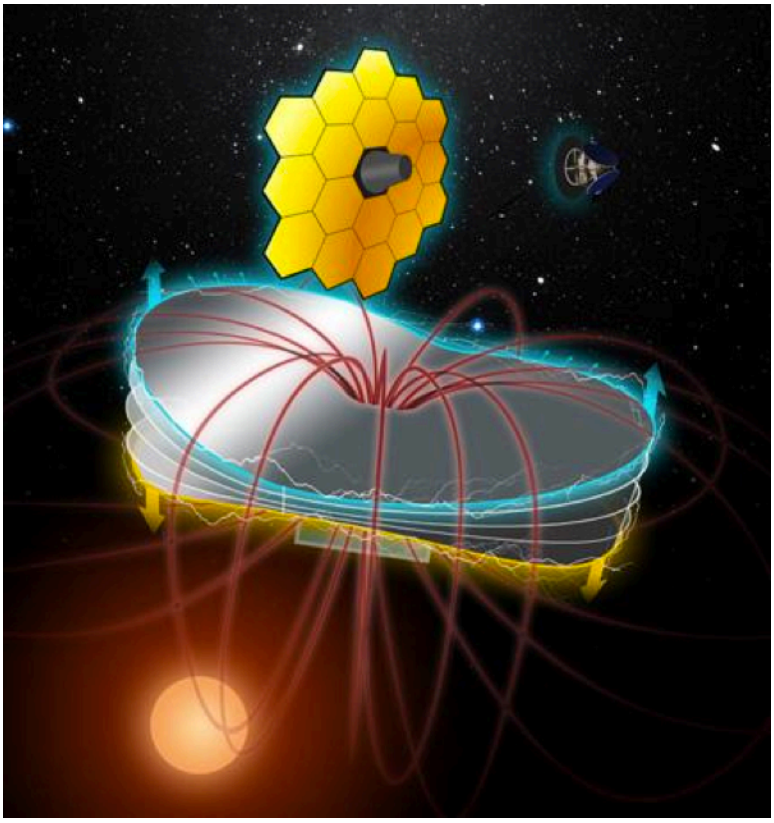

Figure 1.11: Illustration of the electromagnetic deployment concept [2]

in one reference. Reference 47 presented the concept of electrostatic inflation for deployment of a solar sail. In the description, charge is physically deposited onto a folded sail and the repulsive electrostatic forces unfold the sail. A simplified calculation was presented for the deployment time of a sail using electrostatics, showing the the deployment can take from minutes to hours depending on various parameters.[47] The minimal exploration of the topic of electrostatic inflation presented countless avenues for research. The approach was taken to address three fundamental questions, as outlined in the next section.

1.4 Overview of Research

The space-based electrostatic inflation concept is stil in the early stages of investigation. There are many associated challenges and avenues for research, such as non-linear structural mod-

eling and complex interactions with the space plasma, yet fundamental questions must be first addressed before considering such challenges. The goal of this research is to address *fundamental questions* related to electrostatic inflation:

(1) What are the necessary conditions for a meter-scale Electrostatically Inflated Membrane Structure (EIMS) to remain as a desired, inflated shape in vacuum space?

(2) What are the necessary conditions for a meter-scale EIMS to remain as a desired, inflated shape in a space plasma?

(3) What methods can be used to charge an EIMS to desired potential levels?

Investigating these three topics will begin to answer basic feasibility questions about electrostatic inflation, aid in determining where the concept may be applicable and help reveal the biggest challenges that will need to be addressed. These fundamental questions will not address more complex topics, such as deployment mechanics, packaging and subsequent material effects (e.g. wrinkling), or specific spacecraft designs for an application of EIMS.

The tasks associated with each of these focus areas are described. For the first research focus (EIMS in vacuum space), the following are addressed:

- Build prototype membrane structures to demonstrate electrostatic inflation in laboratory and vacuum environments
- Determine required voltages for laboratory inflation of prototype membrane structures
- Quantify charge distributions, electrostatic forces, and electrostatic fields for EIMS shapes using the Maxwell 3D numerical software
- Determine voltage requirements for offsetting orbital perturbation with the simplified case of an electrostatically inflated sphere and for the EIMS two-membrane structure
- Develop simple tools to simulate inflation of EIMS structures (the coupled electrostatic and structures problem)

For the second research focus (EIMS in plasma), the following are addressed:

- Quantify Debye shielding effects, specifically the 'effective' Debye length for high spacecraft potentials
- Demonstrate electrostatic inflation in the presence of a charge flux and identify interactions
- Explore charge deflection and wake patterns of EIMS in a charge flux

For the third research focus (charging methods), the following are addressed:

- Experimentally determine secondary electron emission properties of EIMS materials (metal coated polymers) to better understand EIMS charging
- Simulate charging scenarios in a plasma environment for different charging methods (remote charging, charge emission)
- Experimentally demonstrate charging via a remote charge beam and correlate with simulations
- Approximate power requirements for charging EIMS via charge emission

The research comprising this thesis covers many topics and fields of engineering and physics to answer the basic questions about electrostatic inflation. The results are laid out in the following chapters, organized with the second chapter summarizing the first proof of concept demonstrations of electrostatic inflation followed by three chapters addressing each of the three fundamental research questions. Chapter 6 provides a summary of the key contributions as well as recommendations for future work. This research yields a basic understanding of the necessary conditions of EIMS and sets up further questions which need to be answered for future work on electrostatic inflation.

Chapter 2

Laboratory Demonstration of Electrostatic Inflation

To explore the concept of electrostatic inflation and test the feasibility of the concept in a laboratory environment, simple inflation demonstrations were designed for the 1-g environment. These demonstrations are not representative of space situations but serve to demonstrate feasibility of using electrostatic pressure for deployment or shaping of membrane structures and to better understand the possible applications. The demonstrations also serve to better understand the challenges associated with EIMS, such as the extreme delicacy required for the handling of membrane materials. The laboratory results of this section are predominately qualitative.

An early question with electrostatic inflation was whether the membranes would inflate, as there is theoretically no electrostatic field between two like-charged sheets. This is illustrated in Figure 2.1 in comparison to a parallel plate capacitor setup, which functions based upon the electric field between the plates. Although there is no field between the membranes, the charge on the conducting membranes still experiences an electrostatic forces due to the charges on the opposite membrane, enabling inflation.

The membrane materials used for construction of electrostatic structures include aluminized Mylar and aluminized Kapton films with thicknesses ranging from 6 to 20 microns. The aluminum deposition layer on the polymer films is approximately 0.1 microns and covers both sides of the film. Membrane materials were generously provided by the Multex company.

Initial demonstrations were successfully performed with a hand-held Van der Graaf generator used to directly charge the membranes. A more controllable charging method is desirable though,

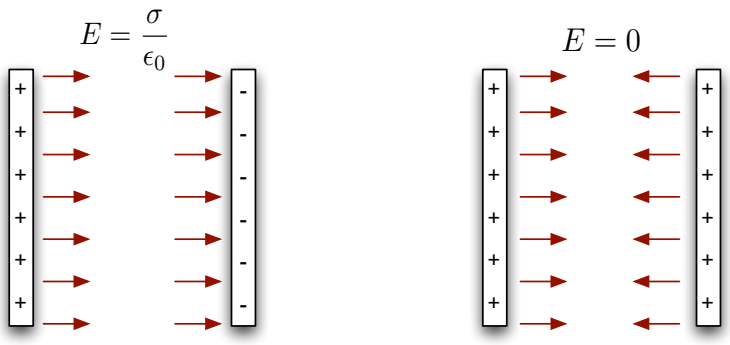

Figure 2.1: Illustration of electric fields between oppositely charged (parallel plate capacitor) and like charged (EIMS) plates

therefore a high voltage EIMS charging setup was designed and constructed for the laboratory. The charging setup is used to apply a desired voltage to the membrane structures for inflation. Figure 2.2 displays a diagram of the setup. The high voltage is supplied by an Ultravolt 40A Series high voltage DC-DC converter. This device supplies up to -40kV to the membrane structures. The voltage magnitude is controlled by a user through a Graphical User Interface on a Macbook computer, as shown in Figure 2.3. A National Instruments USB-6008 data acquisition device is used to drive the power supply and also to record current and voltage data. This custom software allows the EIMS to be charged to a particular voltage by either manually moving the voltage slider, or by running a predefined voltage history on the structure. Surface voltages are measured using an electrostatic surface voltmeter.

2.1 Atmospheric Electrostatic Inflation Demonstrations

With the high voltage charging setup, tests were conducted to inflate a variety of membrane structures in the laboratory environment. While these demonstrations suffer from atmospheric interactions, atmospheric inflation experiments allow a quick method to test the capabilities of the high voltage charging system without the rigors of preparing a vacuum system.

The first laboratory electrostatic inflation demonstrations involved a variety of membrane shapes. In these demonstrations, the high voltage charging setup is used to apply a desired voltage

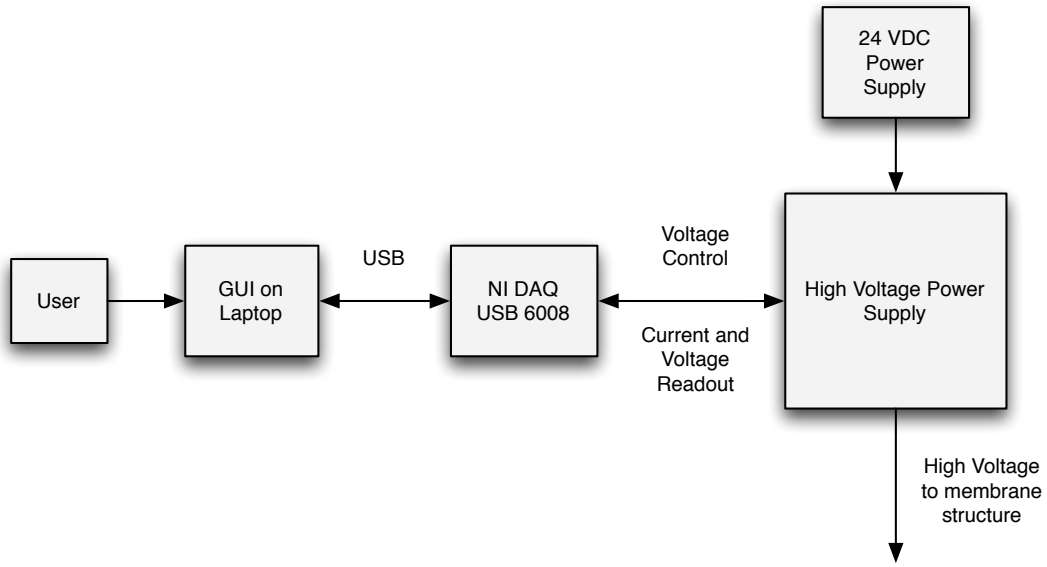

Figure 2.2: Block diagram of high voltage charging setup for membrane structures

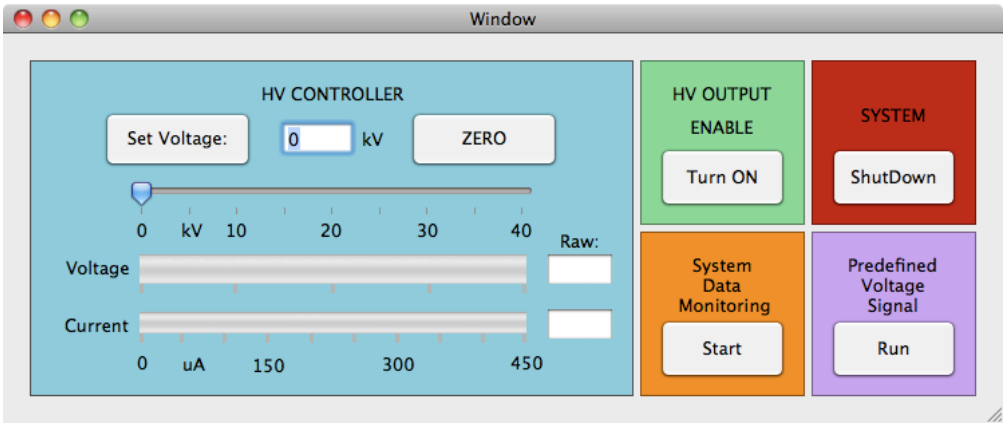

Figure 2.3: Graphical User Interface for operating the high voltage charging setup

to the membrane to induce inflation. Figure 2.4 shows the inflation of a gossamer ribbon structure, an example of a structure with large open surface segments. This ribbon structure was initially compacted to height of approximately 2 cm, then inflated to a height of 25 cm. This demonstration shows the potential of high deployed to stowed volume ratios with the electrostatic inflation concept. Notice in this photo series that the structure has obtained the fully inflated shape at 5 kV, yet

gravity is preventing the structure from standing upright. As the voltage increases to 9 kV, the electrostatic repulsion between the ribbon structure and the conducting surface to which it is attached cause the entire structure to become upright as well as inflated to the desired shape. Membrane structures were also constructed in the envisioned 2-membrane sandwich structure shape of EIMS. Figure 2.5 shows a structure resting on a conducting surface which is connected to a high voltage power source. In this 1-g test environment, the forces on the lower plate are always balanced by the normal force of the object upon which it rests. The other plate is subjected to the Coulomb force to inflate, the compressive force of gravity, and tension in the membrane ribs to hold the structure together. This setup is much like an along-track orbit configuration in which the differential solar radiation pressure and/or the differential atmospheric drag are acting to collapse one membrane onto the other (assumed fixed) membrane. The structure used in this test consists of two 12x15 cm plates of 75 gauge aluminized Mylar. Three aluminized Mylar ribs connect the two membranes. Voltage was applied to the conducting sphere on which the membrane structure rested.

Video snapshots of an inflation demonstration are shown in Figure 2.5 to show that in the laboratory environment, a membrane structure can transition from a collapsed initial state to an inflated state using only electrostatic pressure. Inflation occurred between 7 and 13 kV during different inflation trials. The duration of the inflation shown between the first and last frames of Figure 2.5 is approximately 5 seconds.

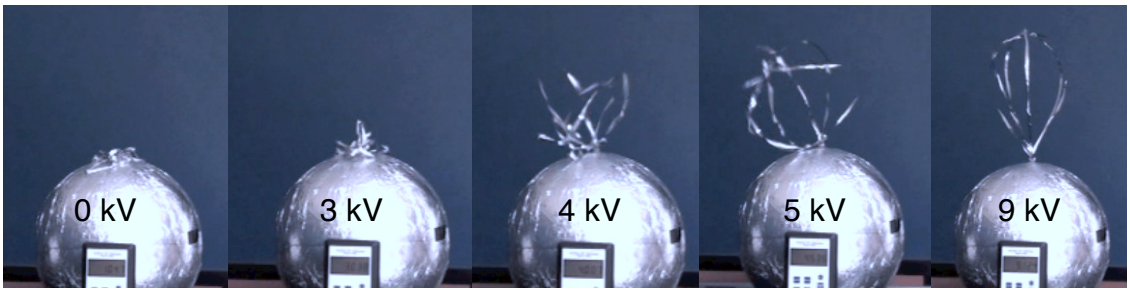

Figure 2.4: Electrostatic Inflation of gossamer ribbon test structure, from 0 kV to 9 kV

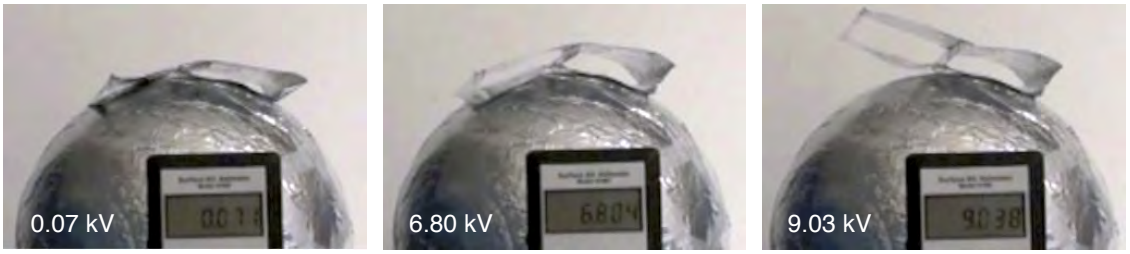

Figure 2.5: Electrostatic Inflation of a test sandwich structure, from 0 kV to 9 kV

To avoid the need to overcome gravity, many demonstrations were performed by vertically hanging membrane sheets and inducing horizontal electrostatic inflation. Early tests included charging of two independently hanging sheets of aluminized Mylar. Figure 2.6 shows the inflation during a test where each sheet was charged to 10 kV. This setup allowed study of different shapes and sizes of membrane materials. Smaller membrane structures inflate more easily than a larger, similar structures charged to the same potential due to higher charge density, thus higher electrostatic pressure. Membranes with material cut-outs (such as the square cut-outs visible in Figure 2.6) inflate with lower potentials than solid sheets, again due to the higher charge densities at corners.

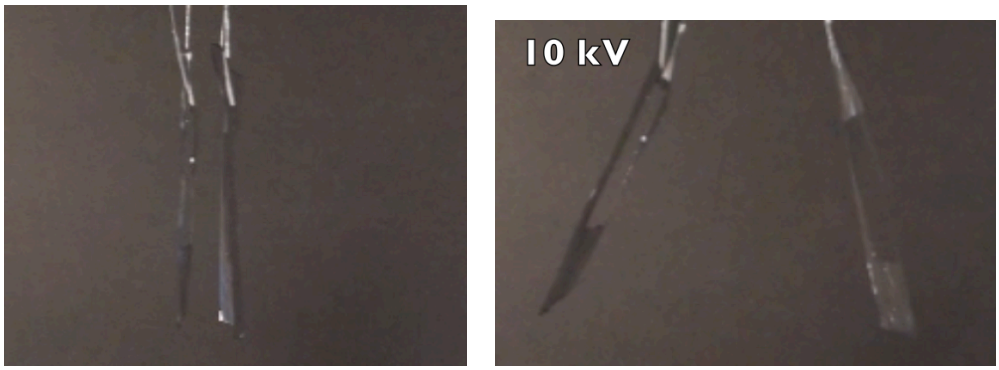

(a) Before inflation, 0 kV (b) Inflation, 10 kV

Figure 2.6: Uncharged and charged hanging membranes during a laboratory inflation test

For the structures tested in the laboratory, inflation was observed for all EIMS test objects at charging levels as low as 4 kV. Below the 4 kV level, effects from the atmosphere are prohibitive to inflation. When charging to kilovolt level potentials, the air ionizes and can induce attraction

between like-charged membranes. These results demonstrated that a vacuum environment is critical to simulate how electrostatic inflation may occur in a more space-like environment.

Another challenging issue in atmospheric tests is membrane stickage. In laboratory tests to inflate a structure, such the one illustrated in Figure 1.3, a non-conducting gap or layer between conducting surfaces is required for electrostatic inflation to occur. Without a gap, the layers of charged conducting sheets do not separate due to stickage between the tested membranes. For electrostatic inflation, it is speculated that non-connected segments may be beneficial between the conducting surfaces such as gaps or un-polarized dielectric layers. In laboratory inflations, a small gap with air between surfaces has been shown as sufficient for inflation to occur across a comparatively large structure.

An important issue observed in laboratory demonstrations is the impact of the non-uniformity of charge density. Initial inflations were often performed by placing the structure onto a charged, conducting sphere or plate. With the rectangular plate, the charge density is not uniform and most charge lies on the corners and edges of the plate. For this reason, any structure placed in the center of a plate (especially a large plate) often does not achieve sufficient charge for inflation. This is illustrated in Figure 2.7 with small membrane sheets electrically connected to a charged, conducting plate. As the voltage on the conducting plate is increased, the charge density levels become large enough to enable repulsion of the membranes and lift them off the plate. The progression in which membranes lift helps to visualize the charge density distribution. Importantly, the membrane in the center does not inflate at any applied voltage due to low charge density. On an EIMS structure on-orbit, the required charge density at this minimum in the center of the membrane sets the required charge density and thus the required voltage for inflation. This inflation demonstration is later compared to the 3D numerical electrostatic solution to quantify why the center membrane does not have required electrostatic pressure to overcome gravity.

This demonstration shows the importance of understanding the charge density distribution which enables electrostatic inflation. For this reason, the 3D electrostatic modeling is a key component of this research.

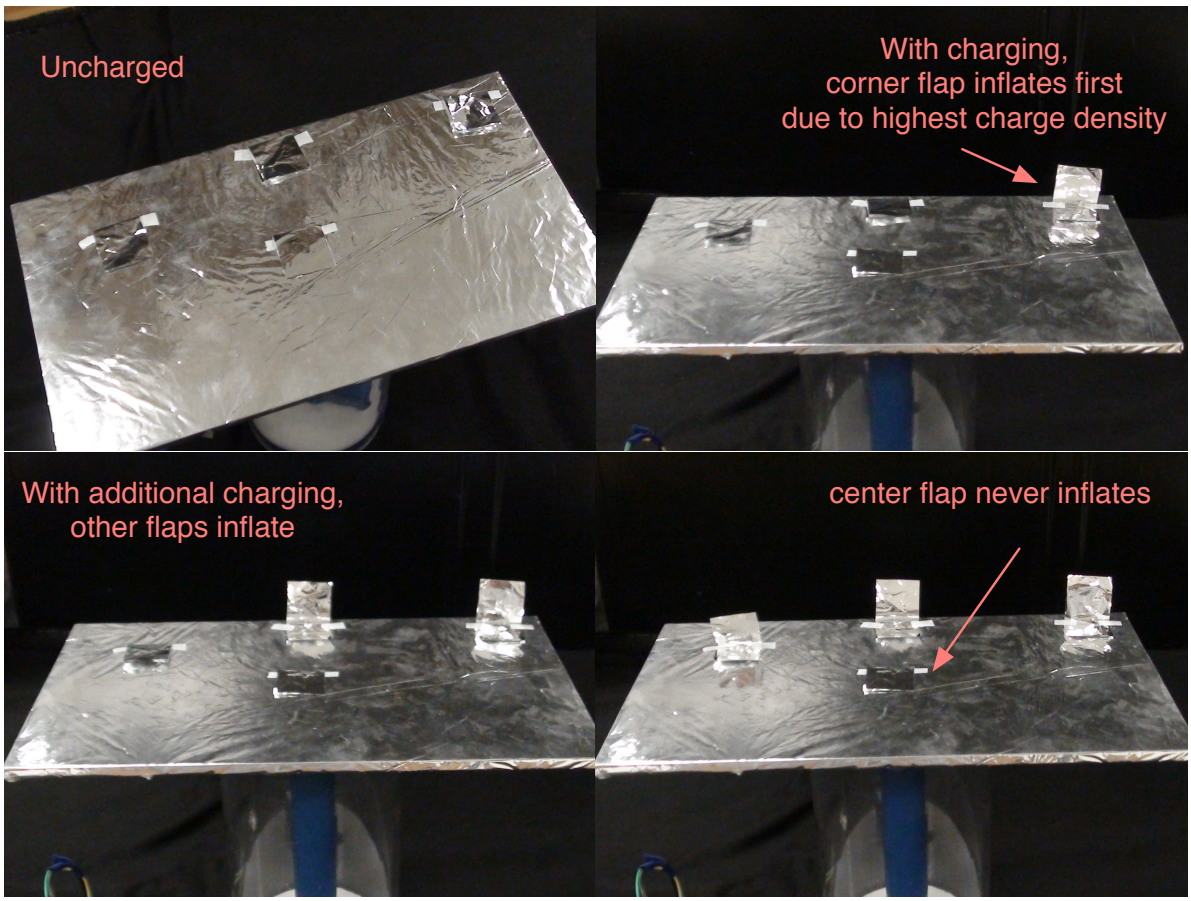

Figure 2.7: Charge density non-uniformity demonstration via electrostatic lifting of membrane sheets

2.2 Electrostatic Inflation Demonstrations in a Vacuum Environment

As the laboratory demonstrations suffer from interactions with the atmosphere, the electrostatic inflation test setup was moved to a vacuum chamber. Access to a vacuum environment was provided by Colorado Center for Lunar Dust and Atmospheric Studies (CCLDAS) at the east campus facility of the University of Colorado at Boulder. The chamber is a cylindrical aluminum chamber with a diameter of 30cm, shown in Figure 2.8. The high-voltage supply to the structure within the chamber is accomplished with a high voltage electrical feedthrough rated to 10 kV. The hanging structure is mounted directly to a metal post of the feedthrough for direct connection to the HV supply.

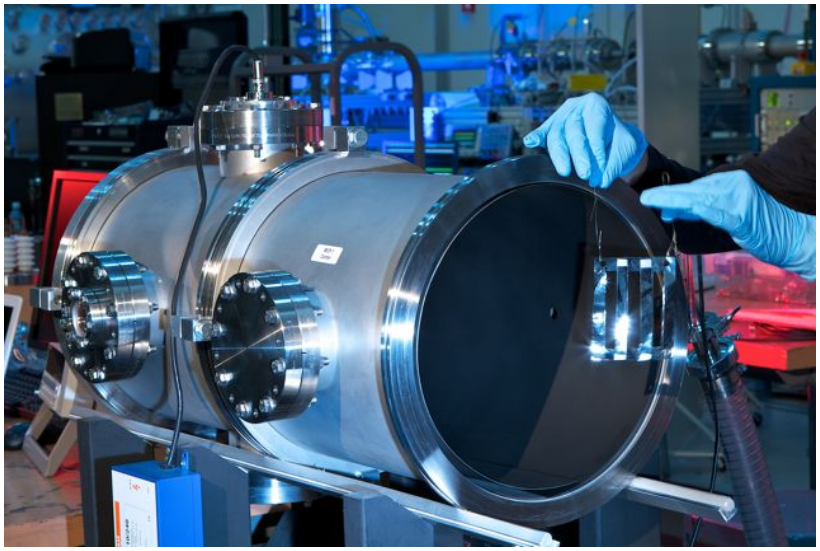

Figure 2.8: Vacuum chamber used for electrostatic inflation demonstrations and experiments

Testing in the vacuum chamber environment requires much more rigor than the atmospheric demonstrations, as special preparations and cleaning procedures are required. Also, only certain materials are allowed to be used, based on their outgassing properties that can damage pumps and other hardware. In general, plastics are not suitable for the vacuum environment, with some exceptions (such as Kapton). Kapton was an important material for these demonstrations, as Kapton tape was often used in construction of membrane structures or as ripstop. All hardware entering the vacuum chamber was carefully cleaned using a sonic bath of ethanol. Extra care was required with the aluminum coated polymer materials, as long soaking in the ethanol would cause a melting type reaction that warps the structures. Also, the ethanol bath removed the stickiness of the Kapton tape, therefore taping for construction or ripstop had to be done after the ethanol bath.

A chamber environment of approximately 10^{-6} Torr was used to verify electrostatic inflation capabilities in a vacuum. Previously observed effects in laboratory tests from the atmosphere becoming ionized and inducing attraction between the sheets were not observed in the vacuum chamber, as predicted. Significantly lower voltage magnitudes are required in the vacuum environ-

Figure 2.9: Electrostatic Inflation of membrane structure within the vacuum environment

ment to induce the same inflation levels that are observed in the laboratory atmosphere at higher voltages.

Similar to the atmospheric demonstrations, many shapes of membrane structures were investigated within the vacuum environment. Similar results were found in these demonstrations, verifying that smaller structures and membranes with cutouts inflate with a smaller absolute potential. Figure 2.9 shows an electrostatic inflation demonstration in the vacuum environment for two hanging membranes with material cut-outs. The membranes were at a potential of 4 kV for this demonstration.

It must be noted that electrostatic inflation does not occur at all levels of vacuum pressure due to electric breakdown. If the breakdown voltage is attained, an electric arc forms and discharges the surfaces. Paschen's Law is used to determine the breakdown voltage in a specific gas as a function of only pressure and separation distance between 2 parallel plates. The relationship describing the phenomena is given in Equation 2.1 where pd is the product of pressure and separation distance and a and b are constants specific to the gas. These curves are illustrated in Figure 2.10 for various gases with data from Reference 48.

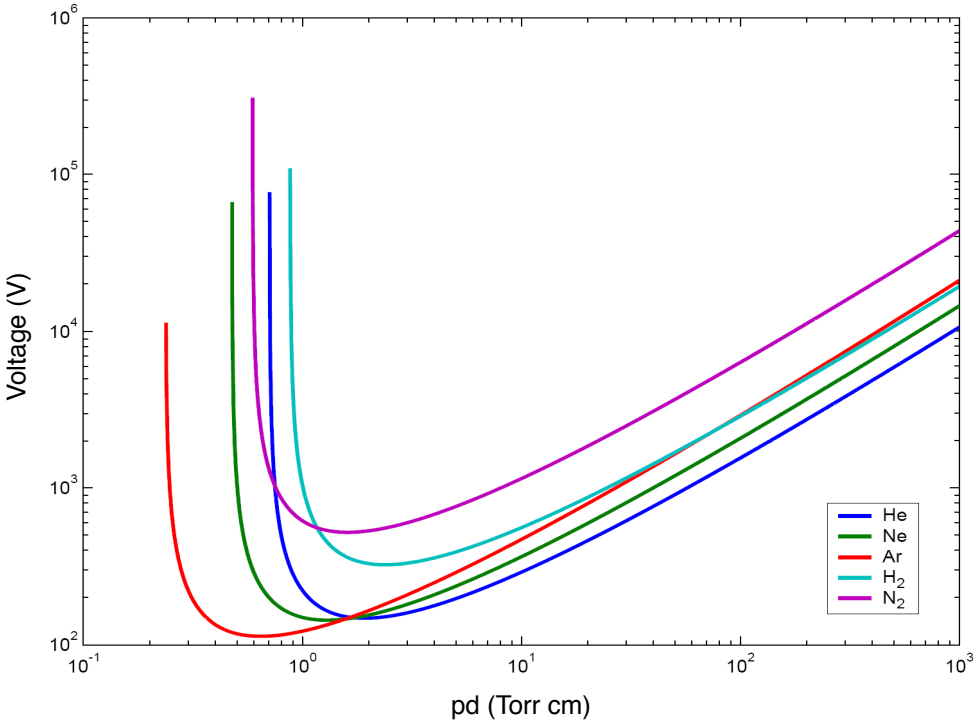

Figure 2.10: Paschen curves for select gases showing breakdown voltage as a function of the pressure-distance product.

$$V = \frac{a\ pd}{\ln(pd) + b} \tag{2.1}$$

It is important to understand when electric breakdown will occur (and the membranes thus do not inflate) for laboratory and vacuum experiments. EIMS requires on the order of a few kilovolts for inflation in 1-g. From Figure 2.10, it can be seen that the breakdown voltage is below kilovolt level for N_2 for a considerable range of the pressure-distance product.

The effect of Paschen discharge was observed in this research during the first attempt to demonstrate electrostatic inflation in a vacuum environment. Before access to the CCLDAS vacuum chamber, the first vacuum environment inflation attempts took place in a bell jar vacuum provided by the Colorado Space Grant Consortium. The pressure achieved inside the bell jar was approximately 1.5 Torr for the experiments. Assuming the required voltage is 5 kV for inflation,

any distance between approximately 0.5cm and 80cm will cause breakdown. The geometry of the bell jar is such that separation distances between the charged membranes and grounded surfaces could not reach 80 cm. Electrostatic inflation could not be observed at the pressures which were achieved in the bell jar, therefore to demonstrate electrostatic inflation in a vacuum, a lower vacuum pressure was be required. The CCLDAS chamber can attain vacuum pressure on the order of 10^{-7} Torr, therefore Paschen discharge is not a concern. This will not be an issue for EIMS on-orbit, as the pressure is extremely low (near perfect vacuum). Paschen discharge does, however, need to be considered for laboratory and vacuum systems for development and testing purposes.

In summary, demonstrations indicate that self-supporting membrane structures can repeatably and reliably be electrostatically inflated in a laboratory and vacuum environment. Such physical results are useful to explore appropriate materials, construction methods, packing methods, and charging behaviors that lead to desirable membrane motions. Further, such testing can be used in the future for validation and verification purposes of high fidelity modeling of charged membrane structures. The relatively small potential levels required to inflate the membrane structures in 1-g are promising to the concept of electrostatic inflation for space structures. As the orbital disturbance pressures are orders of magnitude smaller than the pressure due to gravity in the 1-g environment, required potentials can be much smaller than required in Earth-based experiments, as is further described in the following chapter.

Chapter 3

EIMS operating in vacuum spaces

The first fundamental question that is addressed in this thesis is: what are necessary conditions for inflation to be maintained using electrostatic pressure for a meter-sized membrane structure in a vacuum environment. Here, we do not address the deployment problem, rather the scenario in which an EIMS is on-orbit, post-deployment and undergoing disturbance forces or torques from orbital perturbations (differential gravity, solar pressure, and atmospheric drag) or a spacecraft maneuver. Plasma effects are considered to be negligible for the force evaluation in the analysis of this chapter.

The question of maintaining a desired inflation pressure is a question of maintaining the required charge density across the membrane. To understand inflation pressure for EIMS, the first step is therefore to be able to understand electrostatic solutions for various geometries being considered for these space structures. This problem is studied numerically in the first section. With the tools to determine the electrostatic solution, potential EIMS geometries are next discussed. Basic shapes envisioned for electrostatic inflation, such a sphere, cylinder, and 2 membrane sandwich structure, are explored. Finally, voltage requirements are derived for one case of electrostatic inflation on-orbit undergoing orbital perturbations. The procedure presented for determining voltage requirements due to the chosen disturbance can be extended to all distributed disturbance pressures.

3.1 Electrostatic Solutions for EIMS Geometries

With electrostatics, simplicity is limited to point charges and spheres. Beyond an isolated sphere, charged bodies will not have uniform charge distributions. The complexity of geometries requires going beyond analytical expressions to numerical approaches. To study the electrostatic fields and charge distributions of a charged membrane structures, the Maxwell 3D software is chosen. Maxwell 3D is an Ansoft software package that uses finite element analysis to solve 3D electrostatic problems[49]. The software provides solutions of electrostatic fields, forces, and charge distributions, as well as capacitances based on user-drawn geometries.

The procedure for determining the electrostatic solutions for the membrane structures includes drawing the membrane geometry, assigning material properties, assigning a voltage to the membrane, and drawing a boundary region with a zero voltage to the boundary. It was determined that the zero voltage boundary should be 2000% in each direction of the geometry to have no effect on the electrostatic solution for the membrane. The software automatically meshes the geometries and region using tetrahedral elements. Maxwell 3D solves Maxwell's equations (Equation 3.1 for the electrostatic case) in a region based on assigned boundary conditions and initial conditions. The unique results of the problem are electrostatic charge distribution, fields, forces, and the capacitance matrix.

$$\nabla E = \frac{\rho}{\epsilon_0} \tag{3.1}$$

Maxwell 3D enables understanding of the charge distributions for various shapes considered for electrostatic inflation applications. A critical parameter to investigate is the minimum charge density on the membrane, as this is where the inflation pressure will be at a minimum. When considering the minimum required charge density, it is important to consider the non-uniformity of the charge distribution on the membranes as charges rearrange to create zero electric field inside the conductor. As expected, numerical results show that surface charge is highest at corners, as can be seen in Figure 3.1, where red represents the largest value of surface charge. This occurs because

charge rearranges inside a conductor such that there is no electrostatic field inside the conductor. As seen in Figure 3.1, the minimum charge density is in the center of the membrane. This has important implications for determining where the inflated membrane structure is most likely to collapse from external pressures.

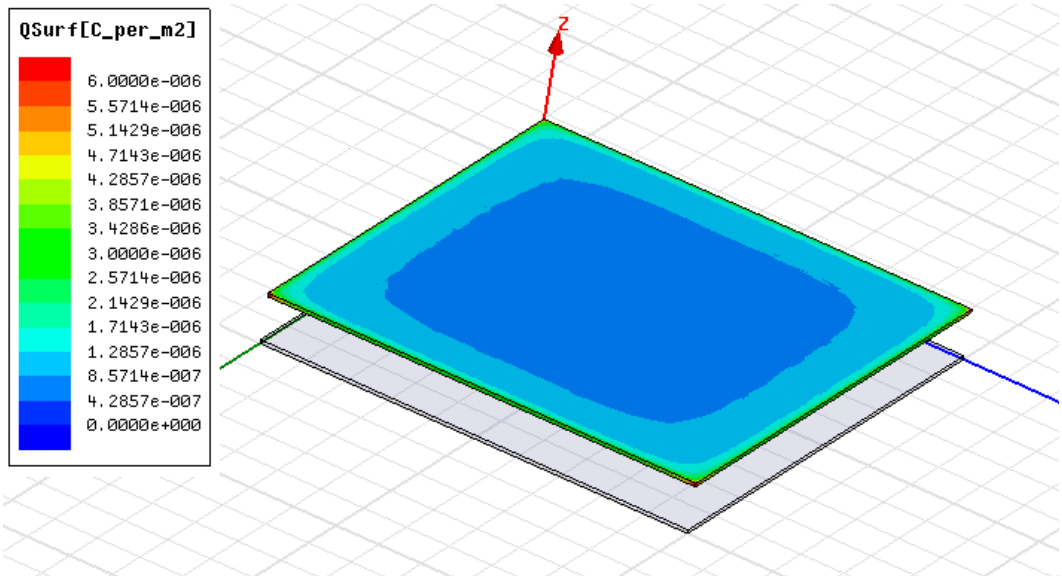

Figure 3.1: Numerical solutions of surface charge distribution on two charged plates

Electrostatic inflation of a structure occurs when an electrostatic potential is applied and the charges distributed on the outer surface repel each other, expanding the structure. The potentials must be high enough to produce sufficiently large electrostatic forces for self-repulsion to negate the compressive differential forces from gravity, solar radiation pressure, atmospheric drag, or a spacecraft maneuver that would be experienced on orbit.

For inflation of the structure, there must be sufficient electrostatic pressure across the entire surface of the membrane to offset these perturbations. This required pressure to exactly offset the disturbances is associated with a required electrostatic charge density which is referred to as the minimum charge density on the membrane. Below this minimum charge density, the structure can compress or collapse from the disturbance.

Consider the two-membrane setup shown in Figure 3.2. We desire to find the required charge

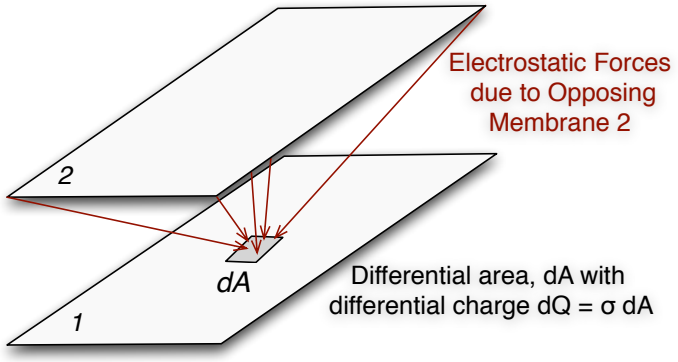

Figure 3.2: Differential area element experiencing electrostatic forces from the distributed charge on the opposing membrane

density on a small element of area dA such that the electrostatic pressure is at least the magnitude of the normal disturbance pressure. The charge on this differential area is:

$$\mathrm{d}q = \sigma \mathrm{d}A \tag{3.2}$$

The fundamental electrostatic force equation yields the differential force on this area due to the electric field normal to the surface:

$$\mathrm{d}F = E_n \mathrm{d}q \tag{3.3}$$

Rewriting this equation as the pressure and substituting Equation (3.2) yields:

$$\mathrm{d}P = \frac{\mathrm{d}F}{\mathrm{d}A} = \frac{E_n \sigma \mathrm{d}A}{\mathrm{d}A} = \sigma E_n \tag{3.4}$$

Application of Gauss's Law yields the electrostatic field at the surface of the membrane with knowledge of the local charge density:

$$E_n = \frac{\sigma}{\epsilon_0} \tag{3.5}$$

The pressure on the small area element is therefore only a function of the charge density on the membrane:

$$\mathrm{d}P = \frac{\sigma^2}{\epsilon_0} \tag{3.6}$$

Equation (3.6) can thus be rearranged to solve for the minimum charge density at any location on the membrane to create a required inflationary pressure level (P_{req}) :

$$\sigma = \sqrt{\epsilon_0 P_{req}} \tag{3.7}$$

This equation is a **key equation** for electrostatic inflation. It is applicable for any EIMS geometry and any disturbance pressure being applied to the system (orbit perturbations or maneuvers).

However, voltage, not charge density, is the parameter which will be actively controlled in the space environment to inflate the structure, therefore it must be determined from these required charge densities. As the structures considered for EIMS go beyond shapes with simple capacitance relationships, such as a sphere, a relationship between the potential and charge is generally not analytically known. Numerical electrostatic field modeling is therefore required to determine the capacitance of each of the different EIMS geometries such that the required charge densities determined with Equation 3.7 can be related to required voltages. The following section explores the capacitance and other considerations for different geometries considered for EIMS.

3.2 EIMS Geometry Considerations

3.2.1 Sphere configuration

First considered is the simplest geometry for the electrostatic solution, that of a sphere. With a spherical geometry, the charge distribution is uniform and analytical relationships exist to describe the electrostatic forces and the self capacitance:

$$C = 4\pi\epsilon_0 R \tag{3.8}$$

The membrane sphere has been used for several applications in previous space missions. As described in the background section of the thesis, the ECHO satellite was a membrane sphere used as a communications reflector, and the similar PAGEOS sphere was used as a reflective surface for mapping purpose. Another envisioned application of a large membrane sphere is a drag de-orbiting

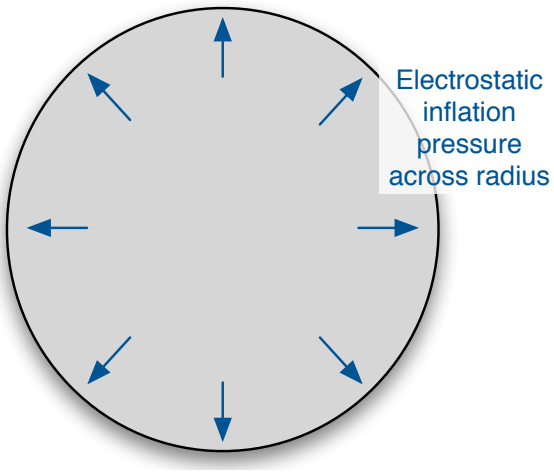

Figure 3.3: Electrostatically inflated membrane sphere

device, such as the proposed GOLD spacecraft. A sphere could also be used as a star shade. The electrostatic sphere concept is illustrated in Figure 3.3.

The geometry is modeled after the ECHO balloon structure. Gores of a conducting membrane material are used to construct a single-layer spherical shape. Electrostatic charge would be evenly distributed across the layer and the electrostatic forces would act across the radius of the sphere. One of the limitations of a spherical shape is the large distance over which the electrostatic forces must apply. For a gas-inflated sphere, larger sizes equate to higher gas pressure. For EIMS, a larger sphere requires achieving a larger electrostatic potential, which has limitations in space.

For the ideal membrane sphere, the electrostatic solution is simple. An analytical development is presented here which describes voltage requirements for an electrostatically inflated sphere. The mathematical development is as follows.

The electrostatic potential energy of the charges on the sphere is described by:

$$U = \frac{1}{2}\int V\sigma \mathrm{d}S = \frac{1}{2}VQ \tag{3.9}$$

As the spacecraft potential is the parameter which is controlled, this can be rewritten as:

$$U = \frac{1}{2}CV^2 = 2\pi\epsilon_0 V^2 R \tag{3.10}$$

To find the force, we use the derivative of the potential energy:

$$F = \frac{\mathrm{d}U}{\mathrm{d}R} = 2\pi\epsilon_0 V^2 \tag{3.11}$$

This is the total force acting on the sphere, but we are interested in pressure. The surface pressure would be:

$$P = \frac{F}{A} = \frac{F}{4\pi R^2} = \frac{\epsilon_0 V^2}{2R^2} \tag{3.12}$$

This relationship is illustrated in the plot shown in Figure 3.4. Electrostatic pressure values (Pascals) are shown on the contour lines as a function of the voltage and the sphere radius. To inflate a sphere with a radii much larger than the 5 meters shown, the voltage requirements become larger than the tens of kiloVolts that are considered feasible on-orbit.

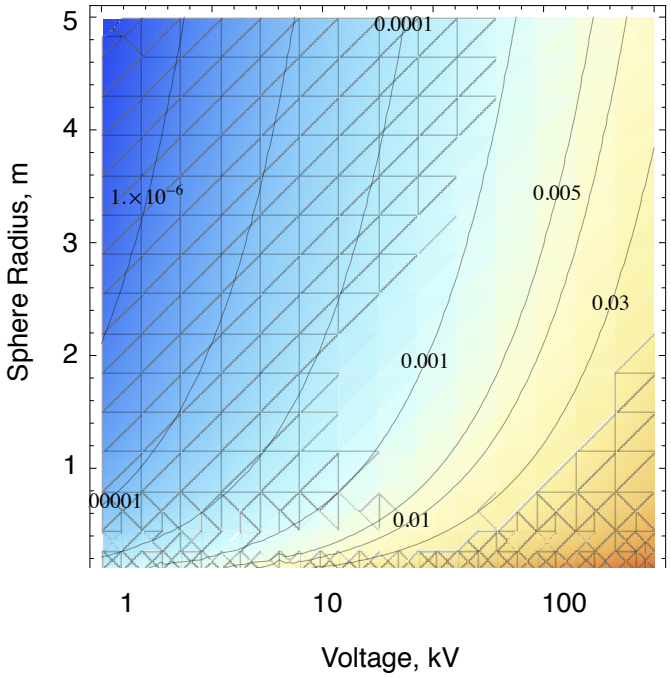

Figure 3.4: Pressure contours (Pa) as a function of voltage and sphere radius for an electrostatically inflated sphere

A further option for a spherical electrostatic structure is a non-solid membrane. In laboratory demonstrations, it quickly became apparent that structures made of membrane strips (or ribbons) inflate extremely well. With the ribboned structure, the charge density for a given voltage is much

higher than for a solid membrane. The Maxwell 3D software verifies that charge densities on a conductor are higher at the edges. With the ribboned structure, there are many edges and electrostatic repulsion between opposite sides becomes much higher. The ribboned structure would also be more lightweight and simpler to manufacture and package. However, some of the applications for a sphere, such as a star shade, would not be as functional without the solid surface.

One of the ribboned structures built for laboratory demonstrations is shown in Figure 3.5. This lightweight structure inflates extremely easily and the repulsion between the structure and the conducting surface easily overcomes gravity with less than 10 kV.

Figure 3.5: Spherical configuration with membrane ribbons

3.2.2 Cylindrical configuration

Next, a electrostatically inflated cylindrical tube is considered. This EIMS configuration is a cantilever cylindrical tube of membrane material which uses electrostatic pressure to give shape and strength to the tube.

A cylindrical tube is a common structure used for space inflatable structures. Cylinders can

Figure 3.6: DLR's cylindrical inflatable boom (deploytech.eu)

be used as booms for deploying an instrument or camera or as a support structure for a larger structures such as a solar sail or reflector. One example is the DLR deployable boom, shown in Figure 3.6. The boom is made of carbon fiber reinforced plastic and is being used primarily as the deployment device for a European solar sail mission (although it has several other applications). [50]

The cylindrical tube geometry has been explored for electrostatic inflation applications both conceptually and through demonstration. For EIMS, the charge distributed along the cylinder provides inflation pressure that gives stiffness to the cylinder. The concept is demonstrated in laboratory experiments to observe buckling of the cylinder with and without electrostatic pressure. The charged cylinder can reach higher angular displacements (procedure shown in Figure 3.7) before collapse than a non-charged cylinder. As a note, this demonstration is very dependent on previous bending or buckling in the membrane which causes permanent wrinkles. As described previously, wrinkles are a key factor in designing the packaging for EIMS.

As with any non-spherical shape, the charge distribution for a charged cylinder is non-uniform. The charge density drops exponentially from the ends of the cylinder, thus the length of the structure is limited by the required charge density in the center of the cylinder. Maxwell 3D is used as a tool for understanding the minimum charge density based on an applied voltage. Figure 3.8 illustrates an example of the charge density solution for a charged (30 kV) conducting cylindrical membrane tube.

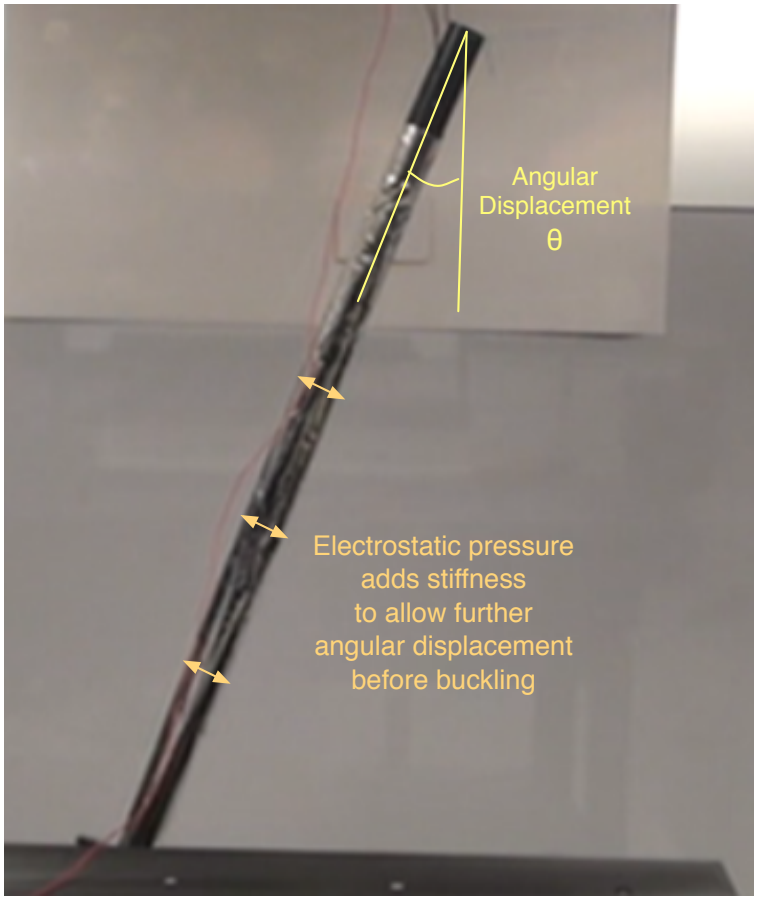

Figure 3.7: Laboratory demonstration of electrostatic pressure increasing stiffness in cylindrical membrane tube

3.2.3 Two membrane sandwich configuration

The two membrane sandwich configuration is envisioned as similar to a ram air parachute with ribs connecting the two membranes which are expanded by electrostatic pressures, as illustrated in Figure 1.3. Such a configuration is shown in Figure 3.9 in a laboratory inflation demonstration. Here, the membrane became fully inflated at approximately 9 kV. With small scale prototypes, the membranes remained relatively flat. It is expected that there could be billowing between the membrane attachments (ribs), but this would be better understand with FEM simulation of the membranes to understand stable configurations. As a note, the 2-membrane sandwich structure is not limited to the rectangular shapes that were explored in the laboratory and in the analysis presented here.

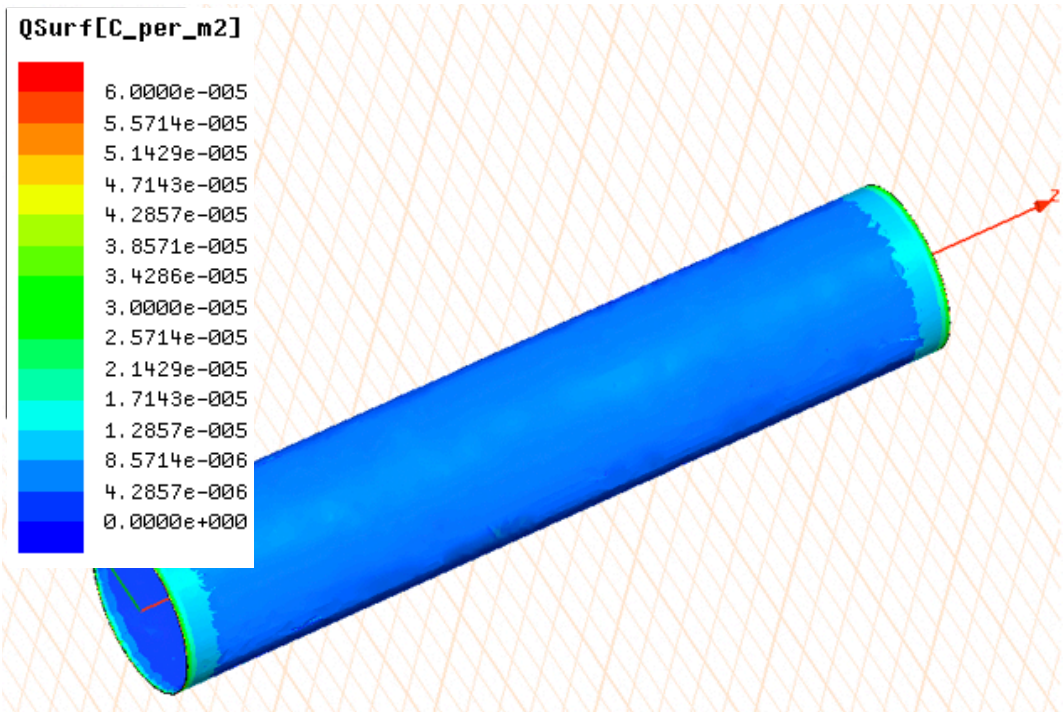

Figure 3.8: Illustration of Maxwell 3D electrostatic solution for charge density for a charged (30 kV) cylindrical membrane tube

Figure 3.9: Electrostatically inflated 2-membrane sandwich structure

To understand the capacitance relationship for the sandwich configuration, Ansoft's Maxwell 3D software is used to create geometries, simulate electrostatic fields, and numerically determine forces on the membranes. The numerical simulations are performed for a model of two conducting, finite plates in a vacuum. For the two plate configuration, the capacitance matrix relationship is as

shown in Equation (3.13), where V is the voltage and Q is the total charge on the membrane. The diagonal components of this symmetric matrix are the capacity coefficients and the off-diagonal terms are the electrostatic induction coefficients.[51] The induction coefficients are negative values and account for the decrease in the potential due to a nearby conductor.

$$\begin{bmatrix} Q_1 \\ Q_2 \end{bmatrix} = \begin{bmatrix} C_{11} & C_{12} \\ C_{21} & C_{22} \end{bmatrix} \begin{bmatrix} V_1 \\ V_2 \end{bmatrix} \tag{3.13}$$

The values of the capacitance matrix are dependent only on the geometry of the conductors. For this system, the capacitance can be altered by changing the area of the plates or by changing the separation distance between the plates.

Figure 3.10 illustrates the effect of changing the area of the structure. Increasing the area increases the capacitance of the system, allowing more charge to reside on the structure for a fixed value of potential. The repulsive forces between the two membranes therefore increase with this additional charge, as shown in the top plot of Figure 3.10. When the pressure is considered, however, the increase in area causes a decrease in electrostatic pressure. Pressure is the quantity in which we are most interested, not total force, as the distributed pressures of orbital perturbations must be offset across the whole area of the structure. This suggests that electrostatic inflation can be achieved more easily for small area structures. The effect of changing the area on the system capacitance diminishes as the areas become larger than a few square meters, and the effect of area change on electrostatic pressure has nearly settled by areas of 4m^2. The effect of varying the separation distance on the capacitance matrix is very significant. Figure 3.11 illustrates the trends for a range of separation distances between membranes with a fixed potential and area. The electrostatic forces become larger as the two membranes are brought closer per Coulomb's law and because the system capacitance increases as two conducting bodies become closer. This result suggests that it will be most advantageous to have the two membranes very close. Small separation distances between membranes are also preferred when considering Debye Shielding, especially at LEO where Debye lengths can be close to the order of the separation distances considered here.

Figure 3.12 illustrates the relationship between the shape parameters of aspect ratio and total

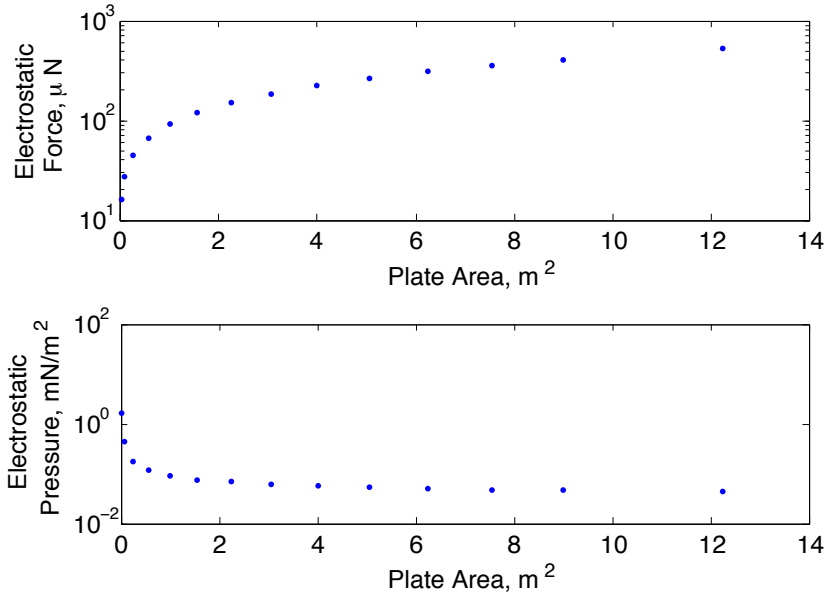

Figure 3.10: Numerical simulation of effect of varying structure area on the capacitance of the system, Fixed separation $2cm$, Fixed potential 1 kV

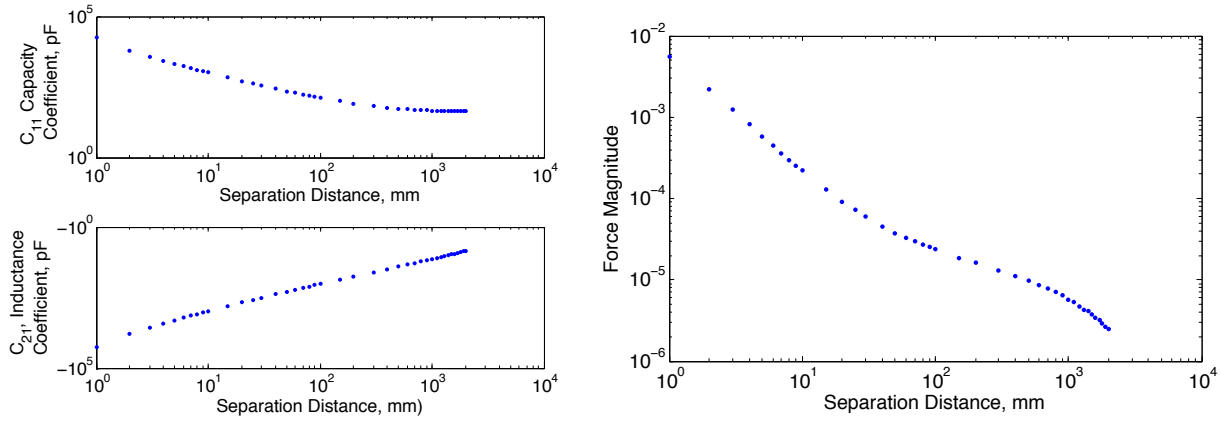

(a) Capacitance of two plate system

(b) Electrostatic force between two plates

Figure 3.11: Numerical simulation of effects of varying separation distance between membranes; Fixed area of 1 m^2, Fixed potential $1kV$

area of a two membrane sandwich structure to the minimum inflation pressure on the membrane. As expected, the larger the area of the structure, the lower the charge density becomes, thus the inflation pressure decreases. This limits the size of a solid sheet of membrane based on the required inflation pressure for the mission scenario. As the aspect ratio increases and EIMS becomes more

rectangular than square, the minimum charge density increases. This shows that to achieve higher inflation pressures with lower voltages, higher aspect ratios are more advantageous. The extrema of this idea leads to a ribbon-like structures.

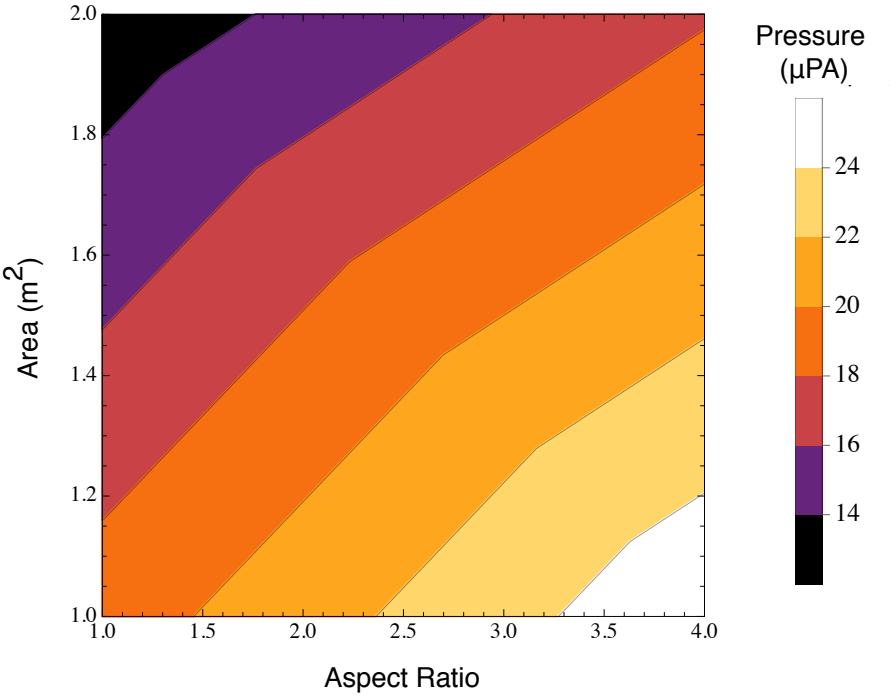

Figure 3.12: Minimum inflation pressure from 1 kV potential 2-sheet membrane structure

Similar to the ribboned structure as an alternative to the solid sphere, sheets with cut-outs can aid in inflation for this configuration. The cut-outs add regions (such as edges and corners) with higher charge densities that can be arranged where the charge density is the lowest for the solid membrane (and therefore inflation pressure is the lowest). Maxwell 3D is used to investigate the electrostatic benefits of the membrane material cut-outs in the structures which inflate well in demonstrations in both the laboratory and vacuum environment.

Figure 3.13(a) shows the geometry of the cut-out structures and Figure 3.13(b) shows a solid membrane, each showing the electrostatic charge distribution given the same applied voltage. Notice in Figure Figure 3.13(a) the increased charge distribution in the region of the membrane cut-outs. The magnitude of the charge distribution at these edges is nearly a 40% improvement of

the charge distribution in the same location of the solid membrane. This increased charge yields a larger electrostatic force and therefore, a greater inflation pressure. From Equation (3.7), a 40% increase in charge density is almost double the inflation pressure. A non-solid membrane concept can also enable further mass savings. A configuration with one solid membrane and an opposing cut-out membrane is also considered, such that the structure would still be functional as a drag device or star shade.

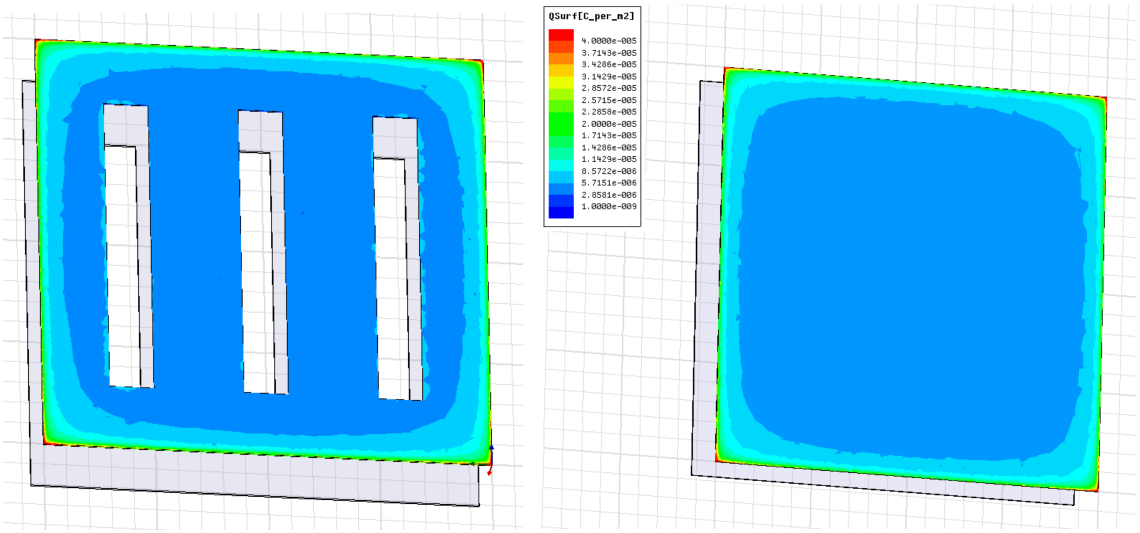

(a) 2-membrane structure with material cut-outs (b) Solid 2-membrane structures

Figure 3.13: Charge density plots for solid and cut-out configurations of the 2-membrane sandwich structure

3.3 Voltage Requirements for On-orbit Inflation under Orbital Perturbations

In this section, the pressure on an EIMS due to orbital disturbances is explored. As a first approach, orbital pressures in the normal direction are considered as the perturbing mechanism. For electrostatic inflation, potentials must be high enough to produce sufficient electrostatic inflation pressure in the normal direction for self-repulsion to offset the normal compressive pressures from differential gravity, solar radiation pressure, and atmospheric drag that would be experienced on orbit. Failure of the system occurs when the compressive pressures become greater than the inflation

pressure, thus collapsing or deflating the structure.

First, the GEO and LEO perturbations are quantified. The specific case of the two membrane sandwich structure is explored in-depth, examining magnitudes of orbital pressures and determining the required voltage to maintain inflation. The cases of a sphere and a cantilever tube under orbital perturbations are also briefly explored.

3.3.1 Orbit Perturbations

The orbital perturbations affecting EIMS depend on the orbit altitude. The magnitudes of pertinent orbital perturbations (solar radiation pressure, atmospheric drag and differential gravity) are quantified in the following subsections. The worst case scenario is studied to understand the largest orbit disturbance magnitudes that may be experienced. To quantify orbital pressure, perturbations are assumed to be distributed over the membrane surface in the normal direction.

Three different configurations of the 2-membrane sandwich structure are considered: orbit radial, along-track and orbit normal, as illustrated in Figure 3.14. The orbit radial configuration is defined as the large areas of each membrane to be nadir facing, as shown in Figure 3.14(a). In the along-track configuration, differential gravity has no effect on the sandwich structure and the atmospheric drag or solar radiation pressure are considered assuming a worst case alignment of the incident sun light or atmospheric particles with respect to the outer membrane surface. For the orbit normal configuration, differential gravity tensions the structure, solar radiation pressure is assumed worst-case, and drag has no effect.

3.3.1.1 Orbit perturbations in geosynchronous orbits

In the GEO environment, atmospheric drag is not a consideration, but differential gravity and solar radiation pressure are investigated. The effect of differential gravity depends on the orbit configuration as this perturbation will tension the structure in the membrane-normal direction in the radial configuration, compress the structure in the orbit normal configuration, and have no effect in the along-track configuration.

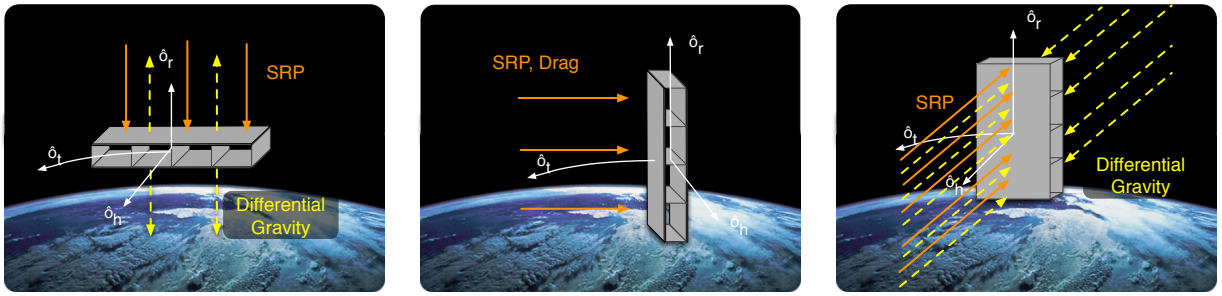

(a) Radial Configuration (b) Along Track Configuration (c) Orbit Normal Configuration

Figure 3.14: Possible orbital configurations of the membrane sandwich structure with worst-case compressive orbital perturbations illustrated.

The linearized differential gravity in the orbit radial configuration illustrated for the 2-membrane case in Figure 3.14(a) is given by Equation (3.14) where μ is the gravitation parameter, r_c is the radius from Earth, and d is the separation distance of the membranes.[52]. In this configuration the differential gravity force will aid in tensioning the structure, as the plate nearest to Earth will experience a stronger force due to gravity.

$$\delta F_{g,\text{radial}} \approx m \frac{3\mu}{r_c^3} d \tag{3.14}$$

For this study, mass is estimated from density, ρ and approximate material volume with area, A, and thickness, t:

$$m = \rho A t \tag{3.15}$$

75 gauge Aluminum coated Mylar, a possible material to be used for the proposed gossamer space structure, is used as the baseline material for this study. Thickness and density of this material are 19 microns and 1.40 g/cm^3, respectively. The mass contribution of the ribs is neglected here. To eliminate area dependence in the calculations, the differential pressure is calculated as follows:

$$\delta P_{g,\text{radial}} = \frac{\delta F_{g,\text{radial}}}{A} \approx \rho t \frac{3\mu}{r_c^3} d \tag{3.16}$$

For the along-track configuration shown in Figure 3.14(b) (large membrane area aligned with the velocity direction), the differential gravity force and pressure in the membrane normal direction

are essentially zero:

$$\delta F_{g,\text{along-track}} \approx \delta P_{g,\text{along-track}} \approx 0 \tag{3.17}$$

In the orbit normal configuration in Figure 3.14(c) (large membrane area facing the direction of the angular momentum vector), differential gravity will tend to compress the structure. The free-body diagram of this setup is shown in Figure 3.17(b). The linearized differential gravity force in this configuration is given by Eq. (3.18) [52].

$$\delta F_{g,\text{normal}} \approx -m\frac{\mu}{r_c^3}d \tag{3.18}$$

Similarly, the differential gravity pressure is:

$$\delta P_{g,\text{normal}} = \frac{\delta F_{g,\text{normal}}}{A} \approx -\rho t\frac{\mu}{r_c^3}d \tag{3.19}$$

The equation for the disturbance force from solar radiation pressure is given by: [53]

$$P_{\text{SRP}} = \frac{F_{\text{SRP}}}{A} = p_{\text{SR}}c_R \tag{3.20}$$

where

$$p_{\text{SR}} = 4.57e^{-6}\frac{N}{m^2} \tag{3.21}$$

is the nominal solar pressure at 1 AU from the sun, c_R is the reflectivity, and A is the area exposed to the sun. Note that the solar radiation pressure is independent of separation distance, area and orbit altitude. This pressure will therefore be identical at LEO and GEO orbits. It is assumed here that one membrane is fixed and the other membrane is experiencing pressure from solar radiation across the entire membrane surface. This is an assumption to provide a worst-case scenario of compression and not to describe the structural design.

These GEO perturbation force magnitudes are illustrated in Figure 3.15 for the three configurations of the 2-membrane sandwich structure. Figure 3.15(a) illustrates that the differential gravity forces are several orders of magnitude smaller than the solar radiation pressure. This result differs from the perturbation analysis for Coulomb formation flying or tethered Coulomb structures in which the differential gravity has a much larger effect. The cause for this difference is that both

separation distances and masses are orders of magnitude smaller for the gossamer 2-membrane rib structure. The much larger area to mass ratio causes the solar radiation pressure to dominate. As a result the tensioning effect of the radial differential gravity term provides negligible relief on the overall inflationary force requirement. Figure 3.15(b) illustrates that the minimum required inflationary pressure is a fixed value for the along-track configuration. Figure 3.15(c) shows that the disturbing pressure magnitudes in the orbit normal configuration are nearly identical to the radial configuration, with the exception that in the normal configuration, differential gravity tends to compress the structure instead of providing tension, as in the radial configuration. Again the solar pressure dominates the required inflationary force for this GEO configuration.

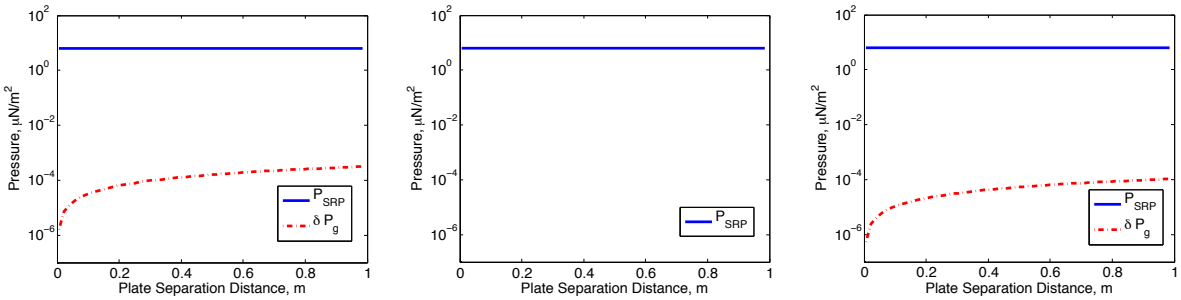

(a) Radial Configuration (b) Along Track Configuration (c) Orbit Normal Configuration

Figure 3.15: Magnitudes of disturbance pressures in the radial, along-track, and normal configurations at GEO, mass $m = 0.01kg$

3.3.1.2 Perturbations in Low Earth Orbits

Next, a membrane structure which is flying at LEO altitudes is considered. In addition to the differential gravity pressures and solar radiation pressure expressed in Equations (3.16), (3.19), and (3.20), the perturbation from atmospheric drag is also considered. The drag force at these altitudes cannot be neglected as a perturbation as it may be at GEO altitudes. The force on the leading plate is calculated with:[53]

$$F_D = -\frac{1}{2} C_D A \rho v_{\text{rel}}^2 \frac{\mathbf{v}_{\text{rel}}}{|\mathbf{v}_{\text{rel}}|} \tag{3.22}$$

Again, to eliminate area dependence, the differential pressure from drag is calculated with:

$$P_D = -\frac{1}{2} C_D \rho v_{\text{rel}}^2 \frac{\mathbf{v}_{\text{rel}}}{|\mathbf{v}_{\text{rel}}|} \tag{3.23}$$

This force, however, is only considered for the along-track configuration. Here the large area of one plate is bombarded by the rarified atmospheric particles, while the other plate is protected in the wake of the leading plate. The resulting differential drag force on the leading plate tends to compress the structure. In the orbit radial and normal configurations the differential drag forces are negligible as no significant area is presented relative to the incoming rarified atmosphere. For the 2 membrane structure with an area of 0.5 m^2 and a mass of 0.01 kg, a study is performed to determine the altitude at which the drag force diminishes versus the differential solar radiation forces. Values for atmospheric density are calculated using the MSIS-E-90 Atmospheric Model.

As shown in Figure 3.16, below approximately 500km the atmospheric drag pressure is the dominating perturbation. Above this altitude, the density becomes too low to have an appreciable effect. Near and below this altitude, the required charge densities and corresponding potentials to inflate a membrane structure must take the differential atmospheric drag into careful consideration. At low altitudes, large area EIMS yield large atmospheric drag forces, thus making it viable as a deployable drag de-orbiting device.

3.3.2 Two-Membrane Sandwich Structure under Orbital Pressures

The investigation of required electrostatic potential for inflation presented here is limited to 2-layer gossamer structures in a sandwich-like configuration. This study makes the simplifying assumption that the outer membranes are flat and rigid, and therefore ignore displacement effects such as geometric stiffening and interactions between deforming structure and electrostatic forcing. For simplified modeling purposes, lightweight membrane ribs between the membranes are assumed to provide tensile forces between the layers of the structure. Additionally, it is assumed that there is no rotation of the structure. Rather, the work here focuses on disturbances that can cause an EIMS surface normal compression and investigates what potentials are required to compensate.

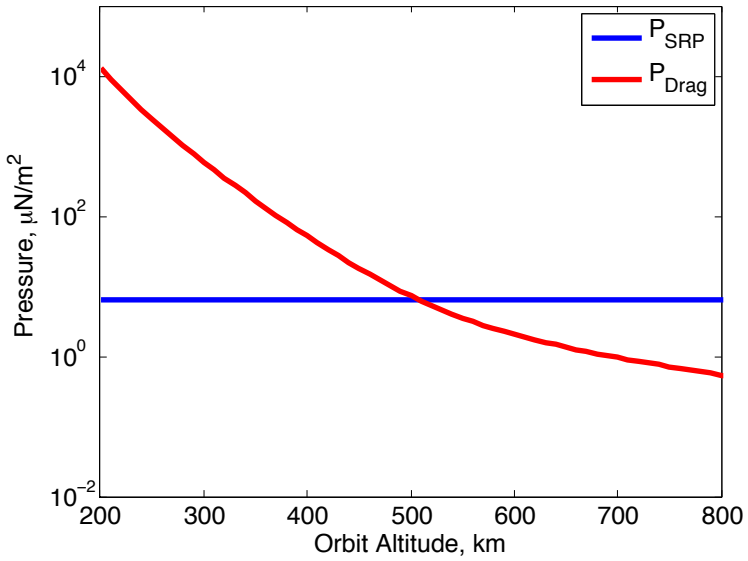

Figure 3.16: Disturbance pressure magnitude as a function of altitude in LEO

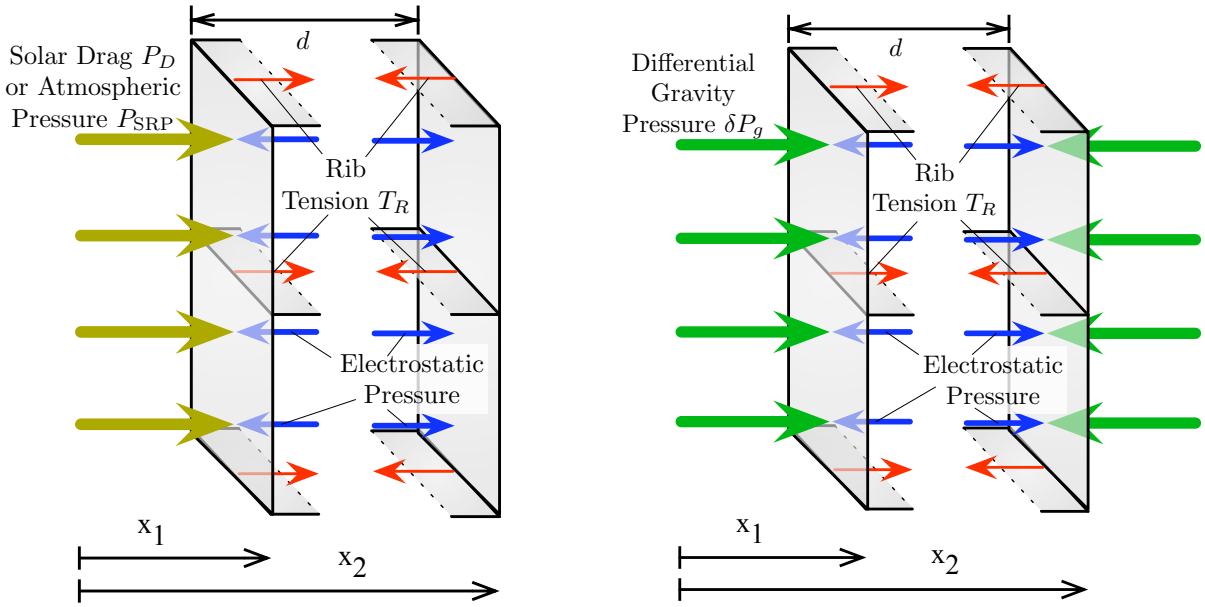

(a) Solar Radiation and Atmospheric Drag Pressure Acting on a Single Membrane causing an inertially accelerating EIMS system

(b) Differential Gravity Configuration Compressing Both Membrane Surfaces with EIMS inertially fixed

Figure 3.17: Force Diagrams of the EIMS Membrane-Normal Pressures and Forces.

Figure 3.17 shows force diagrams of the disturbance pressures and forces acting on EIMS for the cases of a disturbance acting on a single membrane (solar radiation or drag) and a dis-

turbance pressure which compresses both membranes simultaneously (differential gravity). The solar radiation pressure and drag pressure are assumed to be in a worst-case alignment that causes compression of the membrane structure. The internal rib structure is shown as holding the system in tension as the electrostatic pressure causes inflation between the membranes. For the analysis, failure of the structure is defined as compression of the two membranes due to disturbance pressures. Nominally the internal inflationary forces are larger than the external disturbance forces. Here the rib forces, F_R, are positive and maintain a fixed separation distance, d, thus keeping EIMS rigid. Unless the external disturbance forces are large enough to cause the rib tensions to be negative (compressive), EIMS maintains a fixed shape as it translates due to a net external disturbance. Of interest is what minimum electrostatic potentials are required to compensate for the membrane-normal orbital disturbance such that separation distance remains constant. At this critical potential the rib tensions, T_R, are zero, just avoiding the shape deformation.

The relationship between the minimum required electrostatic inflation pressure and the orbital perturbations is studied by examining the dynamics of the two membrane system shown in Figure 3.17. For a system with disturbance pressures acting on one membrane only (i.e. solar or atmospheric drag), the equations of motion for membrane 1 and membrane 2 are:

$$m\ddot{x}_1 = F_{\text{disturb},1} - F_e + F_R \tag{3.24a}$$

$$m\ddot{x}_2 = m\left(\ddot{x}_1 - \ddot{d}\right) = m\ddot{x}_1 = F_e - F_R \tag{3.24b}$$

where m is the membrane mass, F_e is the electrostatic force, F_R is the rib force, and $F_{\text{disturb},1}$ is the one-sided disturbance force. These simplified equations are a good approximation of the first-order EIMS compression dynamics as EIMS is assumed to not be rotating in this structure. Further, these equations are also suitable for an EIMS in Earth orbit if the structure is assumed to not be rotating relative to the local-vertical, local-horizontal (LVLH) frame. If the structure does not deform due to the external disturbance, the separation distance, d, remains constant. Also, the rib force, F_R will be zero in the case of minimum electrostatic pressure. Substituting Eqs. (3.24a) into

(3.24b) yields the relationship:

$$F_e = \frac{F_{\text{disturb},1}}{2} \tag{3.25}$$

Because the one-sided disturbance is causing EIMS to accelerate, the electrostatic inflation force must be half of the disturbance force.The previous scenario applies for solar radiation and atmospheric drag disturbances. For differential gravity disturbances, however, the disturbance pressure acts on both membranes. By the same approach, the required electrostatic for relationship for this scenario is found to be:

$$F_e = F_{\text{disturb},2} \tag{3.26}$$

This relationship between the forces will be used to determine the minimum required charge densities and voltages to maintain a constant separation between membranes under the compressive pressures of worst-case orbital perturbations.

Based on the relationship between the required electrostatic forces and these disturbance forces is expressed in Equations (3.25) and (3.26), the required pressure expressions are thus obtained for one or two sided disturbances (respectively):

$$P_{req} = \frac{P_{SRP} + P_D}{2} \tag{3.27a}$$

$$P_{req} = P_g \tag{3.27b}$$

All disturbance pressures (here, equation (3.27a) and (3.27b)) are added and subsequently used in Equation (3.7) to determine approximate minimum required charge densities at GEO and LEO.

3.3.3 Required voltages for orbital perturbations: 2-membrane EIMS at GEO example case

To apply the development presented above, an example of the required voltage for a two-membrane electrostatically inflated structure with 1m^2 area in the along-track configuration of a GEO orbit is considered. To summarize the procedure, first the normal orbital perturbations are

determined. Using Eqn. (3.7), the determined perturbations yield the required charge density to maintain inflation. Maxwell 3D is then used to draw appropriate geometries, solve the full electrostatic field solution, and determine the voltage which yields the required minimum charge density.

For the given orbit and configuration, the potentials necessary to offset perturbing orbital pressures are shown in Figure 3.18 for a range of membrane separation distances. From Figure 3.18 it can be seen that the required potential is only on the order of a few hundred volts. This is a very small voltage compared to the kiloVolt levels that have been achieved through active charging in GEO. Even natural charging levels at GEO during eclipse can far exceed this level.

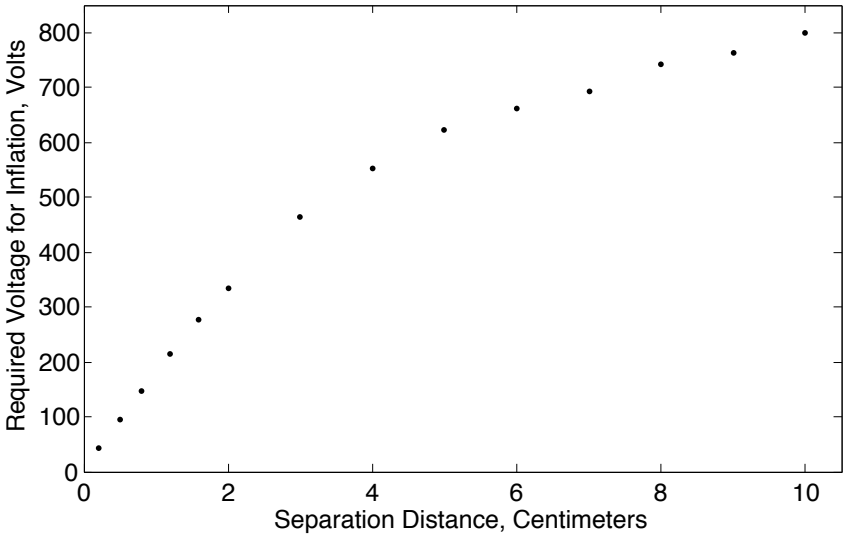

Figure 3.18: Required voltage for offset of compressive orbital perturbations at GEO of a sandwich structure for a range of separation distances; Area = 1 m^2

The relationship between voltage and minimum charge density is shown in Figure 3.19 for two membranes with areas of $1m^2$ at a fixed separation distance of 20mm. This plot illustrates how voltage requirements scale as the orbital perturbation pressures increase from GEO to different LEO altitudes. Figure 3.19 shows that the relationship between these two parameters appears linear over the domain of voltages investigated. As the drag increases in lower LEO orbits, the

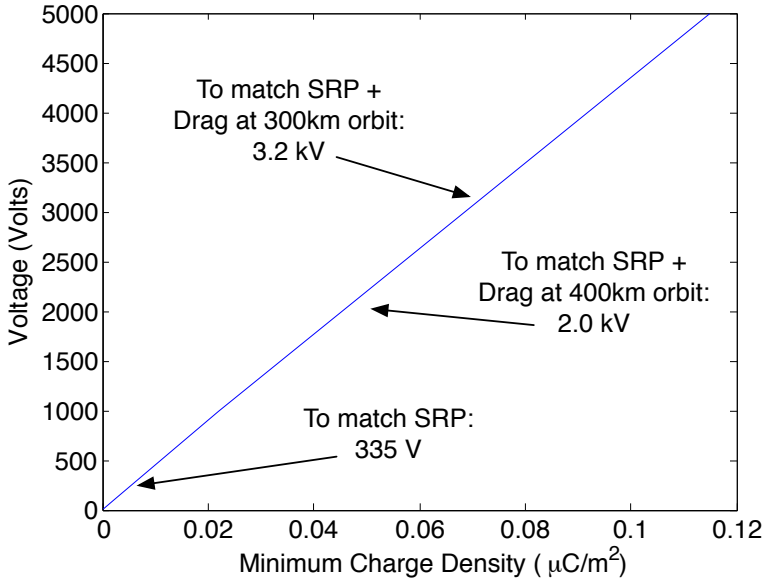

Figure 3.19: Numerical evaluation of the relationship between voltage applied to the membranes and the minimum value of charge density, shown with $A = 1m^2$ and $d = 20mm$

required voltages to offset this pressure remains in the few kilovolt range, which remains below the previously achieved on-orbit charging levels.

It should be noted that the voltage that would be used to inflate the structure would be greater than just this equilibrium voltage. These results reflect a minimum that would be necessary to exactly offset orbital perturbations, but not provide any stiffness beyond this. Additional charging would be desired to provide more stiffness, which would be especially desirable during attitude maneuvers which may deform the structure. The procedure described in this paper will also be applicable to determine the voltages to offset the pressures encountered during attitude maneuvers. What is important here is that this analysis provides a good estimate of the order of magnitude of required potentials for maintaining inflation and these required potentials are feasible for charging in a LEO or GEO environment.

3.3.4 Electrostatic inflation of a membrane sphere under orbital perturbations

Similar to the above study for the 2-membrane structure, a study was performed to understand the voltage requirements for an electrostatically inflated sphere to offset orbital perturbation which may tend to collapse the structure. The two orbit perturbations which may affect a spherical EIMS are solar radiation pressure and atmospheric drag.

Using the mathematical development from the above section for the electrostatic sphere, inflation pressures are studied as compared to orbital perturbation magnitudes. Figure 3.20 illustrates the relationship between voltage and resulting inflation pressure for a 1-meter sphere. For comparison, the magnitude of the perturbing pressure of solar radiation is shown. The voltage required to overcome solar radiation pressure is only approximately 1.2 kV, a feasible magnitude, especially for GEO orbits.

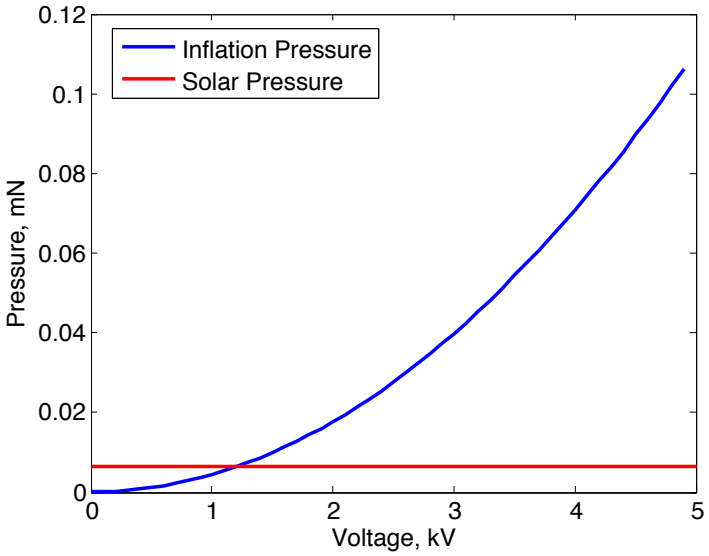

Figure 3.20: Electrostatic inflation pressure and voltage relationship for a 1-meter sphere

Examining the required pressure to offset solar radiation pressure across a range of sphere radii, it is seen that the required voltage remains feasible up to large craft sizes. This is shown in Figure 3.21.

Again, these quick calculations for required voltage consider only the minimum inflation

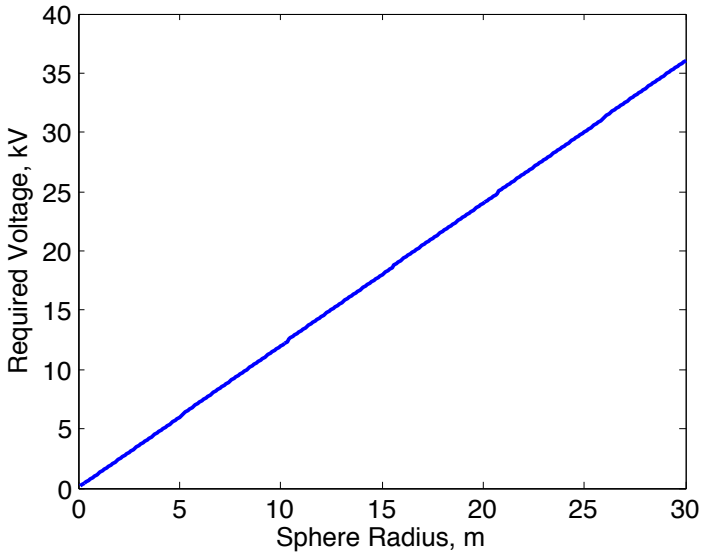

Figure 3.21: Voltage required to offset solar radiation pressure for a range of sphere sizes

pressure required. For stiffness purposes, the desired voltages would be higher. It will be necessary in the future to study the effect of attitude maneuvers on the inflated structure. For now, it is assumed that an attitude maneuver could collapse the structure, but re-inflation would take place upon the completion of the maneuver. The tolerance of motion in response to a maneuver will relate to mission requirements.

3.3.5 Electrostatic inflation of a cantilever cylinder under orbital perturbations

In this section, an inflated cantilever tube undergoing a perturbation is considered. The aim is to find an appropriate value for inflation pressure and subsequently the required voltage that is needed to withstand the perturbation to some maximum deflection. A method based on a gas inflated cylinder is used as the approach to estimate required electrostatic pressure.

Reference 54 presents an approach for a gas-inflated membrane based on the Timoshenko beam model that uses finite rotation kinematics. An example is presented of the bending of the cantilever beam which is extended to the electrostatic inflation scenario. While pressures for gas inflation are considerably larger than with electrostatic inflation, the assumptions in the

development are still met.

The equations in Reference 54 are derived from virtual work principles for the inflatable beam undergoing bending in the xy-plane with inflation pressure and an external load acting in combination.[54]. An illustration of the problem is shown in Figure 3.22.

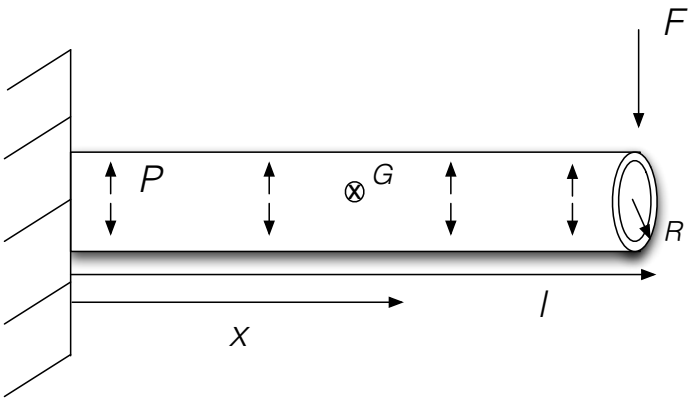

Figure 3.22: Diagram of cantilever tube geometry

It is assumed that some disturbance force is acting at the end of the pressurized tube. The equation for deflection, y, of a cylindrical tube inflated to pressure P and subjected to force F is given in Equation (3.28).

$$y(x) = \frac{F}{(E + P/S_0)I_0}\left(\frac{l_0 x^2}{2} - \frac{x^3}{6}\right) + \frac{Fx}{P + kGS_0} \tag{3.28}$$

where S_0 is the cross sectional area;

$$S_0 = \pi(R^2 - R_{inner}^2) \tag{3.29}$$

G is the location of the centroid;

$$G = \frac{L}{2} \tag{3.30}$$

and I_0 is the second moment of area:

$$I_0 = \pi\left(\frac{R^4}{4} - \frac{R_{inner}^4}{4}\right) \tag{3.31}$$

For this analysis, the deflection at the tip is of interest, therefore the equation can be simplified to Equation (3.32).

$$y(x) = \frac{Fl_0^3}{3(E + P/S_0)I_0} + \frac{Fl_0}{P + kGS_0} \tag{3.32}$$

Notice that the pressure is included in the denominator of both terms. This reflects that the inflation pressure is modifying both the Young modulus and the shear modulus.[54] The parameter k is the correction shear coefficient. From reference 54, this value is found in literature and a value of 0.5 corresponds to a thin circular tube.

If some maximum deflection is chosen (for example based on mission requirements), the pressure can be solved for using a root solving program, such as mathematica. With the required pressure quantified, Equation (3.7) is used to determine the required minimum charge density. Maxwell 3D is subsequently used to related the charge density requirement to a voltage requirement, which is the end goal of the procedure.

An example analysis is provided here to illustrate the procedure. Values for the elastic modulus and thickness are based on the typical membrane materials considered for EIMS. The geometry of a thin walled cylinder is used to calculate surface area (S_0) and second moment of area (I_0). These and other chosen geometric parameters are shown in Table 3.1.

Table 3.1: EIMS cylindrical tube geometric simulation parameters

Parameter	Value
Elastic Modulus	3e-9
k	0.5
Thickness	20 μm
Length	0.5 m
Radius	0.04 m

A disturbance force of 1 mN is chosen for this simulation. An allowable deflection is chosen arbitrarily to be one tenth of the length of the cylinder. For these parameters, Mathematica is used to solve for a value of the pressure. Two solutions are yielded and the positive value is the result for required inflation pressure.

For the simulation using the parameters of Table 3.1, allowing a deflection of L/10 (5 cm) from an applied end load of 1 mN, the required inflation pressure is 0.01 Pa. This pressure value corresponds to a charge density of 8.85e-12 C/m^2. This does however, assume a uniform inflation pressure. Since the charge distribution and thus inflation pressure are non-uniform, the required charge density is a minimum for anywhere on the cylinder. This can be determined using Maxwell 3D, which shows that a voltage of 4.3 kV is required to have the determined minimum charge density. The results are summarized in Table 3.2.

Table 3.2: EIMS cylindrical tube simulation results

Parameter	Value
Force	1 mN
Pressure	0.1 Pa
Charge Density	8.85e-12 C/m^2
Voltage	4.3 kV

This simulation shows that an electrostatically inflated cylinder can withstand significant disturbance pressures. It is noted that the required pressure and voltage are very sensitive to the allowable deflection at the tip of the cylinder. More leniency in this requirement eases the required voltage significantly. It should be noted, however, that Equations (3.28) or (3.32) are linearized and must follow the assumption of small deflections. It is also considered that during a large disturbance, such as an attitude maneuver, the EIMS could be allowed to deform significantly and then return to the nominal configuration post-maneuver. This would further relax the voltage requirements for inflation.

Chapter 4

EIMS operating in a space plasma

This chapter addresses topics related to the second research question: what are necessary conditions for a meter-scale structure to maintain shape via electrostatic inflation in a plasma. In thi1er, the effect of the plasma on the electrostatic forces which enable the inflation of EIMS is considered. First, the Debye shielding phenomena is reviewed. Based on the Debye shielding effects, EIMS applicability in different orbit regions is discussed. While the plasma at geosynchronous altitude has little effect on employing electrostatic inflation, the low earth orbit plasma presents challenges for EIMS due to the strong shielding effects of the dense plasma. Then, an assumption made in the classical Debye shielding development is reviewed and it is shown through numerical simulation that actual electrostatic shielding is less than predicted when high spacecraft potentials are employed. This phenomena is termed 'effective' Debye shielding and trends are explored based on craft size, craft potential, and plasma conditions. Effective Debye lengths can be orders of magnitude larger in LEO and also significantly larger in GEO. Lastly, the effect of a charge flux on an inflated membrane structure are explored through experiment. Experiments show that EIMS can remain as a stable structure in a charge wake, though interesting structure-charge flux vibrations were observed.

4.1 The Plasma Environment of Effects on EIMS

The space environment is not a pure vacuum, rather it is occupied by charged particles in the state of a plasma. This environment exists because the energy of gases exceeds the ionization

energy, thus resulting in an ionized gas of free electrons and ions [55]. The plasma affects spacecraft both by causing spacecraft to attain non-zero potentials (described further in Chapter 5) and by shielding the potential around the craft. A variety of plasma conditions exist depending on orbit altitude or location in the solar system.

4.1.1 Debye Shielding

In the plasma environment of space, electrons and ions rearrange in the presence of a disturbing electric field to maintain macroscopic neutrality [20]. This phenomena, known as Debye shielding, will effectively shield the electrostatic field of a charged object in a plasma, such as an electrostatically inflated structure. To determine the potential near a charged object in a plasma, the number density of charged particles must be known. An expression for the electron density and ion density are given in Eqs. (4.1) [20], where k is the Boltzmann constant, T is temperature, ϕ is the potential due to a charge, and n_0 is a constant particle density where $n_e(\infty) = n_i(\infty) = n_0$.

$$n_e = n_0 e^{\frac{e\phi}{kT_e}} \tag{4.1a}$$

$$n_i = n_0 e^{-\frac{e\phi}{kT_i}} \tag{4.1b}$$

Using these definitions for particle number densities, the electrostatic potential is given by Gauss's law:

$$\nabla^2\phi = -\frac{\rho}{\epsilon_0} = \frac{n_0 e}{\epsilon_0}\left(e^{-\frac{e\phi}{kT}} - e^{\frac{e\phi}{kT}}\right) \tag{4.2}$$

This classical development continues under the assumption that the potential energy of the field is much smaller than the kinetic energy of the particles, or $(e\phi \ll kT)$. This assumption yields the simplified expression:

$$\nabla^2\phi = \frac{2}{\lambda_D}\phi \tag{4.3}$$

where the parameter, λ_D is the Debye Length. The Debye length describes the distance at which a charge is essentially shielded by the plasma if $(e\phi \ll kT)$ is true. The Debye length is determined by plasma conditions through:

$$\lambda_D = \left(\frac{\epsilon_0 kT}{n_e e^2}\right)^{\frac{1}{2}} \tag{4.4}$$

where e is the elementary charge. This particular form of the Debye length computation assumes that the negative plasma electrons dominate the electrostatic charge shielding. Table 4.1 shows nominal Debye lengths at LEO and GEO. The GEO parameters are based on measurements from the ATS spacecraft (References 56 and 57). The LEO data is taken from Reference 31.

Table 4.1: Representative GEO & LEO single Maxwellian plasma parameters and Debye lengths

Conditions	$\mathcal{T}_e$ [eV]	n_e [cm^{-3}]	λ_D [m]
LEO Nominal	0.2	1×10^5	**0.01**
GEO Nominal	900	1.25	**200**

The simplified form of Poisson's equation (Equation (4.3)) has a well known analytical solution for the potential in a plasma surrounding a point charge, q, (or a charged sphere with total charge q) in spherical coordinates given by:

$$\phi = \frac{k_c q}{r} e^{-\frac{r}{\lambda_D}} \tag{4.5}$$

This equation can be compared to the Laplace (or vacuum) potential equation, which is the limit of the Debye potential equation for large Debye lengths:

$$\phi = k_c \frac{q}{r} \tag{4.6}$$

Taking the gradient of the potential function of Eq. (4.5) yields the spherically symmetric electrostatic field for $r \geq R$:

$$E = -\nabla\phi = \frac{k_c q}{r^2} e^{-\frac{r}{\lambda_D}} \left[1 + \frac{r}{\lambda_D}\right] \tag{4.7}$$

As is the potential, the electrostatic field of a charged body in a plasma is also bound by the lower limit of this Debye-Hückel field and the upper limit of the vacuum field.

The Debye shielded electrostatic force experienced by a 2nd point charge q_2 (due to point charge q_1)is derived by taking the gradient of Equation (4.5):

$$F = \nabla\phi \cdot q = \frac{k_c q_1 q_2}{r^2} e^{-\frac{r}{\lambda_D}} \left[1 + \frac{r}{\lambda_D}\right] \tag{4.8}$$

While this force computation is only valid for point charges, and not the flat membrane models considered in this research, Eq. (4.8) provides insight into how the plasma Debye length can limit the electrostatic actuation. No simple analytical expression describes the electrostatic force between two plates, therefore numerical simulations of plasma conditions will be required for these more complex geometries.

It should be noted that the force is a function of the gradient of the potential. Therefore if there is a steep gradient in potential due to aggressive Debye shielding, the electrostatic force can actually be larger than the vacuum force. The increase in force may be beneficial for EIMS operating at very close distances.

4.1.2 Orbit Regions Applicable for Electrostatic Inflation

Debye shielding can have a significant impact on the use of electrostatics in a plasma environment. In the Low Earth Orbit region, Debye lengths are typically on the order of milli- or centimeters, depending on the orbit altitude. Table 4.2 shows the extremes of Debye lengths experienced in LEO at an orbit altitude of approximately 350 km, as predicted by the International Reference Ionosphere model and reported in Reference 58.

In earlier work on Coulomb control of free-flying charged spacecraft, or the electrostatic deployment of tethered Coulomb structure concepts over several meters, this aggressive Debye shielding prevents such concepts from being considered at LEO.[32,52] However, with the electrostatically inflated membrane structures, even with surface areas of multiple square meters, the electrostatic force only has to occur across the membrane layer separation distance d which can be on the order of centimeters. If the separation distance between the membrane layers of a sandwich structure in LEO is greater than a few millimeters or centimeters, or of the order of the local Debye length, then the membranes would not experience a significant electrostatic force and the inflation concept would not be feasible. This argument assumes that the membrane potential ϕ satisfies the condition that ($e\phi \ll kT$). It has been shown that high potentials which violate this condition yield reduced Debye shielding effects, with LEO Debye Lengths raised to several decimeters,[59] as

is further explained in the following section. Thus, if small membrane separations, d, of less than a centimeter are assumed, then even with the aggressive Debye shielding assumptions electrostatic inflation is still feasible at LEO.

Dissimilar to earlier work on free-flying charged spacecraft where the formation size is directly limited by the electrostatic force drop off with separation distance, the membrane structure can scale to comparatively large dimensions. With EIMS, it is not necessary for the electrostatic repulsion to occur across the entire membrane surface with width and length dimensions on the order of meters, only across the much smaller separation distance d with dimensions of centimeters.

In the GEO regime, the Debye length is generally on the order of hundreds of meters. However, these values vary drastically with the solar storm activities heating up part of the plasma sheath, or pushing the lower and colder plasma pause conditions into the GEO altitudes.[60,61] The upper and lower bounds of possible geostationary Debye length values are shown in Table 4.2, as well as the nominal value. These Debye lengths are based on observations from the ATS-5 and ATS-6 spacecraft given in References 56 and 57. The small separation distances between proposed membrane structures compared to the comparatively large Debye lengths yield nearly negligible effects from the shielding. This is true even for the very worst GEO plasma weather conditions being considered.

The LEO Debye lengths[62] illustrate that electrostatic inflation will require small membrane separation distances. However, because the potentials (kilovolts) are large in comparison to the cold LEO plasma temperatures, the effective Debye lengths are multiple times larger. These values do not indicate that EIMS is feasible at LEO, but it can be considered if a compatible set of potentials and separation distances are used.

Table 4.2: Range of Feasible Plasma Debye Lengths

	Smallest λ_D	Nominal λ_D	Largest λ_D
LEO Environment	0.002 m	0.005 m	0.013 m
GEO Environment	4 m	200 m	743 m

4.2 Effective Debye Shielding

The Debye-Hückel potential field is an analytic expression that is derived by assuming $eV \ll kT$ holds. Table 4.1 quantifies the spacecraft surface potential required to match the plasma thermal energy, i.e. $eV = kT$.

Table 4.3: Craft voltages violating the ($eV \ll kT$) assumption

Plasma conditions	Debye length [m]	Craft potential [V]
LEO Nominal	0.01	0.2
GEO Quiet	4	3
GEO Nominal	200	900

If the craft potential is much less than plasma energy ($eV \ll kT$), than the Debye-Hückel model of Eq. (4.5) is a good approximation. If the craft potential is significantly greater than the plasma ($eV \gg kT$), then the plasma-based potential field is actually closer to the vacuum model of Eq. (4.6).

For electrostatic inflation and other Coulomb applications in GEO and LEO orbit regimes, the ($eV \ll kT$) assumption in the analytical development of the Debye-Hückel potential is quickly violated. The Debye-Hückel potential of Eq. (4.5) serves as a lower bound for the actual potential decay from a charged body in a plasma while the the Laplace potential of Eq. (4.6) serves as an upper bound. One method to analytically compute the force within this range with higher accuracy is with an **effective Debye length**, as proposed in Reference 63 for the charged asteroid scenario. Murdoch in Reference 63 computes effective Debye lengths for analyzing the capabilities of orbit altering and impact deflection of a NEO asteroid. Their study indicates, with particular examples, that the Coulomb application works best for 100 m size NEO, charges of 20 kV and mission durations up to 20 years. In this NEO application the interplanetary Debye length is 7.4 m, however with potentials up to 20 kV, Murdoch calculates that the effective Debye lengths can be as great as 349 m.[63] This is a scaling increase of approximately 50, and can result in significantly less plasma shielding of the Coulomb forces.

This effective Debye length study by Murdoch is used as a basis here to analyze the force production in a plasma for small spacecraft operating in close proximities in Earth orbit plasmas. This effective Debye length is larger than the true Debye length and consequently reduces the screening of the potential field. For charged craft in the dense plasma of LEO it is shown that the effective Debye lengths are scaled to the meter level. It is demonstrated that this improves the Coulomb force magnitudes and makes them viable for applications such as inflation of membranes at centimeter level separations.

To incorporate the effects of high voltage bodies on the local plasma, the effective Debye length ($\bar{\lambda}_D$) simply replaces the classical Debye length in the electrostatic force equations. This effective Debye length is linearly proportional to the Debye length using a scaling parameter α using the relationship:

$$\bar{\lambda}_D = \alpha \lambda_D \tag{4.9}$$

The effective Debye length, given in Eq. (4.9), is numerically computed based on plasma conditions, craft size, and potential as demonstrated in Reference 63. The benefit of the approach using this effective Debye length is that it allows efficient analytic force computations with improved accuracy.

In this study, the effective Debye lengths are obtained from numerical solutions of the Poisson-Vlasov equation in the OML (Orbit Motion Limited) limit. Solutions are obtained for the E-field surrounding a charged sphere in a plasma. An α scalar value described by Eq. (4.9) is determined by fitting an effective Debye shielded E-field model to the numerical solution across distances up to several Debye lengths from the sphere. The E-field model used is based on Eq. (4.7), using effective Debye lengths:

$$E = \frac{k_c q}{r^2} e^{-\frac{r}{\alpha \lambda_D}} \left[1 + \frac{r}{\alpha \lambda_D} \right] \tag{4.10}$$

The effective Debye length is computed for force computations in Earth plasmas for a range of craft sizes and craft potentials. The nominal GEO plasma conditions are not investigated as the plasma shielding in a Debye length of 200 m is minimal and the Debye-Hückel model closely

resembles the vacuum values.

4.2.1 Effective Debye Length Trends

Factors which affect the effective Debye length include the plasma Debye length, craft radius, and the voltage level on the craft. Numerical simulations were performed using ranges of each of these parameters to understand the trends in α-parameter. Figure 4.1(a) displays the variation of the α factor over a range of craft sizes and craft voltages.

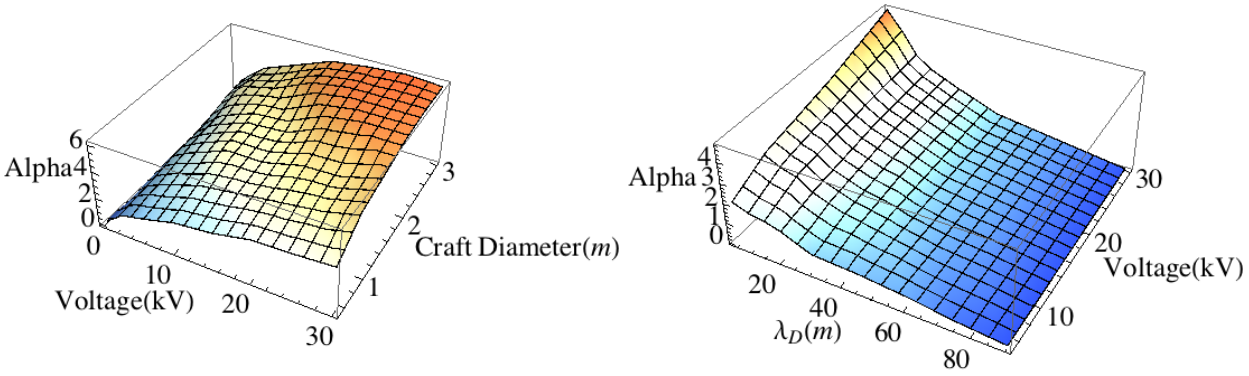

(a) Craft diameter and potential in a fixed quiet plasma ($\lambda_D = 4$)

(b) Craft potential and Debye length for a fixed diameter of 1 m

Figure 4.1: Trends in Alpha parameter for effective Debye lengths in a GEO plasma

Figure 4.1(a) clearly illustrates that larger craft radii and higher potentials yield larger effective Debye lengths. The craft voltage trend occurs because as the assumption ($e\phi \ll kT$) is further violated, the shielding is reduced. There exist limitations on craft voltage due to power requirements and limitations on craft size due to launch constraints, but this study demonstrates that electrostatic forces are more effective with larger craft and higher potentials.

Figure 4.1(b) shows the variation of the effective shielding parameter as a function of Debye length and craft voltage for a sphere with a 1m diameter. The extreme case of a quiet GEO plasma Debye length near 4 m and a high craft voltage of 30 kV, the effective Debye length is more than 5 times the predicted Debye length. As the Debye length approaches 100 m, the effective Debye length is close to the predicted Debye-Hückel Debye length, therefore α approaches a value of one.

With a Debye length of 100 m, the Debye shielded force is nearly the same as the vacuum force at distances on the order of a few tens of meters. Interpolation of the data shown on these plots can be used to determine the effective Debye lengths for different combinations of craft voltage, Debye lengths, and craft sizes.

4.2.2 GEO Effective Debye Lengths

In this section, electrostatic fields surrounding a charged craft in a quiet GEO plasma are examined in more detail. Figure 4.2 compares the vacuum E-field, the analytical E-field model using both classic Debye length and the effective Debye length, and the numerical simulation results. Two cases are illustrated: craft voltage of 1kV (top) and a craft voltage of 30kV (bottom). In both cases, the numerical solution has a stronger E-field than classically predicted, but have an upper bound of the Laplace potential of Eq. (4.6) (vacuum case). As the craft voltage increases, the actual E-field values stray further from the the classic Debye-Hückel model and approach the vacuum E-field.

4.2.2.1 Parametric α-Parameter Relationship

For Coulomb force modeling, a parametric relationship between the effective Debye length α-parameter and input parameters of craft voltage and craft diameter is desired. This allows for quick modeling of the E-fields or forces surrounding the craft with improved accuracy from classic Debye length solutions.

A nonlinear model in the form of $V \cdot poly(V_C, D_C) + (1 + e^V) \cdot poly(V_C, D_C)$ was fit to α-parameter values across a a range of craft voltages sizes for the quiet GEO Debye. The coefficient of determination, $\mathcal{R}^2$, was used to measure the goodness of fit for the model. A nonlinear fit of the alpha parameter data is shown in Eq. (4.11) as a function of craft voltage, V_C and craft diameter, D_C. The $\mathcal{R}^2$ value of this fit is 0.995, very near the maximum value of 1, therefore this model was considered a satisfactory prediction of the alpha parameter for effective Debye lengths. The regression equation is as follows:

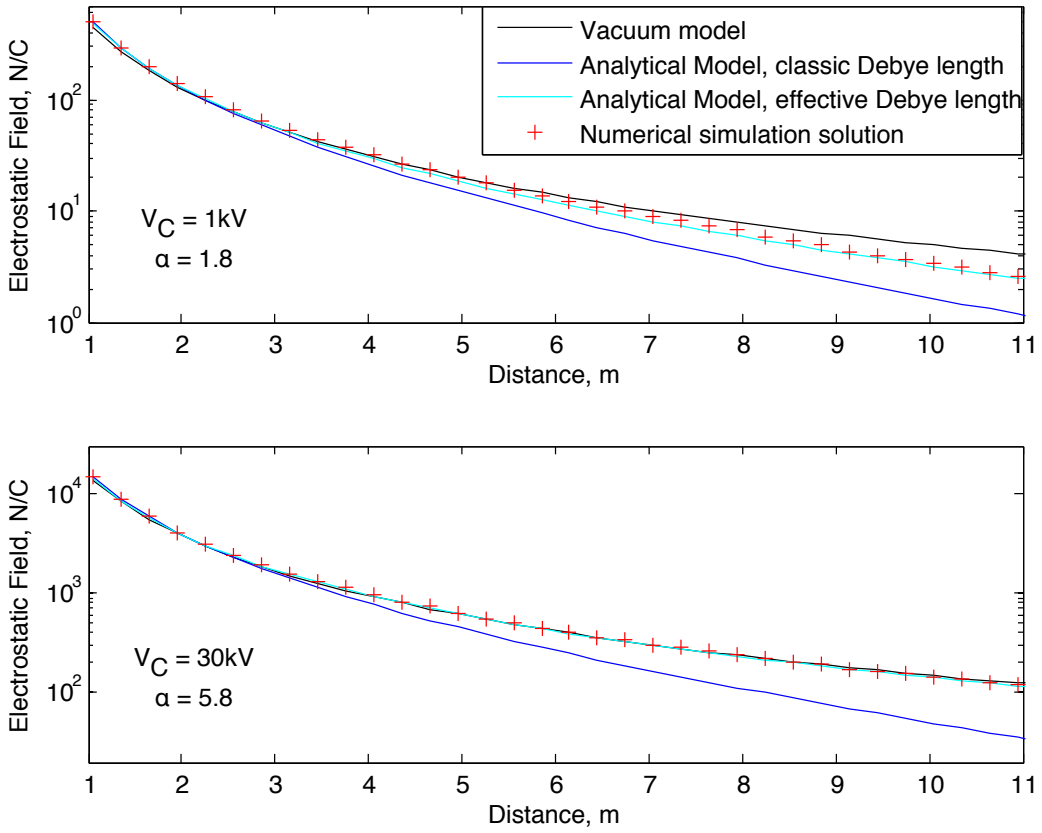

Figure 4.2: Comparison of classic E-field models with the effective Debye model; GEO plasma, $\lambda_D = 4m$

$$\alpha = 1 + 0.490V_C - 0.00322V_C^2 + 0.00446V_C D_C + \\ \left(1 - e^{-0.576V_C}\right)\left(-0.1045 - 0.289V_C + 1.086D_C\right) \tag{4.11}$$

This nonlinear model forces the α parameter to converge to a value of 1 as the craft voltage approaches zero. As the voltage approaches zero, the $(e\phi \ll kT)$ rule is no longer violated, thus the classic Debye-Hückel model is satisfactory for predicting E-fields and forces. The form of this nonlinear model was chosen as a combination of a quadratic polynomial term, which well models the behaviors at higher voltages (5 - 30 kV), and an exponential term which models the low voltage behavior as α converges to one. This equation is beneficial as a quick evaluation of how much the Debye length should be modified to account for the $(e\phi \ll kT)$ violation when considering Coulomb spacecraft applications.

4.2.2.2 Illustration of Results

To illustrate the results of the parametric relationship of Equation (4.11), a surface plot is shown in Figure 4.3. This plot displays the alpha parameter data as a colored surface, with the fit model shown as a mesh surface. In this figure, it can be seen that the model closely matches the behavior of the data.

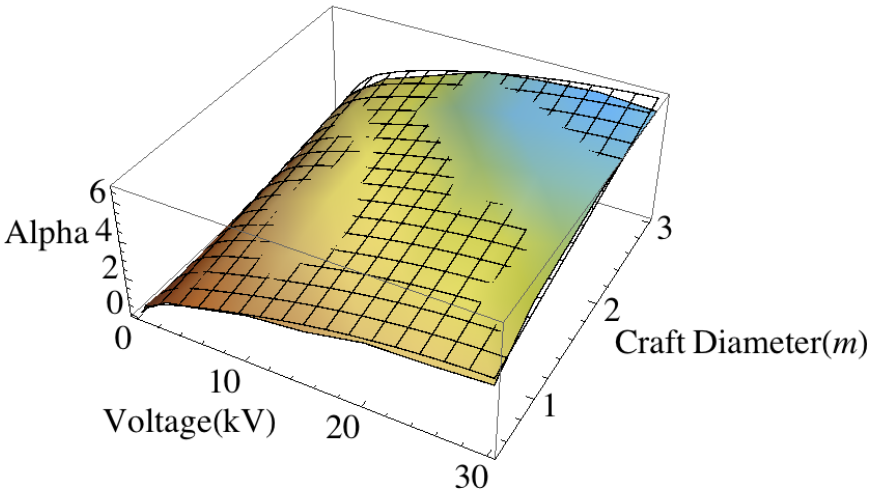

Figure 4.3: Alpha parameter values and surface plot of regression (Equation (4.11)) for Quiet GEO plasma conditions, $\lambda_D = 4$; colored surface represents data and mesh represents fit surface

4.2.3 LEO Effective Debye Lengths

In the same procedure as described for determining the GEO effective Debye length, effective Debye lengths at LEO are investigated. As seen in Table 4.1, the nominal LEO Debye length is on the order of one centimeter. This small distance limits the feasibility of electrostatic actuation for Coulomb formation flying or tethered Coulomb applications. Other applications of electrostatics in LEO may however be feasible, for example electrostatically inflated membrane structures. These structures use electrostatic forces between layers of conducting membranes as the source of inflation pressure. The distances over which the electrostatic force acts is much smaller, likely on the order of a few centimeters. As shown in Table 4.3, $eV = kT$ at a craft voltage of 0.2V, therefore any

Coulomb application with kilovolts of potentials will clearly violate the Debye-Hückel assumption. It is important to understand if the violation of $eV \ll kT$ will aid in electrostatic inflation or other small separation distance Coulomb applications.

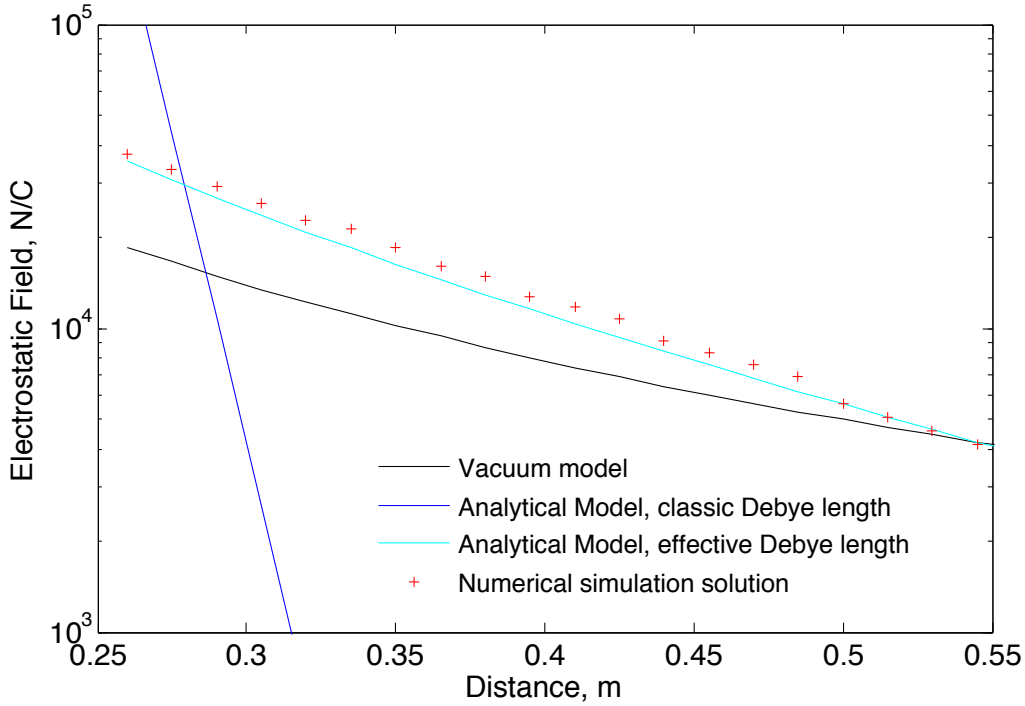

Figure 4.4: Comparison of classic E-field models with the effective Debye model; LEO plasma, $\lambda_D = 0.011m$, $V_C = 5kV$

Figure 4.4 illustrates the E-field models compared to numerical field results for a LEO plasma environment. The classic Debye length E-field model is not a good approximation of the numeric solution. As an improvement to the classic Debye length results, an effective Debye length analytical model was fit to the data for distances up to approximately two effective Debye lengths (α=24 for illustrated case). The scaling factors at LEO proved to be significantly larger than those at GEO, representing significantly less plasma partial shielding of the Coulomb forces. The LEO effective Debye lengths are on the order of several decimeters to a meter, as opposed to the centimeter level classic Debye lengths. This shielding reduction improves the Coulomb forces magnitudes and makes them viable for applications such as inflation of membranes at cm level separations.

The approach presented for modeling the effective Debye lengths provided good results at voltages in the range of 5kV to 30kV, the voltage range which would be employed for Coulomb applications. At lower voltages, the Debye-Hückel model could not be reasonably fit to the numerical solutions solely by using an effective Debye length. Other models would need to be considered for modeling voltages below 5 kV. The α values found in the 5kV to 30kV range are shown in Figure 4.5 for a range of crafti sizes and craft voltages. Interestingly, the α-parameter is nearly constant across the voltage levels, which was not the trend for the GEO case. This indicates that the effective Debye lengths converge to a limit as $eV < kT$ is strongly exceeded. As seen in the plot, the relationship across craft diameters is nearly linear. A linear model is fit to this data with an $\mathcal{R}^2$ value of 0.994. The expression for this linear model for calculating the α-parameter in this voltage range is:

$$\alpha = 7.028 - 0.031V_C + 42.314D_C \tag{4.12}$$

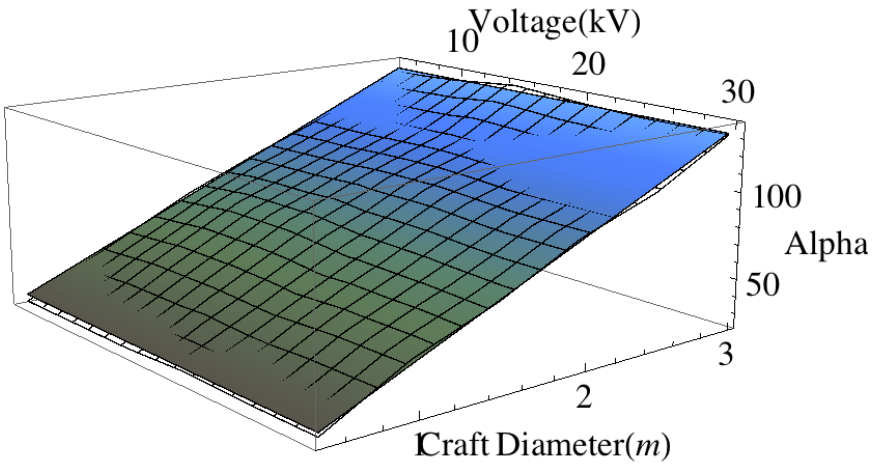

Figure 4.5: Alpha parameter values and surface plot of regression (Equation (4.12)) for LEO plasma conditions, $\lambda_D = 0.011$; colored surface represents data and mesh represents fit surface

At LEO altitudes, the dense plasma can have interactions with the charged body that affect the potential. It is important to note that other plasma mechanisms, such as wake effects, are not being considered in this analysis.

In summary, classical Debye length models are quickly violated for charged craft in LEO and

also in quiet GEO conditions. Numerical simulations allows for a more accurate solution to the forces and a modified 'effective' Debye length can be defined to allow quick use of the analytical equations by direct substitution into the Debye-Hückel Coulomb force model. These effective Debye lengths are calculated for GEO and show that the effective Debye length can be from several times larger than the calculated Debye length for the applications of Coulomb formation flying. In LEO plasma conditions, the 'effective' Debye length can be more than an order of magnitude larger than the classically predicted Debye length. The LEO effective Debye lengths can therefore be up to the meter level, and the resulting Coulomb force improvement from reduced shielding may allow for LEO Coulomb spacecraft applications such as inflation of membranes at cm level separations.

4.3 Charge Flux Interactions with EIMS

In this section we consider the scenario in which either EIMS is flowing through a plasma (in LEO, spacecraft velocities exceed ion velocities) or a plasma flowing around an EIMS. It is of interest for general applications of EIMS to understand the behavior of the particle flows and the response of structure. It is important to understand both how charged particles contact and deflect around the structure and if the structure remains stable. The charge deflection capability of the charged membranes leads to the interesting idea of EIMS for active radiation shielding, which is briefly discussed at the end of this section.

4.3.1 Charge Flux Experiments

For application of the EIMS concept, it is important to understand how the a charge flux from the local space environment interacts with a charged membrane structure. In particular, does the structure remain inflated and stable in the presence of a charge flux? Experiments with an electron emission source and charge detector in a vacuum chamber allow study of the charge flow around an electrostatically inflated membrane structure and the observation of structural stability. Here, the aim of experiments is not to try to simulate realistic space plasma conditions, but to begin to understand charged membrane structure and charged particle interactions. Experiments

were performed to study the charge deflection patterns, the charge shielding capabilities, and the stability of and interaction with the membrane structure.

4.3.1.1 Charge Flux Experiment Hardware Setup

The setup for the charge flux experiments includes an electron gun at one end of a vacuum chamber and a Faraday cup positioned behind a membrane structure at the opposite end of the chamber. The electron gun emits electrons and the Faraday cup measures the current, allowing observation of the flow of electrons around an EIMS structure and providing insight into how an EIMS structure can be used for charge shielding. The EIMS structure is charged with a high voltage power supply system external to the vacuum chamber. The concept is illustrated in Figure 4.6.

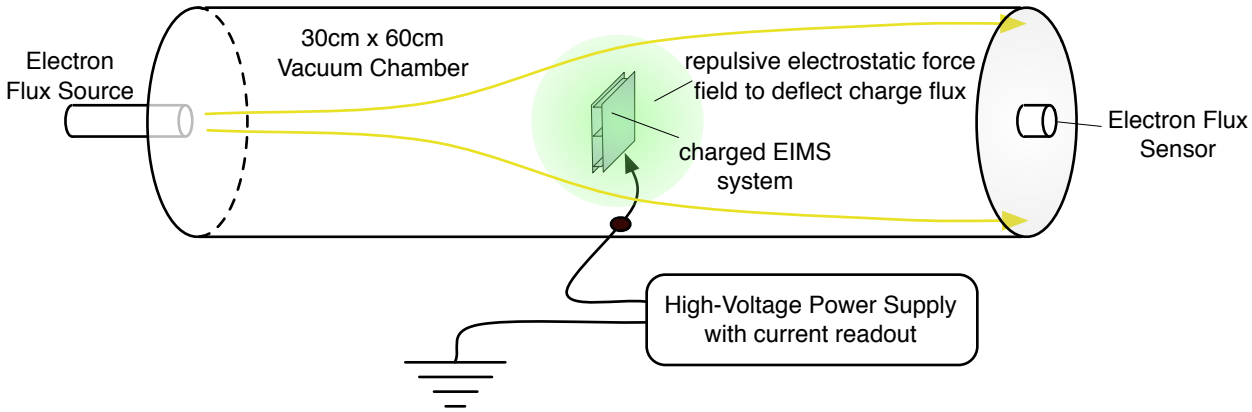

Figure 4.6: Concept illustration for the charge flux experimental setup

Figure 4.7(a) shows the constructed electron emitter. The filament is heated, electrons are thermionically emitted and then accelerated off by the electrostatic field between the biased filament and the grounded wire mesh. The filament is constructed of 5mil coiled Tungsten wire. The length of the Tungsten wire is chosen based on the resistivity of the metal, ρ, and the electrical resistance, R. The resistivity of Tungsten near the melting point is approximately 10^{-6} Ohm-meters and the electrical resistance was measured in the lab to be 2-3 Ohms. Using the below equation, the 5 mil wire (cross sectional area, A=1.3e-8) could have a length, l, of approximately 3.8 cm.

$$l = R\frac{A}{\rho} \tag{4.13}$$

The current emitted from the tungsten coil can be tuned by the AC current level passing through the wire. The higher the AC current supplied to the coil, the higher the temperature, thus more electrons are thermionically emitted and can be accelerated toward the grid. The high voltage power supply providing the DC bias to the coil is current-limited at 5 mA, therefore the maximum emission current is 5 mA.

The FC-70 Faraday cup is a device to detect current within the vacuum chamber. The detector has a small aperture into which electrons can flow to measure the ambient current. The FC-70, shown in Figure 4.7(b) is mounted onto a rotatable vacuum feedthrough probe. The rotatable probe allows the Faraday cup to sweep through an angular range of approximately 120°, thus providing positioning both behind and to each side of the membrane structure. The output of the Faraday cup is connected to a digital multimeter with DC current resolution to picoAmperes. A battery is located in the path between the nano-ammeter and the Faraday cup. The battery is a combination of the two 9 Volt batteries connected in series to bias the Faraday cup by 18 V. This small voltage helps to eliminate low-energy secondary electrons from entering the aperture of the Faraday cup.

For reference, a more detailed diagram of this hardware setup is shown in Figure 4.8.

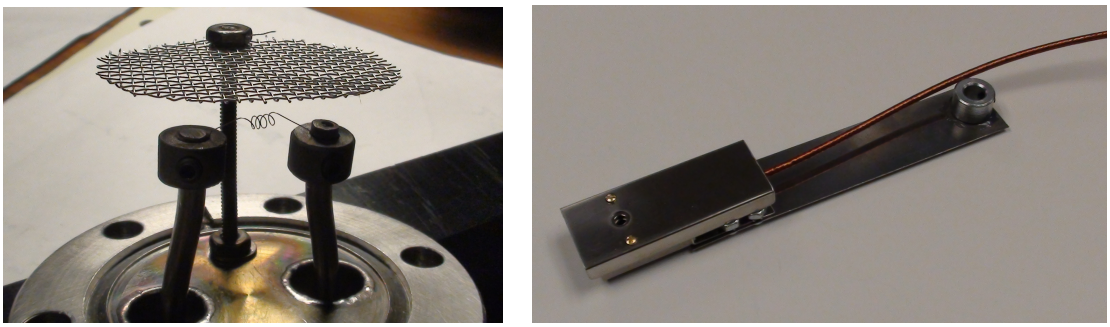

(a) Electron gun filament and grid

(b) Mounted faraday with collar for attachment to vacuum feedthrough

Figure 4.7: Charge deflection experiment hardware

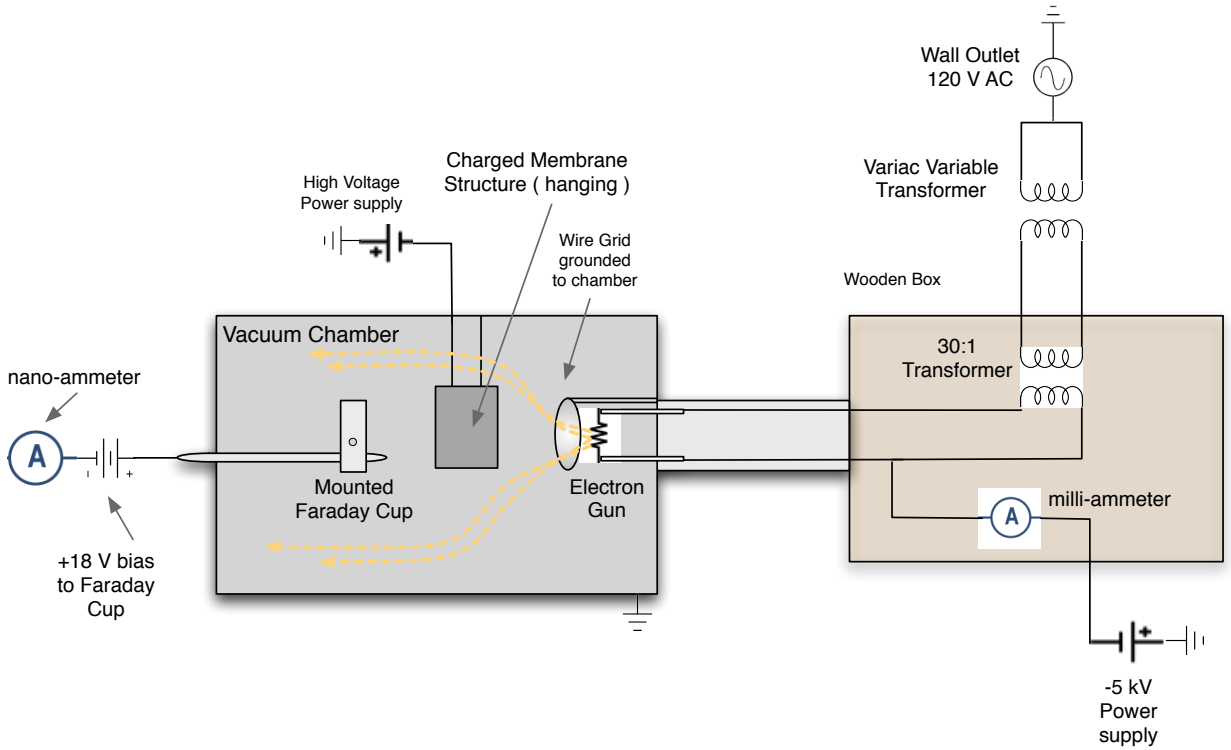

Figure 4.8: Detailed experimental setup for charge flux hardware

4.3.1.2 Electo-mechanical Vibrations

One of the purposes of the vacuum charge flux experiments is to identify any interesting structure/charge interactions. Experiments have shown that the structure is stable, in the sense that it does not collapse or undergo major shape changes, in all of the ranges of particle flows created. Interestingly, structural vibrations were discovered when the structure is charged and the electron gun is emitting a flow of electrons. To observe the vibrations, the membrane structure must be electrostatically inflated while the electron gun is emitting electrons. No vibrations are present with an uncharged membrane structure in the electron flux.

These vibrations are seen at both very low currents and the currents near the maximum of 5mA. The vibrations, however, are not seen through the full sweep of currents. The vibrations, however, are not seen through the full sweep of currents. Rather, at particular charge flux and electrostatically inflationary pressure combinations a resonance-like vibration appears. If the EIMS

voltage is change upwards or downwards, the vibrations can cease until new critical conditions are achieved. Similar patterns are seen for the full range of membrane structure voltages (0 to 10 kV) and electron energies (0 to 5 keV).

Figure 4.9 is shown to convey the magnitude of vibrations in the structure. It is difficult to capture the small oscillations, but a difference can be seen in the membrane shadows of Figure 4.9.

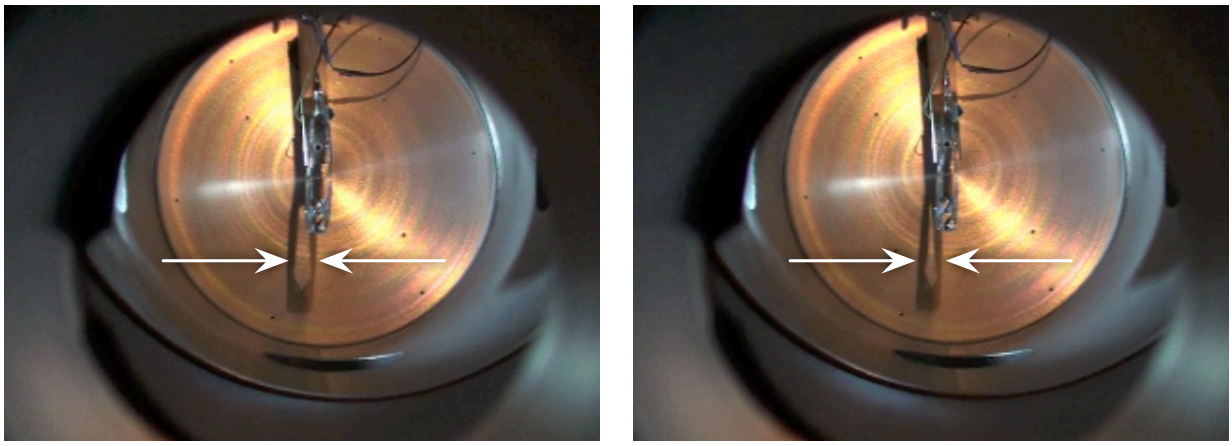

(a) Slightly expanded position during vibration

(b) Slightly deflated position during vibration

Figure 4.9: Video snapshots to illustrate magnitude of structural oscillation; As shown by arrows, difference enhanced in shadow

A Strobotac stroboscope was used to determine the frequency of the structural vibrations. Often, there are several different vibration frequencies present at a given instant. This indicates a complex ripple of vibrations is present as small shape changes occur, not just a single standing vibration. Also, rather than remaining constant, the vibrations appear to have a beat-like frequency, with larger vibrations coming in intermittent pulses. The frequencies measured are around the 4 Hz range with the highest frequency vibrations at the upper limits of the structure voltage (10 kV), electron energy (5 keV) and emitted current (5 mA). Several different shapes of membrane structure, including a pre-tensioned membrane structure (shown in Figure 4.10 were also used to further investigate the vibrations. The stroboscope was used to determine the approximate frequency of vibrations in the pre-tensioned structure and vibrations are found to be near 8 Hz, approximately twice the frequency of the previous unweighted structures. The vibrations are also

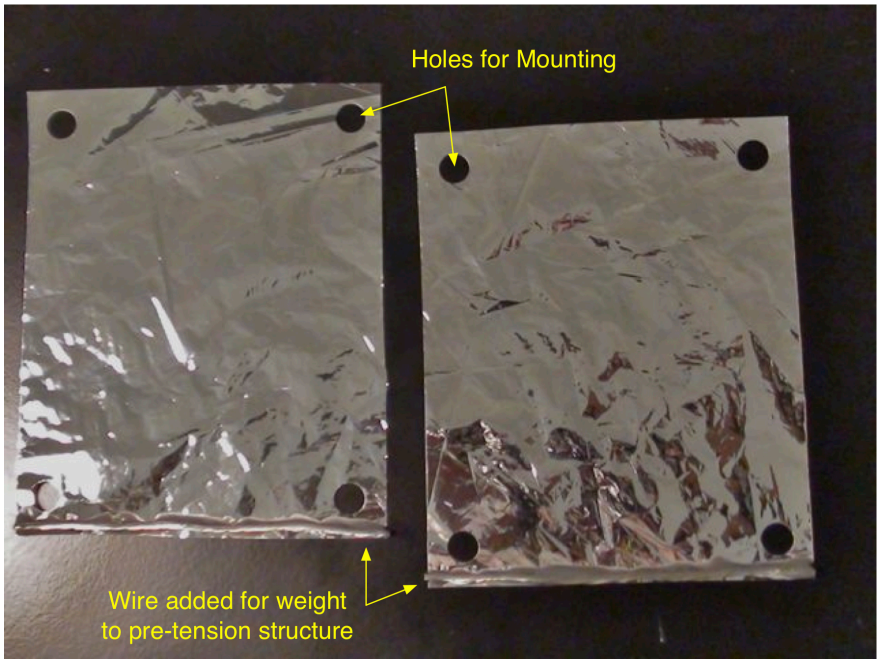

Figure 4.10: Pre-tensioned membrane structure for studying vibrations

more consistent through the entire membrane.

Several speculated sources of the vibrations have been investigated and eliminated. First, it is possible that the deflected charge flux imparts a sufficiently large momentum exchange with EIMS to cause this rippling. To investigate this possible cause, experiments with a single membrane sheet were performed. None of the single-sheet experiments, charged or not charged, showed any visible vibrations, even sweeping through all feasible electron energies and all electron currents. These results suggest that the vibrations are un-likely caused by a transfer of momentum. Otherwise, vibrations or deflections would have been seen with single sheet experiments.

Secondly, the electron flux itself could be a source of these vibrations if the electron gun emitted flux is not steady, but has frequencies near 4Hz. To investigate this possible vibration cause, the electron flow output signal from the emitting gun is studied with an oscilloscope. The Fourier transform function of the oscilloscope is used to determine frequencies present in the driving current signal. The only significant frequencies present were the power line frequency of 60 Hz and

a very high frequency in the kiloHertz range. Neither of these frequencies are in the 4Hz range of the observed structure vibrations.

Thirdly, fluctuations in the EIMS external power supply performance could cause EIMS vibrations. In essence, if the actual EIMS voltage is not held steady, but cycles in the presence of the external charge flux, then these voltage variations would directly results in the electrostatic inflation pressure varying. As a result, the EIMS structure would slightly deflate and inflate. An oscilloscope is used to examine the output of the power supply which charges the membrane structure. The power supply has an internal feedback loop to ensure a digitally commanded reference voltage level is maintained. The measured output signal provides a measurement of how well this voltage is being held constant. It was speculated that the power supply may be overcompensating as the external charges from the electron gun change the charge on the structure. It was found, however, that the power supply output frequencies, with and without the EIMS vibrations present, showed no significant difference. In fact, the power supply fluctuations were very small, barely observable, and more than an order of magnitude larger than the observed EIMS vibrations. Thus, it is concluded that the power supply did not provide first order contributions to the EIMS vibrations. Otherwise, output power variations during EIMS vibrations would leave a unique fingerprint.

The elimination of several possible sources of the vibrations has lead us to believe that the vibrations are due to a coupling between the changing electrostatic fields surrounding the structure and the flow of electrons to and around the structure. The hypothesis is that the membrane surface vibration is a result of local surface charge density variations causes by the charge flux. As the charge density varies, then the local electrostatic inflation also changes. Since the EIMS system is in an equilibrium between the 1-g gravitational forces attempting to compress the structure, and the electrostatic pressure inflating the structure, a small change in electrostatic pressure will negate this equilibrium and result in a local shape deformation, outward or inward. This shape change, in return, will cause a change in the surface normal electrostatic field which impact the near-surface charge flux.

Analytically or numerically describing this phenomena was beyond the scope of these studies.

It remains as future research to understand this complex charge flux and membrane structural fluttering phenomena. Further, note that this hypothesis requires the structure shape to be in an equilibrium between competing electrostatic pressure and compressing gravity forces. This raises the question if such EIMS vibrations would manifest if the structure were in space. If the electrostatic pressures are sufficiently large, here the shape inflation is not limited by gravity, but by internal support structure and membrane surface tension. Thus, a loss in pressure will not result in a shape change until the pressure is less than an externally compressing perturbation. In the absence of gravity, a gravity-like perturbation must still be considered if the structure is accelerated through an orbital maneuver.

In summary, an interesting phenomena of structural vibrations was discovered between a charged membrane structure and a charged particle flow. A series of diagnostic tests were performed to eliminate sources of the vibrations, leading to a conclusion that the vibrations are caused by a coupling between the changing electrostatic fields surrounding the structure and the flow of electrons to and around the structure.

4.3.2 Charge Deflection with Electrostatic Structures

A charged object in the path of a charged particle will change the particles trajectory, depending on the magnitudes of the particle and charged object. This principle suggests an interesting application of an EIMS system to deflect charged particles in space, for example as a radiation shielding device to help enable human space travel. The electrostatically inflated membrane structure is envisioned as a lightweight structure which can act as shield to charged particles. Of interest here are how the shape and dynamic response of EIMS affects the pattern of charge deflection for a flux of electrons.

Radiation shielding is an important problem in space exploration activities. The dangers of radiation must be understood and protection incorporated into any space travel, especially that of long duration and travel beyond Low Earth Orbit. Radiation shielding can be accomplished with passive or active methods, or a combination of the two. One drawback of passive shielding

is the mass of thick materials required for adequate radiation safety. Use of electrostatic fields, illustrated in Figure 4.11, is one active method which provides an alternative to bulk material passive shielding.[64]

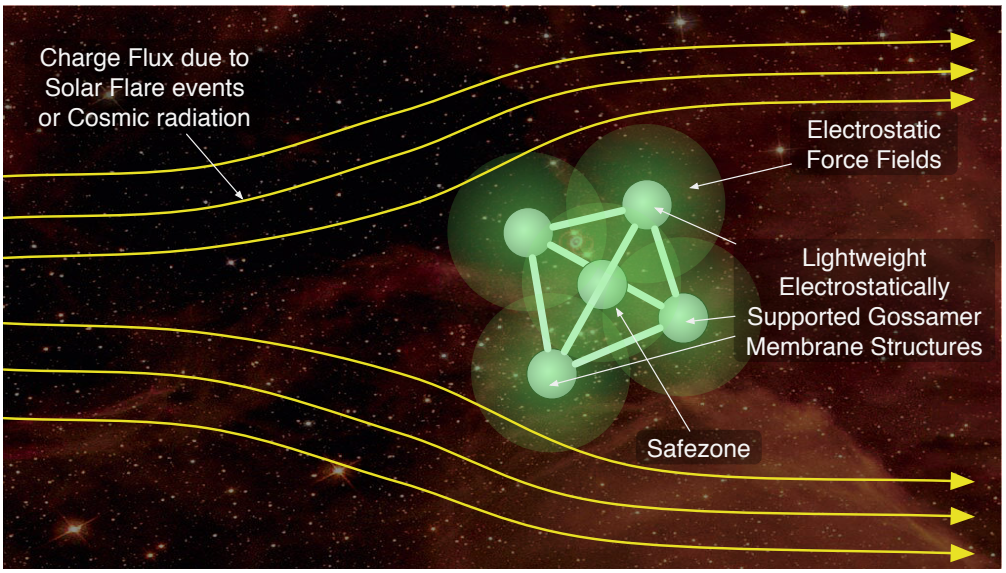

Figure 4.11: Concept illustration of radiation shielding with an electrostatically charged structure

Other forms of active shielding include plasma shields, confined magnetic fields, and unconfined magnetic fields.[65] Some of the challenges of active electrostatic shielding, such as high potentials and size limitations due to electrical breakdown, have deterred further research on the subject.[10] In Reference 10, Tripathi challenges the claim that electrostatic shielding may be unsuitable and explores a design for radiation shielding. The charged 10-sphere design may require potentials of up to 300 Megavolts, and would be used in conjunction with passive material shielding. The ability to achieve 300 MV potential level, however, especially for a space-based system, is not currently within the realm of technology. In this research, only potentials in the tens of kilovolts have been explored, therefore investigating the feasibility of EIMS potentials beyond tens of kilovolts remains as future work.

4.3.2.1 Low Energy Charge Deflection

Experiments with a charged structure in the electron stream were performed to understand the charge flow patterns around the electrostatically inflated membranes and also to study the radiation shielding capability of low energy electrons. The capability to study high potentials and high energy particle flows through experiments is very limited. The experimental setup used for the charge interaction experiments, however can provide a basic picture of how EIMS can be used for particle shielding. The setup in the vacuum chamber is shown in Figure 4.12.

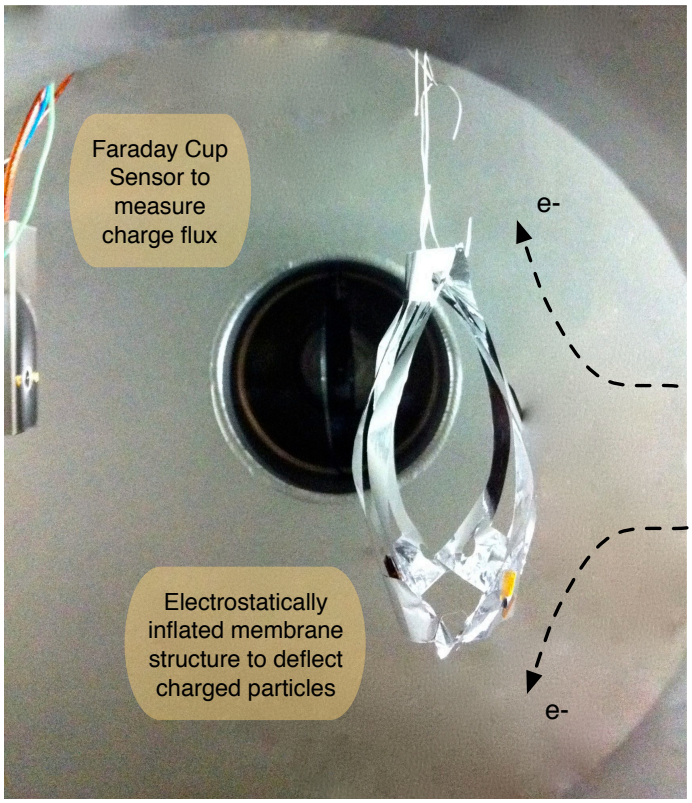

Figure 4.12: Charge deflection using EIMS in the vacuum chamber

To study the charge deflection and shielding pattern around the structure, the Faraday cup position is rotated within the chamber. The probe on which the detector is mounted allows for rotation through approximately 120 degrees. Measurements of detected current are recorded as the probe and detector are swept through the physically feasible angular range. The rotation of the

detector is illustrated in Figure 4.13.

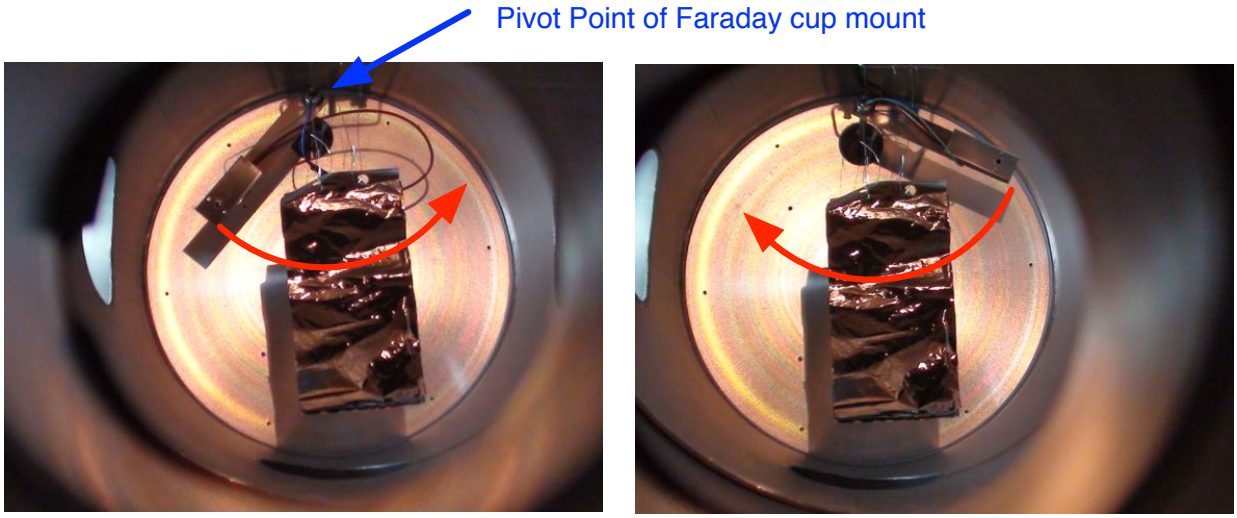

Figure 4.13: Rotation of the Faraday cup around the membrane structure

Experiments were performed with a membrane structure in the vacuum chamber as shown in Figure 4.6. 3D surface plots are used here to represent the data. First, the charge flow pattern without any structure present is compared to that with a uncharged structure. It must be noted here that the electron gun had to be removed from the chamber and loose wiring fixed which affected the flow pattern. When removing the device, the grid which accelerates the electrons had rotated from the correct position down 180 degrees. This had to be rotated into the correct position to remove the electron gun. For this reason, the charge flow patterns appear to be flipped in the following plots of no structure (Figure 4.14) and an uncharged structure (Figure 4.15). What is important to see in these figures is the large drop in electrons directly behind the structure (approximately -20 to +15 degrees) from the 70 nA range down to the 25 nA range.

Next, the same data collection was performed with a charged structure at 4kV and 8kV. These two voltages were chosen such that one voltage was below the energy of the electron gun (5 keV) and one above. The surface plots are shown in Figures 4.16 and 4.17 (note the change in scale).

When the structure is at 4kV and below the electron energy, there is still current in the 20 nA

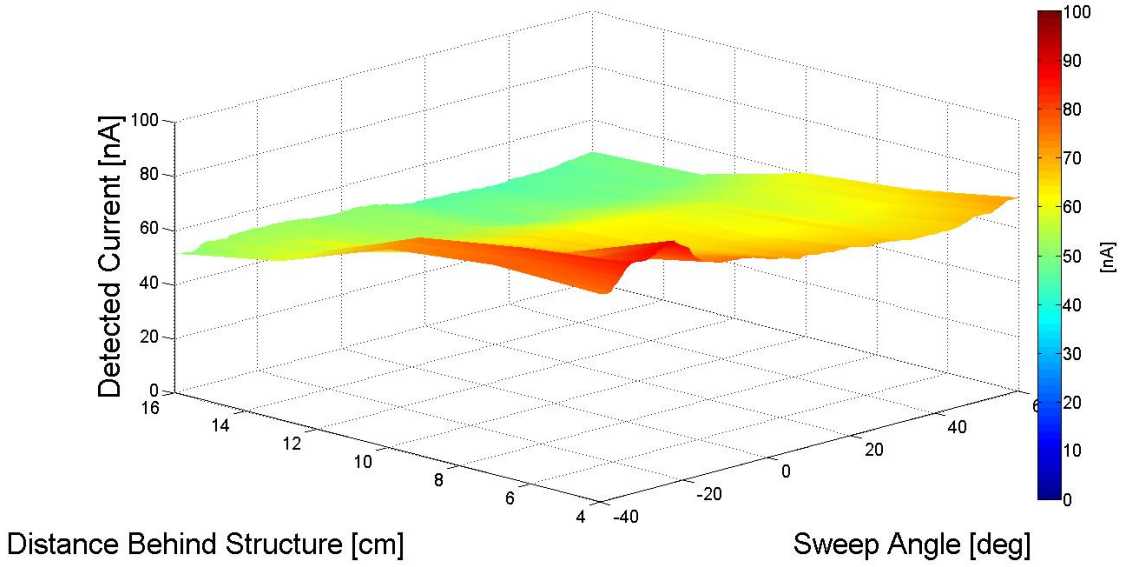

Figure 4.14: Detected current, no structure

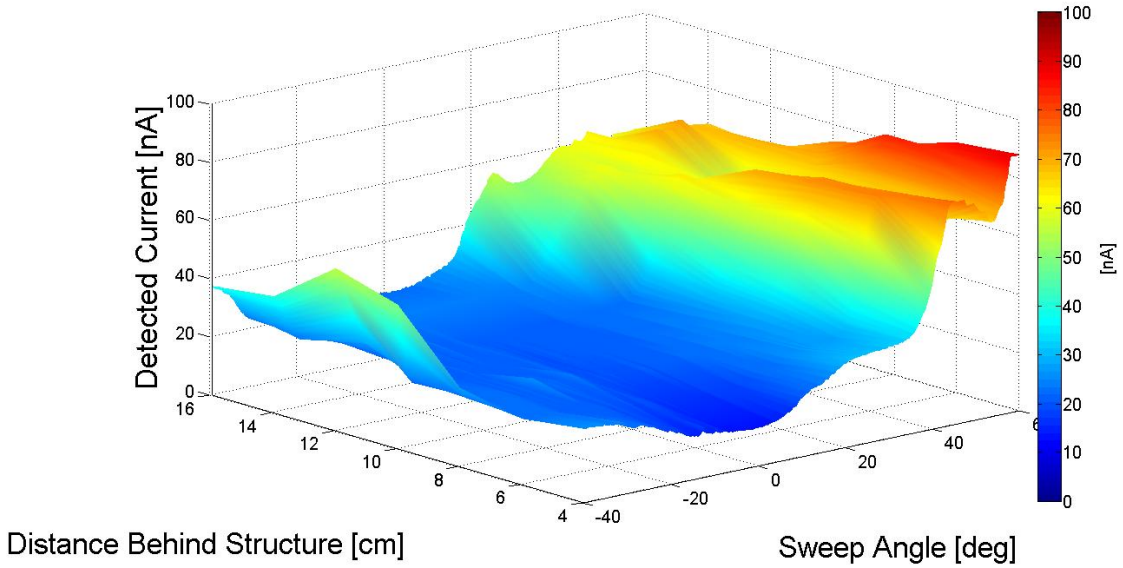

Figure 4.15: Detected current, structure at 0kV

range behind the structure. There is an overall drop, however, in the amount of current detected anywhere behind or to the side of the structure. When the structure is charged to 8kV, there is another large drop in the current levels detected. All recorded currents are below 12 nA and are in the single digit nA range behind the structure. These plots clearly show the electron shielding

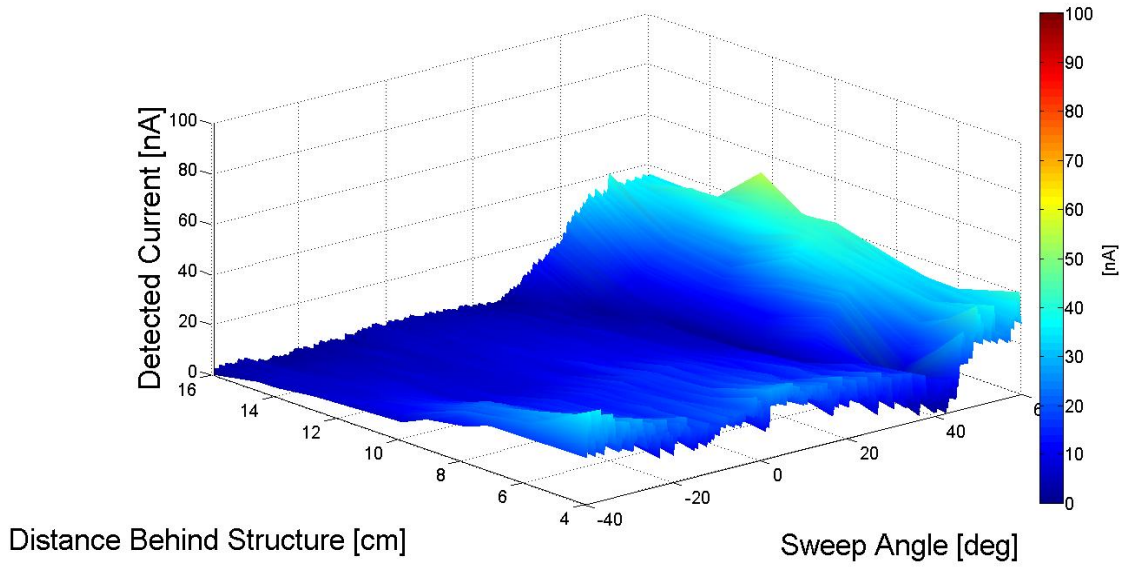

Figure 4.16: Detected current, structure at 4kV

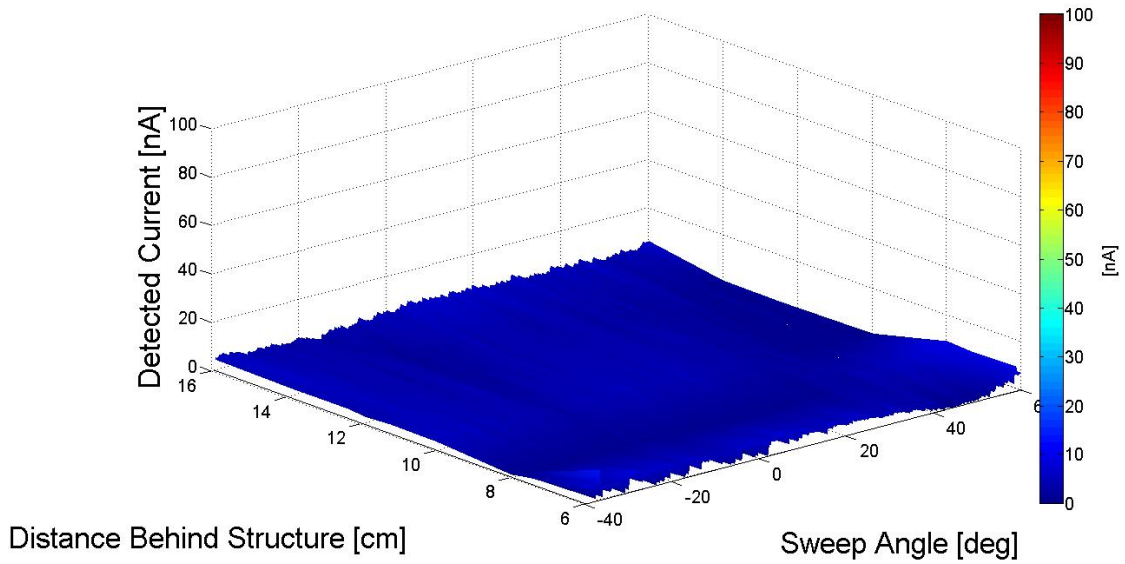

Figure 4.17: Detected current, structure at 8kV

capabilities of a charged membrane structure.

4.3.2.2 Shape and Configuration Study for Charge Deflection

A range of membrane structures were constructed from Aluminzed Mylar for the charge shielding experiments. Four different configurations were used for the shape-study experiments, including sheets with cutouts, and different orientations of membranes connected with membrane ribs or ties. The cutout structures were included to study how the electrostatic fields not including the materials itself can shield particles. The cutout structure could also offer further mass savings. Illustrations of each configuration are shown in Figure 4.18

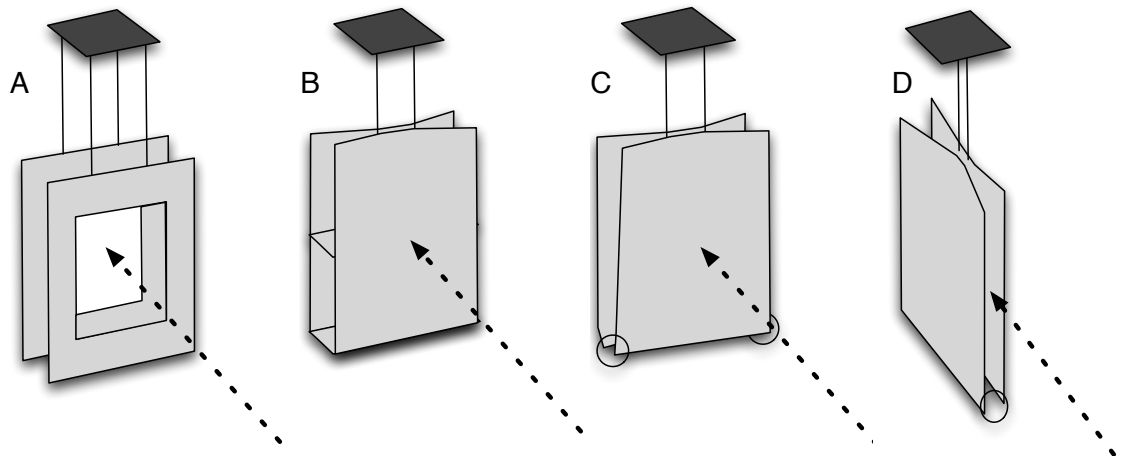

Figure 4.18: Four membrane structure configurations A–D used for experiments. The incoming charge flux direction direction is shown through the dashed arrow.

The first shielding experiments were performed with the unconnected cutout sheets hanging in the vacuum chamber. For a fixed electron energy and emission current, a sweep of voltages on the membrane structure was performed, up the 5 kV high voltage rating on the vacuum feedthrough. For each structure voltage, the current detected by the Faraday cup was recorded. This procedure was repeated for different electron energies, from 1 to 5 keV. There was a clear trend of decreasing current detected behind the membrane structure as the structure voltage was increased. This can be seen in Figure 4.19(a) for the cutout membranes (configuration A), in Figure 4.19(b) for the ribbed structure (configuration B), and in Figures 4.19(c) and 4.19(d) for the two configurations C and D of the tied structure. In these plots, the percentage of current detected relative to the

current detected with an uncharged membrane is expressed by contours.

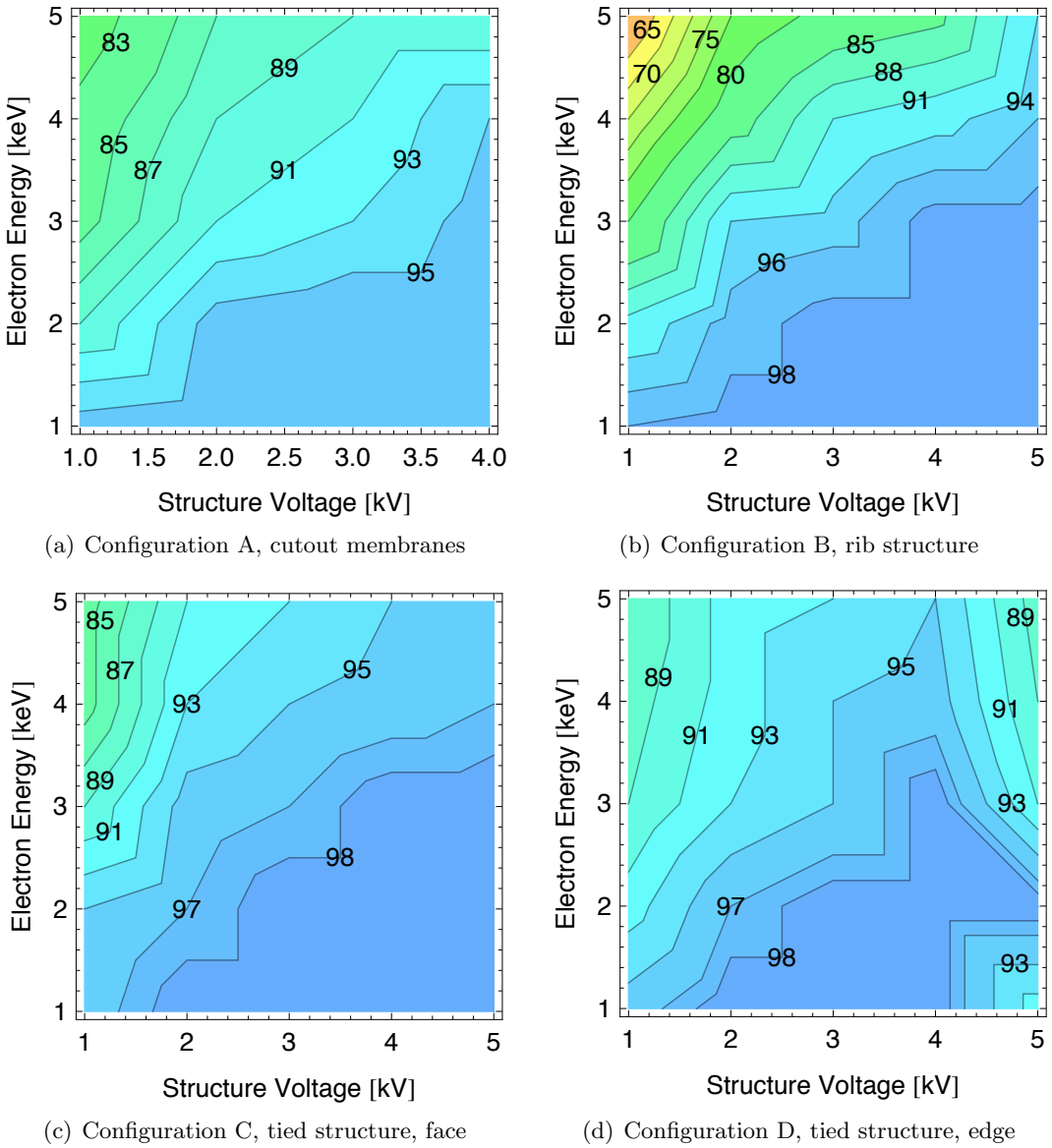

(a) Configuration A, cutout membranes

(b) Configuration B, rib structure

(c) Configuration C, tied structure, face

(d) Configuration D, tied structure, edge

Figure 4.19: Percentage of original detected current behind inflated membrane structure at different electron energies

From these figures, several conclusions can be made. A clear trend exists of increased shielding with increased structure voltage for the first three configurations, where the pattern is seen for all electron energies and structure configurations. These figures appear to have roughly the same pattern. For the ideal case of having an electron of energy less 1keV approach the center of a

charged membrane of potential 1kV, the electron should be deflected backwards. Thus, in this ideal scenario we should not be measuring charge behind the structure if the EIMS voltage is above the electron energy voltage. However, these tests of similarly sized EIMS prototypes illustrate that this is only approximately the case. The electron beam is not focused, and as a result there is bending of the charge flux about the edges, as well as interactions with the grounded vacuum chamber walls. Differences in the charge deflection amount were observed for different EIMS shapes. For example, the cut-out membrane structure (configuration A) provides only a small loss in charge deflection in contrast to the more solid membrane structures. This indicates that very open charged structures might provide very light-weight charge deflection capabilities.

An interesting deviation from the nominal charge deflection to EIMS voltage relationship is seen in Figure 4.19(d). Here, for the tied configuration with the edge facing the electron gun, the current begins to instead increase at the highest structure voltage. Below a structure voltage of 5 kV, the membranes are physically blocking the Faraday cup aperture. When 5kV is achieved, inflation of the two membranes creates an opening in front of the aperture. As there is theoretically no electrostatic field between two like-charged sheets, electrons pass between the membranes relatively unaffected, and thus the shielding begins to degrade. This illustrates that the complex flexible shape interactions with the resulting electrostatic force field must be carefully considered when designing such active charge deflection systems. In the future, a well-focused electron beam is recommended for further shape investigations.

In summary, the application of EIMS for active radiation shielding is investigated and low-energy electron energy experiments are described. The EIMS structures are shown as efficient in shielding electrons nearly 99 percent of energy levels below or equal to structure charge levels. This low-energy shielding capability is assumed to be similar to the high energy charge shielding that would be required for active radiation shielding purposes. It is acknowledged, however, that current technology limits the possibility of applying potentials in the hundreds of Megavolt range. For the electrostatic active charge shielding, the power capabilities must be addressed before the concept is advanced further.

Chapter 5

Charging an EIMS

To achieve desired charge levels for electrostatic inflation, active charge emission or remote charging are considered. For active charge emission, an electron or ion emitter is used to emit a stream of charged particles to balance the other currents to the spacecraft. For remote charging, a beam of electrons is directed onto EIMS to change to potential. In this chapter, these two methods are explored for charging EIMS in different orbit scenarios.

First, an overview of spacecraft charging (both natural and controlled) is presented. Next, an experiment to determine secondary electron emission (SEE) for EIMS applicable materials is described. SEE is a key component of spacecraft charging and previous research on metal coated polymers is sparse. Using the secondary emission results, remote charging demonstrated in the vacuum chamber is compared to simulation, and good agreement is found. Lastly, the power requirements for the charge emission method are explored for LEO and GEO scenarios.

5.1 Review of Spacecraft Charging Principles

5.1.1 Natural Spacecraft Charging

The ambient space plasma surrounding a spacecraft will cause a craft to obtain a non-zero potential with reference to the plasma. Based on the plasma and sunlight conditions, the craft can naturally become either positive or negative, with natural charging levels recorded up to -19 kV on the ATS-6 spacecraft [66]. The naturally occurring currents to the craft which cause charging include the plasma electron and ion flux, photoemission, secondary electron emission, and backscattered

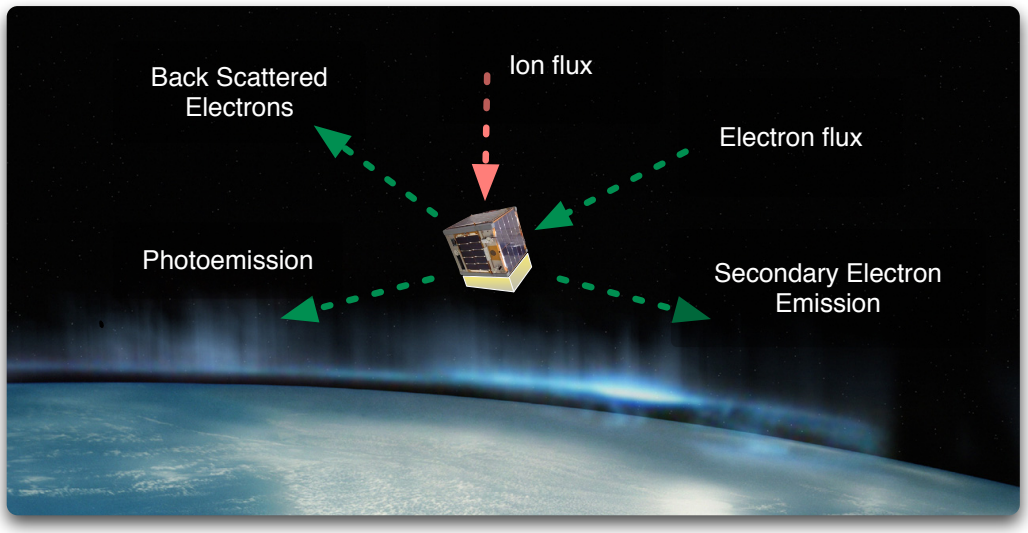

Figure 5.1: Illustration of natural currents in the space environment

electrons as illustrated in Figure 5.1. The natural current balance equation can be expressed as a sum of the following currents:

$$I_e(\phi) - I_i(\phi) - I_{ph}(\phi) - I_s(\phi) - I_b(\phi) = 0 \tag{5.1}$$

where I_e and I_i are the electron current and ion current from the plasma environment, I_b represents backscattered electron current, I_{ph} represents the emitted photoelectrons, and I_s is the secondary electron emission current. The equilibrium of these currents determines the potential which the spacecraft naturally obtains.

The first two terms are the currents from the ambient space plasma environment. Several assumptions will be made for the analysis in this research. First, a single Maxwellian plasma is assumed where the density and temperature of ions and electrons are equal. Also, all ions are assumed to be protons. Models for the electron current are given for positively charged and negatively charged craft respectively in Equations (5.2) and (5.3):

$$I_e(\phi \geq 0) = \frac{-Aqn_e w_e}{4}\left(1 + \frac{\phi}{T_e}\right) \tag{5.2}$$

$$I_e(\phi < 0) = \frac{-Aqn_e w_e}{4} \exp\left(\frac{\phi}{T_e}\right) \tag{5.3}$$

Models for the ion current are given for positively charged and negatively charged craft respectively in Equations (5.4) and (5.5):

$$I_i(\phi > 0) = \frac{Aqn_i w_i}{4} \exp\left(\frac{\phi}{T_i}\right) \tag{5.4}$$

$$I_i(\phi \leq 0) = \frac{Aqn_i w_i}{4} \left(1 + \frac{\phi}{T_i}\right) \tag{5.5}$$

The photoelectron current is defined in Equations (5.6) and (5.7). Here, j_{ph} is the photoelectron flux and $A_\perp$ is the cross-sectional area. The photoelectron flux is variable based on activity of the sun, but a constant value of 20 μA/m is used here.[58]

$$I_{ph}(\phi > 0) = j_{ph} A_\perp \exp\left(\frac{\phi}{T_{ph}}\right) \tag{5.6}$$

$$I_{ph}(\phi > 0) = j_{ph} A_\perp \tag{5.7}$$

There are several empirical models that exist for the secondary electron emission current.[67–69] There is not, however, sufficient previous research to adequately describe the secondary emission with these models for the metal coated polymers used for EIMS. An experiment was thus designed, built, and performed to improve the modeling of this current. The secondary current is described in detail along with the experimental setup and results in Section 5.2.

5.1.2 Charged Particle Emission for Potential Control

Currents can also be actively induced by charged beam emission or charge beam impact. These two methods can be used to actively control the potential of a spacecraft to a desired value. With beam emission, the outgoing charged particles become a part of the current balance given in Equation (5.1) as a positive current for emitting ions and negative current for emitting electrons,

as shown in Equation (5.8). Emitting ions can thus charge the spacecraft negatively while electron emission can induce positive charging.

$$I_e(\phi) - I_i(\phi) - I_{ph}(\phi) \pm I_{beam} = 0 \tag{5.8}$$

Charging through electron or ion beam emission has been demonstrated on many spacecraft missions. One example is the SCATHA spacecraft which used both electron and ion emission to demonstrate charging. An electron beam with a current of 13mA raised the potential of the craft to 4 kV and a 2 keV ion beam raised the potential to 0.3 kV.[70] The charging level is affected by the beam energy and current, the potential difference between the emission and the craft (if near the same energy, there is beam spreading and return current to the craft), and the local space plasma conditions.

The magnitude of the charge emission current is dependent on the sum of the natural currents and the desired charging level. Figure 5.2 illustrates an example of charge emission currents required for achieving a range of potentials for a $1m^2$ craft. In this simulation, the electron, ion and photoelectron current are modeled as described above and the constant photoelectron current dominates the environmental currents. As shown in the figure, the ion emission beam current must match the environmental current such that the total current sum is zero and a fixed potential is maintained.

5.1.3 Indirect Charging with Electron Beam

Another method to achieve and maintain a fixed potential on a spacecraft is through remote charging. Here, an electron beam is used to transfer charge and achieve high potentials. The resulting potential from the beam depends on the current and energy of the electron beam, the secondary electron emission, and the backscattered electrons, as well as other charging phenomena, such as the ambient plasma ions and electrons and photoemission, and how the surface is initially charged.[71] Similar to the natural current balance, the current balance equation for remote charging is shown in Equation (5.9)

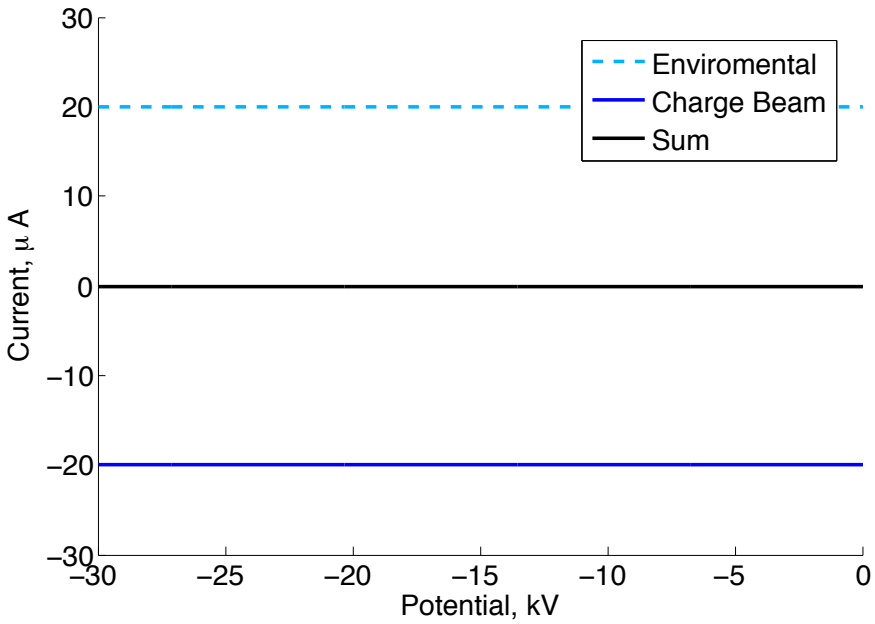

Figure 5.2: Ion emission current to maintain a fixed potential in GEO plasma

$$I_e(\phi) - I_i(\phi) - I_s(\phi) - I_{ph}(\phi) + I_{\text{beam}} = 0 \tag{5.9}$$

In the mission scenario for remote charging, a chief craft would have an electron gun to bombard the EIMS with a current of electrons. The chief craft would also need an auxiliary ion gun to maintain a current sum of zero as to not change the potential level.

To simulate the remote charging scenario, each current to the spacecraft must be defined. Assuming that the backscattered electron current is small, models for electron and ion current from the atmosphere, photoelectron current are as described in the first section of this chapter. For this simulation, it is assumed that the craft is in sunlit conditions. This scenario requires a higher input from the electron beam, thus is the worse case scenario. As stated previously, there are several models for describing the secondary electron emission current. For these simulations, the Draine and Salpeter model is used, as shown in Equations (5.10). This equation uses the parameters of maximum secondary electron yield and energy at maximum yield as the characteristics of materials

(here, aluminum), as will be described in detail in the following section.

$$I_{\text{SEE}}(\phi) = 4\delta_{\max} I_{\text{beam}}(\phi) \frac{E_{\text{eff}}/E_{\max}}{(1 + E_{\text{eff}}/E_{\max})^2} \tag{5.10}$$

The current from the electron beam is dependent on the width and accuracy of the beam. A coefficient of transfer efficiency, α, is used to incorporate these effects. The beam current is therefore given in Equation (5.11) for when the potential of the craft is less than the potential of the gun:

$$I_{\text{beam}} = \alpha I_{\text{beam},0} \tag{5.11}$$

As the secondary emission current is a function of the beam current, determining the required charging beam input to maintain a fixed potential requires re-arranging the current equation to solve for I_{beam}:

$$I_{\text{beam}} = \frac{I_{\text{env}}}{1 - 4\delta_{\max} \frac{E_{\text{eff}}/E_{\max}}{(1+E_{\text{eff}}/E_{\max})^2}} \tag{5.12}$$

where I_{env} is the sum of the environmental currents (ion, electron, and photoelectron).

A simulation is shown in Figure 5.3 to illustrate currents for the remote charging scenario. Here, a 20 kV electron beam is used to maintain a sweep of fixed potentials in a GEO plasma. It can be seen that as the craft potential nears the electron gun energy, the secondary emission becomes larger. The craft potential is limited by this gun energy, thus 20 kV would be the maximum achievable potential.

5.2 Secondary Electron Emission for EIMS Materials

As seen in the previous section, the secondary electron emission is a large factor in the remote charging scenario for a spacecraft. It is thus important to understand the secondary electron yield to determine how the spacecraft becomes charged and what beam currents are required.

Previous research has explored secondary electron emission for many materials. Experiments have been designed to measure secondary electron emission and equations have been empirically

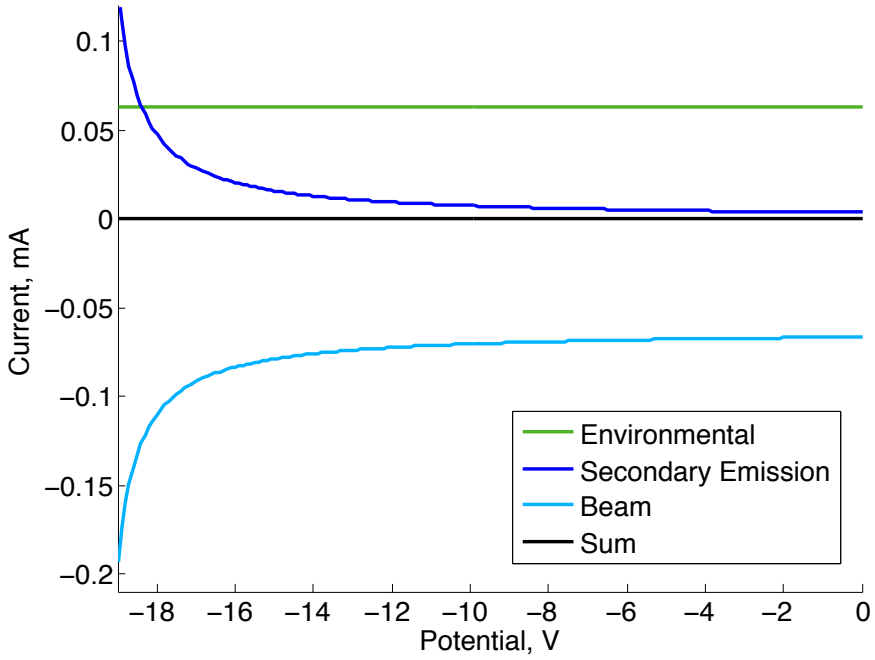

Figure 5.3: Remote electron beam current to maintain a fixed potential in GEO plasma

determined to model secondary yields. There haven't, however, been experiments to quantify secondary yields from metal-coated membrane materials, such as Aluminized Mylar. In this research, an experiment is designed and executed to experimentally determine the secondary yields for several EIMS-applicable materials. Fully understanding the secondary yield characteristics is critical part to a full understanding of charging behavior.

The research performed is also applicable to other spacecraft mission scenarios, for example the electrostatic re-orbiter concept. In this concept, an electrostatically charged space tug uses Coulomb forces to manipulate the orbit of a space debris object [72]. The space debris object will be naturally charged from the space environment, but the charge level can be augmented by remote charge transfer via a stream of charged particles. This research on remote charging may contribute to understanding how charging is more effectively performed for electrostatic re-orbiting based on the secondary electron contribution to charging.

In the following sections, the principles of secondary emission are presented. Next, the de-

signed experimental hardware and procedures to measure secondary electron emission are described. Experiments first performed use a well characterized material (Nickel) in order to better understand measurements and quantify any discrepancies from theory (for example due to ionization or measuring other secondary electrons). Then results are presented for membrane materials of Aluminized Mylar and Aluminized Kapton and the application to an EIMS system is discussed.

5.2.1 Principles of Secondary Electron Emission

Secondary emission occurs when an incoming electron shares energy with nearby electrons in a material and the energy is enough for the electron to leave the surface. The energy of the secondary electrons is usually only a few eV [71]. The secondary electron yield coefficient, δ, is defined as the ratio of outgoing electrons (from secondary emission) to the current of incoming electrons. The outgoing electrons are referred to as I_{SEE}, describing the secondary electrons emitted from a material sample being bombarded by incoming electrons. I_{beam} is the incoming current from the electron source. The secondary electron yield is therefore defined as:

$$\delta = \frac{I_{\text{SEE}}}{I_{\text{beam}}} \tag{5.13}$$

An empirical model for the secondary yield, δ is described by Sternglass [67] by Equation 5.14. The equation is based on fits to empirical data for many materials.

$$\delta(E_0) = 7.4\delta_{\max}\frac{E_0}{E_{0,\max}}e^{-2\sqrt{\frac{E_0}{E_{0,\max}}}} \tag{5.14}$$

Here, E_0 is the energy of the incoming electron beam. The maximum value for secondary yield is described with $\delta_{\max}$ and the energy at which this maximum occurs is $E_{0,\max}$. These maxima depend on the material being bombarded by electrons. The secondary yield is therefore a function of only beam energy, material, and potential of the emitting surface. The Sternglass curve is illustrated generally in Figure 5.4. What is interesting to note here is that there are two unity crossings. Between energies E_1 and E_2, the number of electrons leaving the material due to secondary emission is higher than the number of incoming electrons. Although intuitively a surface

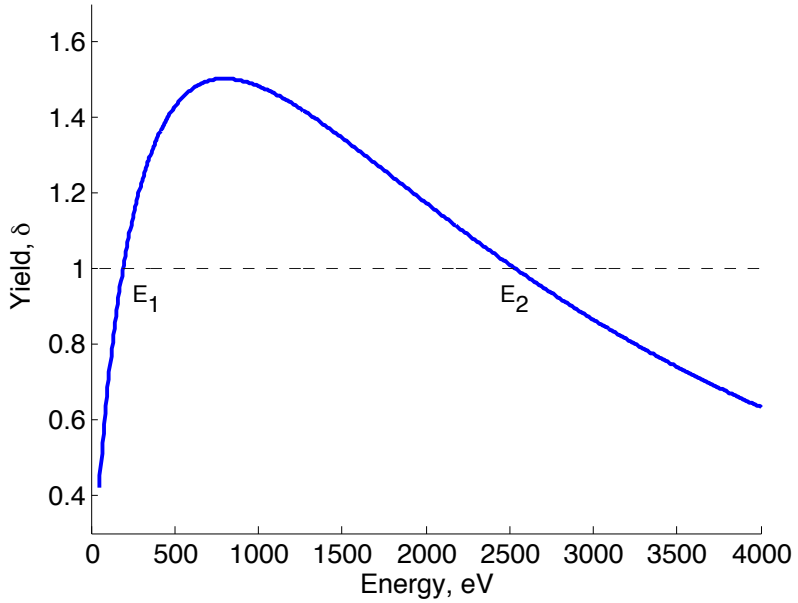

Figure 5.4: Illustration of secondary electron emission yield curve

would charge negatively through electron impact, if the beam energy lies between energies E_1 and E_2, the surface would charge positively due to the greater number of electron leaving than arriving.

To illustrate the effect of materials on secondary electron emission and spacecraft charging, Figure 5.5 is shown. In this figure, various currents are represented. First, the environmental currents are plotted for a nominal geosynchronous orbit (GEO). It is assumed that the spacecraft is in sunlight, thus the currents included here are the photoelectron current, plasma electron current, and the ram ion current. Next the current from a remote charging electron beam is included, assuming an energy of 20 keV. Included next are the secondary electron emission from two different materials: Aluminum and Kapton. The two materials have different yield properties, thus the resulting currents can vary significantly. Lastly, the sum of all currents to the spacecraft are illustrated for the two different materials cases. As can be seen in the Figure, the equilibrium where the currents sum to zero occur several thousand volts apart. Th difference demonstrates how important it is to correctly quantify the secondary electron emission to understand how a spacecraft will charge when using remote charging.

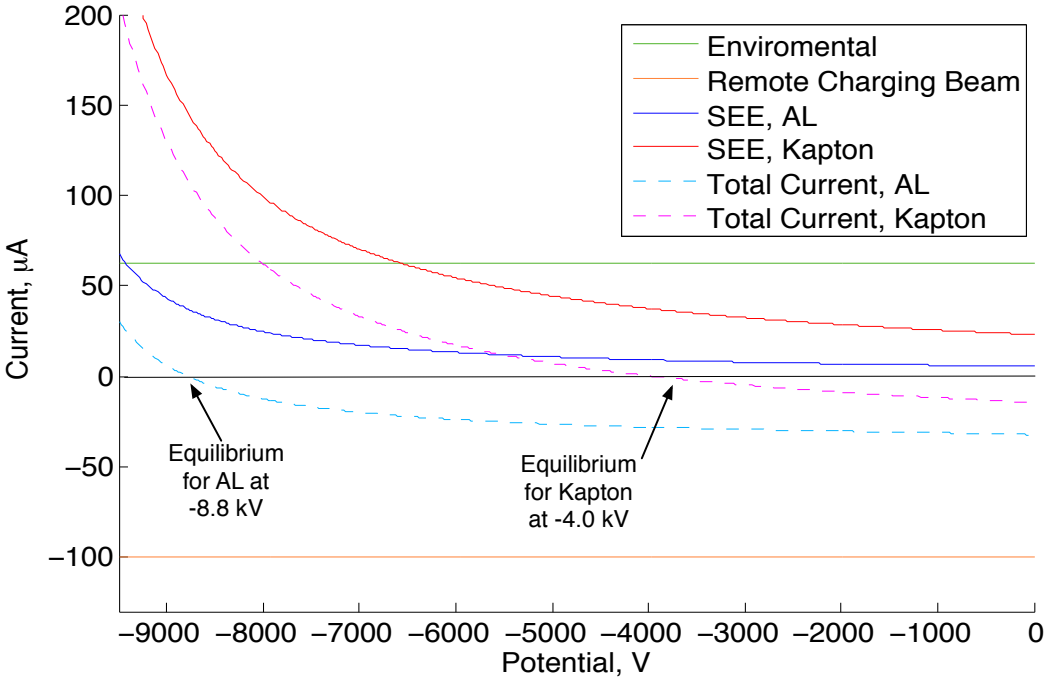

Figure 5.5: Illustration of effect of secondary electron emission on spacecraft charging

The parameters of $\delta_{\max}$ and $E_{0,\max}$ to determine the secondary electron yield can be determined through experiment or simulation[73]. Some examples of the yield parameters for various materials are shown in Table 5.1. It can be seen that there is a significant difference in the yield parameters of metals and polymers. In general, insulators have higher secondary electron yields than conductive materials[74].

Table 5.1: Secondary emission yield parameters for selected materials

	$E_{0,\max}(eV)$	$\delta_{\max}$
Aluminum[68]	300	0.95
Nickel[68]	500	1.3
Copper[68]	600	1.3
Kapton[75]	150	2.1
Mylar[75]	175	4.8

5.2.2 Experiment Description

The purpose of the experiment is to investigate the secondary electron emission from samples of aluminized Mylar and aluminized Kapton to better understand the remote charging response of these EIMS-applicable materials. Initially, a baseline experiment with a Nickel material sample is performed to compare the experimental results of secondary emission to the accepted values for Nickel. Then, EIMS-applicable materials are studied to determine secondary yield characteristics. The yields of these materials have not previously been experimentally determined.

5.2.2.1 Hardware Description

The hardware setup for the remote charging experiments includes an electron gun emitting charge toward a material sample in a vacuum chamber. The chamber has vacuum capability down to approximately 10^{-7} Torr. Each of the hardware components of the setup are described below.

An electron gun is used to emit electrons which are accelerated toward the membrane sample. A filament is heated and electrons which are thermionically emitted are accelerated off by the electrostatic field between the filament and a grounded wire mesh.The electron gun filament is constructed of 5mil coiled Tungsten wire. The electron gun can operate with energies up to 5 keV and emit current up to 5 mA.

The mounting system for the material sample is illustrated in the diagram shown in Figure 5.6. The sample and grids are mounted inside a 2 inch diameter copper tube which is grounded via connection to the vacuum chamber walls. The material sample is mounted on an 1.25 inch aluminum plate, shown in Figure 5.8(b). Ceramic mounts and other insulating materials (Teflon, Kapton) are used to keep the sample mount and grids electrically isolated from the grounded metal cup. Each grid and the sample mount have individual electrical connections through an electrical feedthrough in the chamber to allow individual biasing. The setup as viewed from outside the vacuum chamber is shown in Figure 5.7.

The material sample is connected to a Kiethley Model 6487 PicoAmmeter/Voltage Source

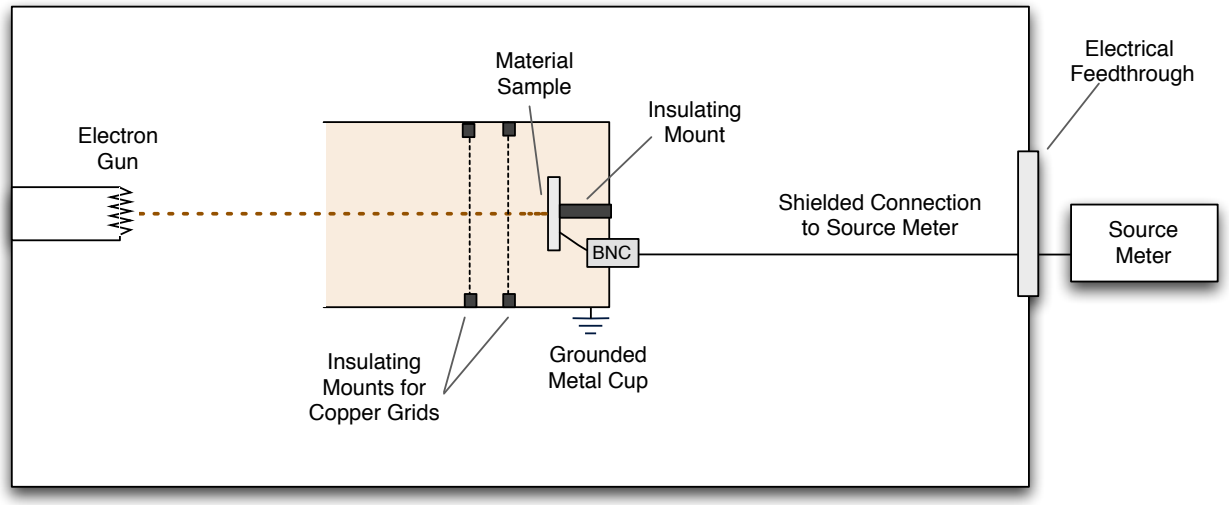

Figure 5.6: Experimental setup for measuring secondary electron emission

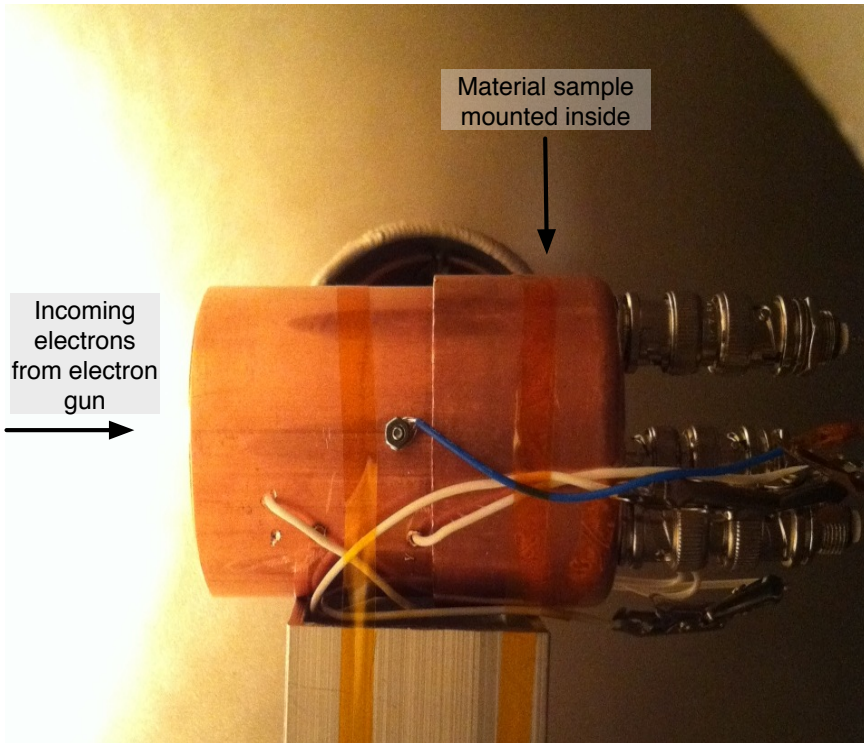

Figure 5.7: Experimental setup for measuring secondary electron emission

(source-meter). This model has ±500V DC voltage source and current measurement capabilities. The source-meter is used to simultaneously run through a pre-defined voltage sweep while measuring

(a) Aluminum grid inside test apparatus (view in primary electron velocity direction)

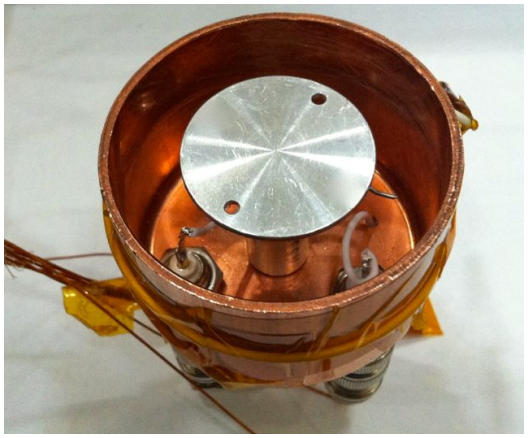

(b) Aluminum mount for affixing material samples inside test apparatus (behind grid shown in A)

Figure 5.8: Sample mount apparatus

current. This sweep is used for the characterization of the I-V curve in order to determine the current from the material sample and the beam current, as will be further explained in the following section.

5.2.2.2 Experimental Procedure

To calculate secondary electron yield, equation (5.13) is employed. It is necessary to experimentally determine both the beam current and the sample current for this equation. Each of these quantities can be found for a particular electron energy by sweeping a voltage on the material sample and simultaneously measuring the currents using the source-meter. The voltage sweep is chosen to range from -75 V to 75 V to capture the full behavior of I-V curve. Figure 5.9 shows the measurement from a voltage sweep.

The current on the material sample being measured by the SourceMeter is a combination of several currents: primary electrons from the electron gun, secondary electrons emitted from the material sample, secondary electrons emitted from the grids, and ions from the ionization of the residual gas. First, the main source of current is the primary electrons from the electron gun. The

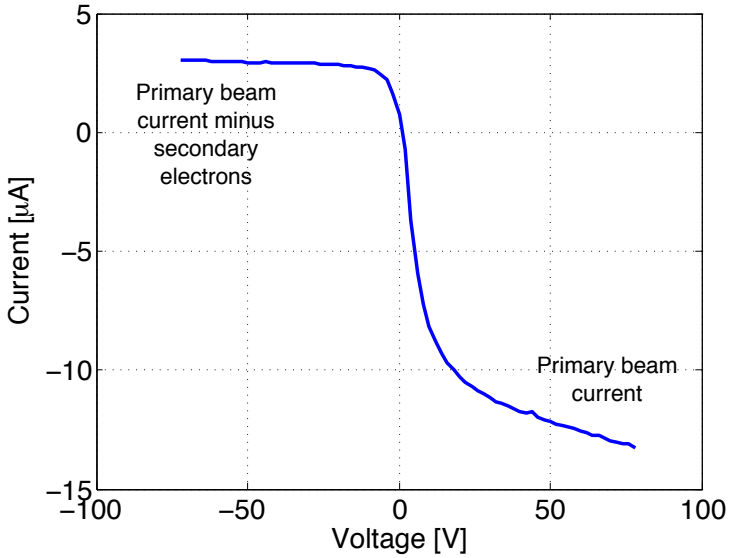

Figure 5.9: Current vs. voltage data sample

current emitted from the gun for the experiments is 3 mA. The electron gun provides a spray of electron from a heated filament with minimal directionality, therefore only a fraction of the 3 mA reaches the material sample. The beam current which reaches the sample can be approximated from the positive potential data of the I-V curve shown in Figure 5.9. When the sample is biased positively to a level greater than the energy of the secondary electrons (which are only a few eV), all secondary electrons are attracted back to the sample. The current of leaving secondaries is cancelled out by the secondaries returning. The primary beam is unaffected here, as the energy of the beam is a minimum of 150 eV (thus always larger than the potential used for biasing). The positive end of the I-V curve therefore gives us the value of I_{beam} for Equation (5.13) and is expressed as:

$$I_{+\phi} = I_{\text{beam}} \tag{5.15}$$

Notice, however, that the current level does not settle as potentials continue to increase. Here, other stray electrons begin to be attracted into the test setup and onto the material sample. The value for I_{beam} is chosen as the inflection point in the I-V curve. This was determined through calibration with Nickel, as it described in the results section.

At the opposite end of the I-V curve where the bias potential on the sample is negative, the currents being measured are the beam current minus the secondary electrons leaving the material sample. Because the sample is biased negatively, all the lower energy secondary electrons which are emitted from the material are accelerated away due to electrostatic repulsion. As the beam current is already determined as described above, the secondary electron current can be calculated from the measurement. Recall from Equation (5.13) that the current of the secondary electrons can be rewritten as:

$$I_{SEE} = \delta I_{\text{beam}} \tag{5.16}$$

Therefore the measured current at negative potentials, named $I_{-\phi}$, can be defined as:

$$I_{-\phi} = I_{\text{beam}} - I_{SEE} = I_{\text{beam}}(1 - \delta) \tag{5.17}$$

By calculating the ratio ($\mathcal{R}$) of the current at the two ends of the I-V curve:

$$\mathcal{R} = \frac{I_{-\phi}}{I_{+\phi}} = \frac{I_{\text{beam}}(1 - \delta)}{I_{\text{beam}}} = 1 - \delta \tag{5.18}$$

we can solve for the secondary yield:

$$\delta = 1 - \mathcal{R} \tag{5.19}$$

Thus, the secondary electron emission yield at a particular primary electron energy can be calculated directly from the measurement of the I-V curve. This calculation determines one point on the yield curve for the material under study.

To determine the secondary electron yield curve for a material (as shown in Figure 5.4), the following experimental procedures are performed at a range of primary electron energies. The yield curve is constructed point by point, calculating the yield at many primary electron energies. The range capability for electron energies to be explored is from 100 eV up to 5 keV with the hardware setup described above.

5.2.3 Secondary Emission Results

In this section, the preliminary experimental results for baseline materials and membrane materials are presented and discussed.

5.2.3.1 Baseline SEE Measurement

In order to verify the experimental setup and procedures, a sample of nickel was chosen as the first material to study. Through previous experiments, nickel has known secondary electron emission characteristics [68]. Nickel also makes a good material for this procedure due to the slow oxidation rate or corrosion resistance, as oxidation can have a significant effect on secondary emission.

The yield curve created from the experimental data is shown in Figure 5.10.

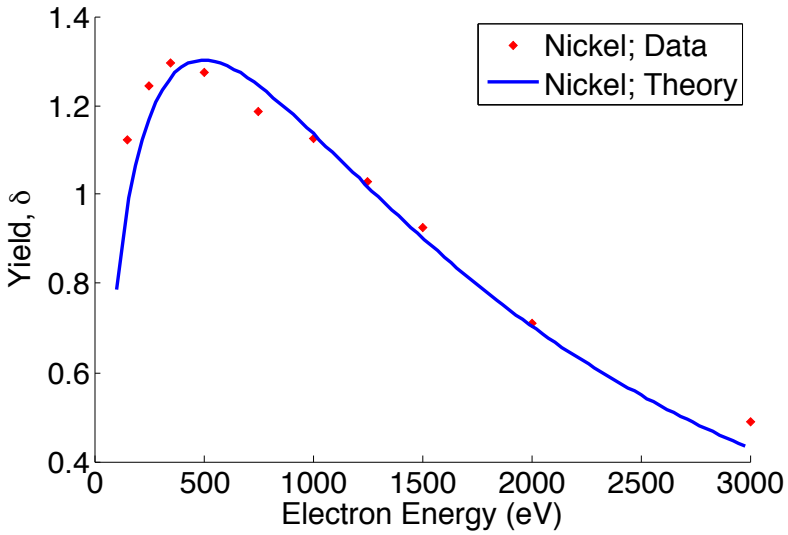

Figure 5.10: Experimental data for nickel yield curve compared to the Sternglass model

It is noted that a membrane sample of Nickel was also studied during the baseline stage of this experiment. The membrane sample, however, had an annealed surface, which has been shown to have a significant effect on the secondary emission yield. [76,77] The Nickel membrane did not follow a trend of the Sternglass yield curve therefore was not used for the baseline study.

5.2.3.2 Membrane Materials

The first membrane material investigated is aluminized Mylar. The sample for the study is 1/4 mil thickness aluminized Mylar. Figure 5.11 shows the yield curve that was built with experimental data. The data is compared to the Sternglass yield curves for both aluminum and

Mylar. At lower energies, the aluminized Mylar data lies between the yield curves of the two pure materials. The trend of the data follows the general shape of Sternglass curve, though does not drop-off as quickly as either the aluminum or Mylar.

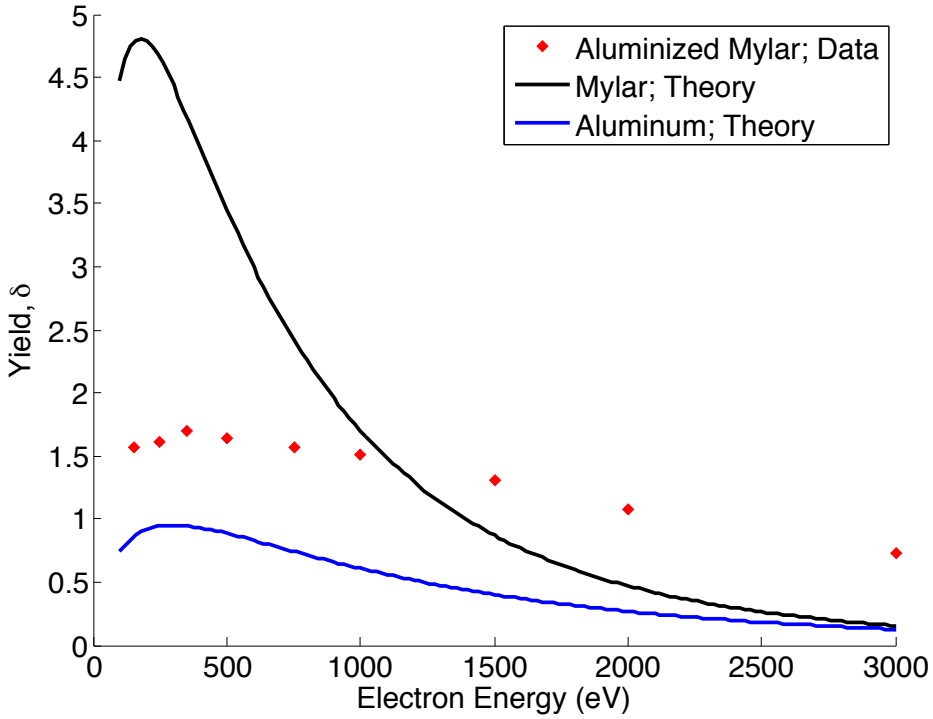

Figure 5.11: Experimental data for Aluminized Mylar compared the Sternglass model for aluminum and Mylar

Aluminized Kapton is the second membrane material studied and the data collected for the yield curve is presented in Figure 5.12. The data again follows the general shape of a Sternglass curve showing a peak at low energies and the yield decreasing as energies become larger, though the drop-off is much more gradual then the component materials.

As oxidation makes an impact on secondary emission, a sample of commercial aluminum foil is also studied. The data for the AL foil is shown in Figure 5.13 and there is a clear difference between the theory and the sample. The aluminum foil data is more similar to the aluminized polymers than to the aluminum theory. This helped to demonstrate the effect that oxidation can have on the material and to explain the behavior of the aluminized polymers. Even at low Earth

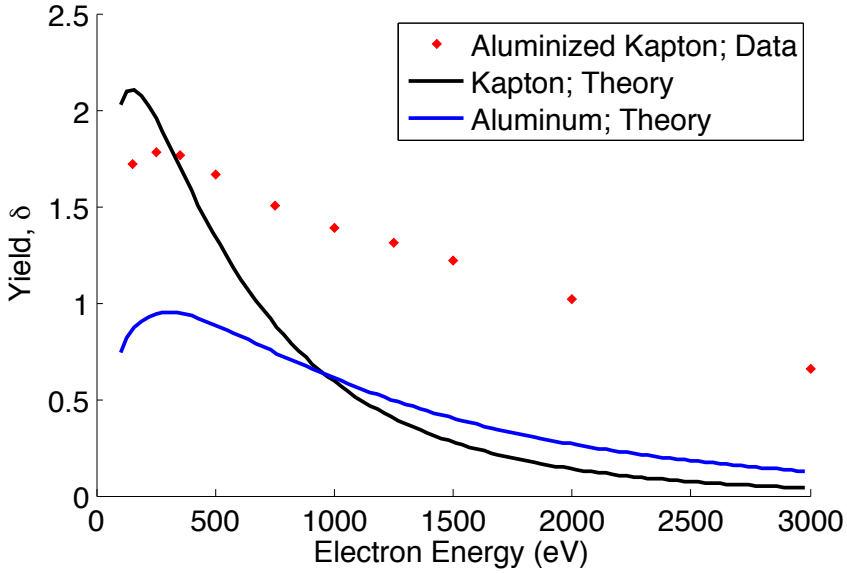

Figure 5.12: Experimental data for Aluminized Kapton compared the Sternglass model for aluminum and Kapton

orbit altitudes oxidation can take place, suggesting that the secondary emission behavior of these EIMS materials could change over the lifetime of the mission.

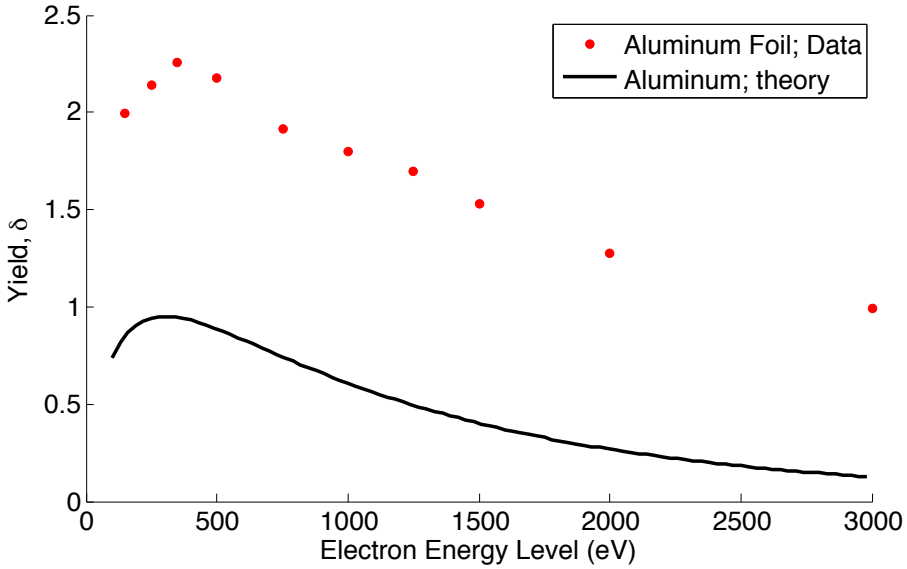

Figure 5.13: Experimental data for aluminum foil compared the Sternglass model for aluminum

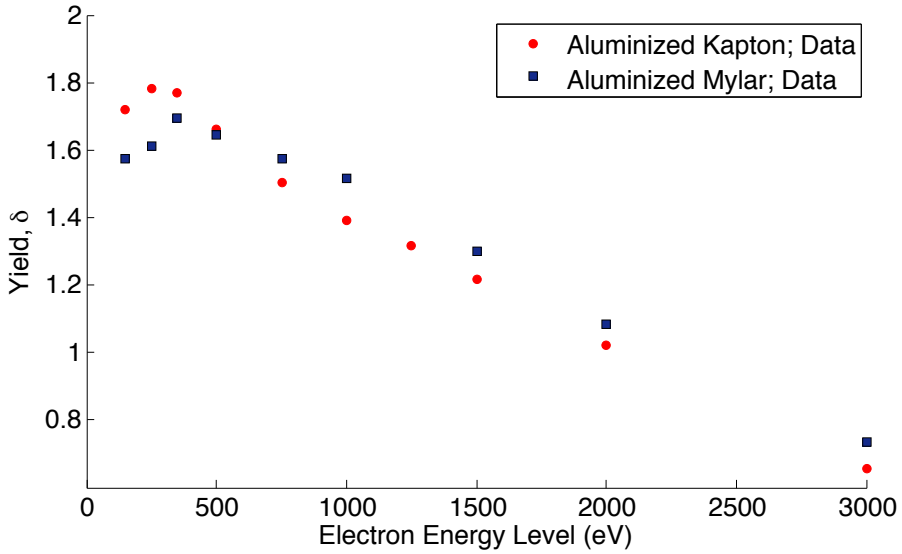

Figure 5.14: Comparison between experimental data for Aluminized Kapton and Aluminized Mylar

The comparison between the two membrane material data sets is presented in Figure 5.12.

The Aluminized Kapton yield curve is similar to that of Aluminized Mylar, suggesting that there may be little difference in remote charging behavior with these two membrane materials. At nearly every energy, the Aluminized Mylar shows a slightly higher yield value. For both of the membrane materials, the yield is above unity until energies are near 3000 eV. This demonstrates that secondary electron emission is a large factor in remote charging unless high beam energies (above 3 keV) are employed.

In order to conveniently utilize the results for the aluminum coated polymers, the data was fit to the parameters of the Sternglass curve using Mathematica's nonlinear model fitting tool. The Sternglass parameters for Aluminized Mylar and Aluminized Kapton are shown in Table 5.2 and the curve fit results are illustrated in Figures 5.15 and 5.16. The curve fit for both membrane materials capture the behavior well over the range of data. The Sternglass curve with the fit parameters, however, would slightly under predict the secondary emission effects at energies above which data was collected.

Table 5.2: Experimental secondary emission yield parameters for EIMS materials

	$E_{0,max}(eV)$	δ_{max}
Aluminized Mylar	511	1.78
Aluminized Kapton	433	1.83

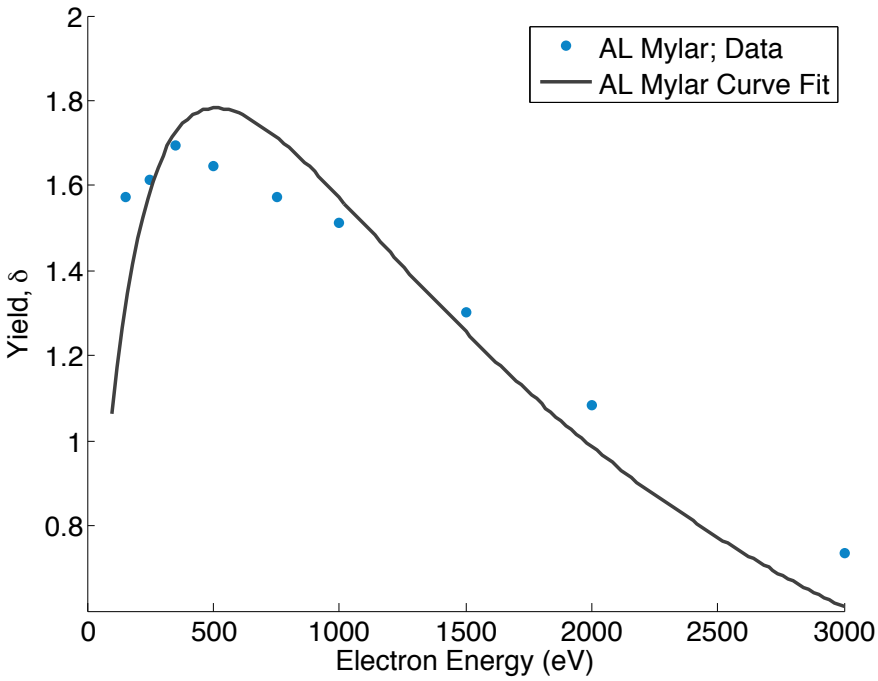

Figure 5.15: Aluminized Mylar data and fit to Sternglass curve

5.2.4 Application to EIMS

The results from this experiment yield important information about using the method of remote charging to raise the potential of a membrane structure for electrostatic inflation. Based on the secondary electron yield of a material, the achievable potential levels can vary by many kiloVolts. Thus, the difference between being able to obtain the desired potential level or not may be in the choice of materials. For example, in Figure 5.5 for the given GEO remote charging scenario, the aluminum object charged to an equilibrium potential of -8.8 kV while the Kapton material charged to -4.0 kV. Here, it may be more desirable to have a conducting material with a

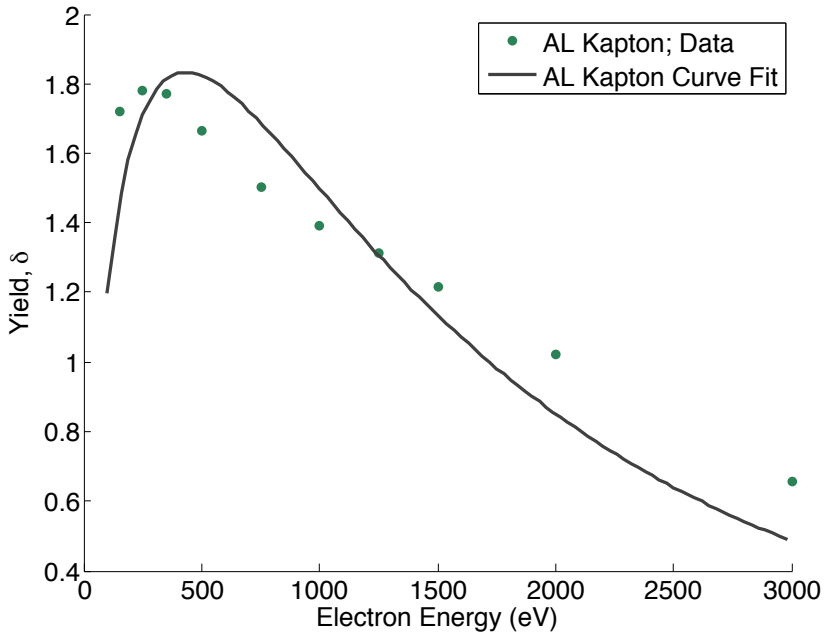

Figure 5.16: Aluminized Kapton data and fit to Sternglass curve

lower secondary electron emission. For a membrane material, this could mean a thicker deposition layer of the aluminum onto the Kapton or Mylar, as a pure aluminum foil at membrane thicknesses does not have sufficient strength. Considering other charging methods, such as charge emission from the spacecraft, other materials may be more efficient for charging to desired high potentials. In the scenario of electron emission to charge positively, the higher the secondary electron emission (from plasma electrons), the easier it would be to charge positively. Even with remote charging using an electron beam, it could be possible to charge to positive potentials. Here, the beam energy would be chosen near the maximum of the yield curve in order to eject as many electrons with each incoming electron. The potential on the craft, however, would then be limited by the low energy of the electron beam.

5.3 Experimental Verification of Remote Charging

To demonstrate the capability for charging a membrane structure remotely, an experiment was arranged in the vacuum chamber. Figure 5.17 shows the simple setup in the chamber: the electron gun emits a spray of electrons and the membrane sheet is hanging in the path of the electrons. It is assumed that the emission of the electron gun is relatively conical, with a distance between the emitter and membrane of H_{cone}.

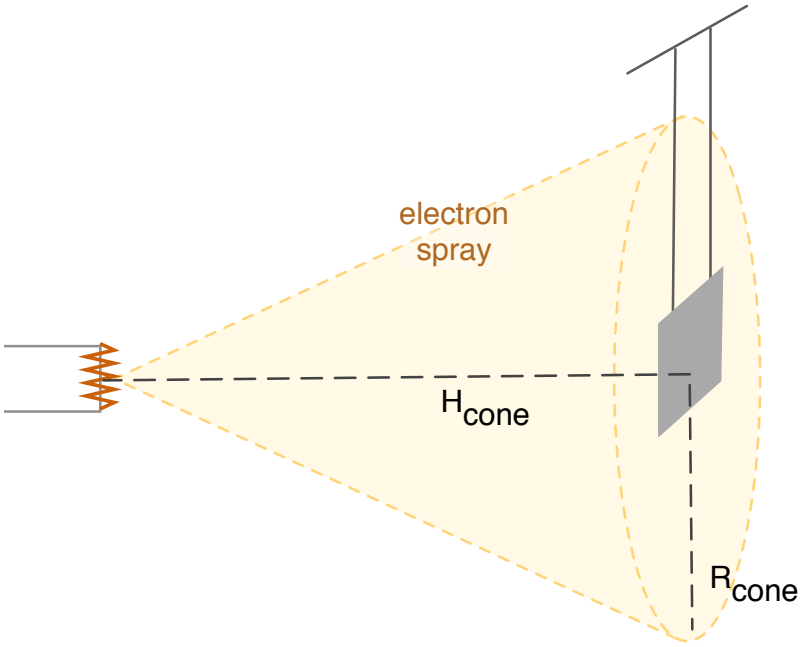

Figure 5.17: Illustration of remote charging experiment and electron spray geometry

There are three currents to and from the membrane: incoming primary electron current, outgoing secondary electron current, and incoming ion current. The ion current is caused when a primary electron impacts a molecule (primarily water vapor or Nitrogen in the vacuum chamber) and ejects an electron, thus creating an ion. The ion may be collected by the membrane if the material is biased to a negative potential, thus attracting the positively charged ions. To calculate the approximate number of ions being created by impact ionization, the following equation is

employed[78]:

$$I_i = I_0 N q_i x \tag{5.20}$$

In Equation (5.20), I_0 represents the electron beam current, N represents the number density of the gas in the chamber, q_i is the ionization cross section, and x is the mean free path length. Cross sections of molecules can be found in the NIST online database for ionization cross section by electron impact (See Reference 79). The cross section is dependent on the incoming electron energy and reaches a maximum near 150 eV. It is assumed that the primary molecule in the chamber is water, thus ionization cross sections for H_2O are used in calculations. Calculations show that for the chamber pressure and electron gun capabilities for this experiment that the ion current is on the order of 50 μA. The electron gun current to the membrane and the secondary current are on this same order of magnitude, therefore the ion current has a significant impact on the remote charging in the vacuum chamber.

As an example, an experiment is performed with the electron gun operating at maximum energy (5 keV) with an emission current of 3 mA. Using a high voltage probe (allows passive measurement of high voltage due to extremely high resistance), the potential of the membrane can be measured from external to the chamber. Charging to approximately -550 V can be observed with this setup. This demonstration proves the concept of remote charging a membrane structure with an electron beam. To understand the level of charging, each of the currents is quantified. Figure 5.18 illustrates the currents to and from the membrane for this experiment.

To calculate the electron beam current which reaches the membrane, the cone angle for the electron spray must be calculated. The first experiment was used to calibrate the angle to make the simulation match the experiment. It was found that the angle is approximately 45 degrees. Using this value, it was found that the simulation still matches the experiment with any electron beam current, suggesting that the calculation is correct. As the energy changes, the angle of the cone varies slightly. This intuitively makes sense, as the higher energy, the less spreading should be seen with the beam, and more of the current reaches the membrane. For a beam energy of 4.5

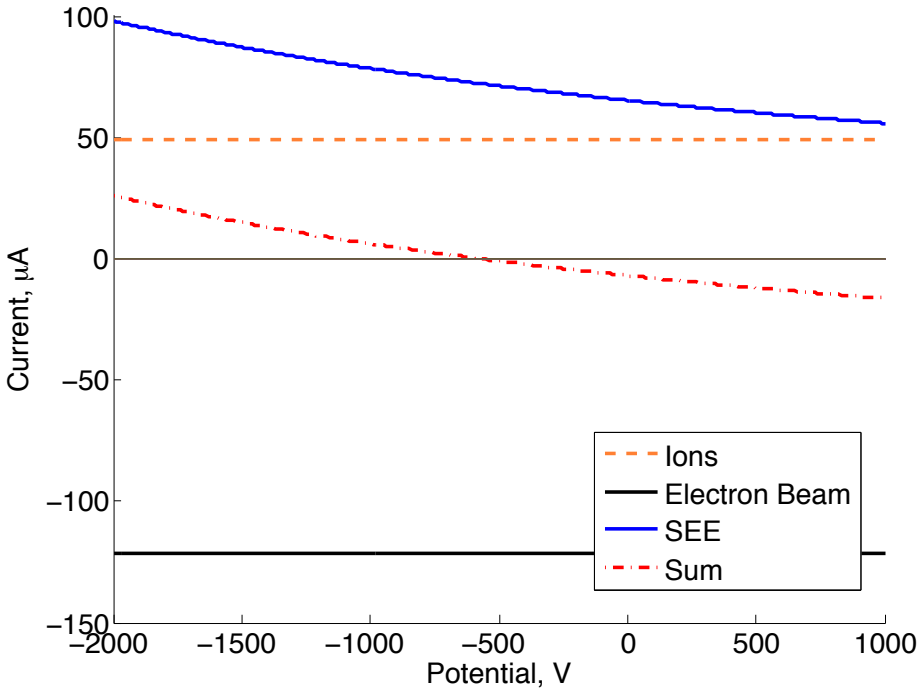

Figure 5.18: Currents in remote charging simulation at 5 keV showing equilibrium potential of approximately -575 V

keV, the angle is closer to 46 degrees.

Below a beam energy of 4.5 keV, remote charging was not observed in the chamber. This can be verified with the simulation of currents in the chamber. Figure 5.19 shows the currents for a beam energy of 4 keV. Here, the equilibrium potential would be a positive number. However, when the membrane reaches a positive potential, the ions are no longer attracted to the membrane and the secondary electrons can be re-collected after being ejected. The potential of the membrane, as measured by the high voltage probe, reaches only a few millivolts.

5.4 EIMS Power Requirements for Fixed Potentials

In this section, the power required to maintain a fixed potential on an EIMS in a plasma environment is described. It is critical to understand the power requirements to assess applicability of an EIMS in various orbit conditions. It is noted that EIMS may also be used in conjunction with

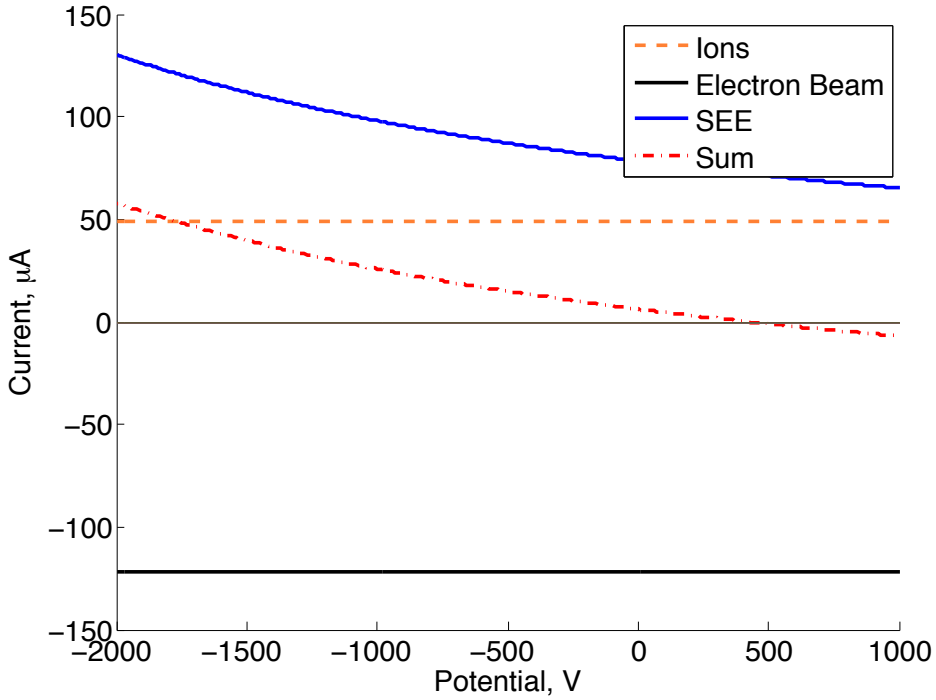

Figure 5.19: Currents in remote charging simulation at 4 keV showing a positive equilibrium potential

membrane stiffening technology. Here, EIMS would only require power for an initial deployment and shape acquisition. Then, material stiffening technology would be used to fix the shape and maintaining the potential would no longer be required. Some examples of stiffening technology include UV-curable laminates, heat-cured thermoset composite laminates, or hydro-gel rigidization[9]. In these simulations, though, it is assumed that power is constantly required to maintain potentials required for maintaining the desired shape of EIMS while on-orbit.

For maintaining a potential through charge emission, the power is simply the product of the current from the charge emission beam and the potential of the EIMS craft:

$$P = I_{\text{emit}}\phi \tag{5.21}$$

where the emission current, I_{emit}, is simply the sum of the environmental currents which will impact

the craft:

$$I_{\text{emit}} = -[I_e(\phi) - I_i(\phi) - I_{ph}(\phi)] \tag{5.22}$$

For the simulations in the following sections, an EIMS with a surface area of 1 m^2 is assumed. Also, it is assumed that EIMS is in sunlit conditions, which can drastically increase the power requirements, especially in GEO where the photoelectron current dominates the environmental currents.

5.4.1 GEO Power Requirements

At GEO altitudes, the plasma environment is relatively benign for Coulomb applications. Table 5.3 shows the nominal plasma conditions that are used for the GEO remote charging and charge emission simulations.

Table 5.3: GEO plasma parameters for charging simulations

Electron temperature, $\mathcal{T}_e$	900 [eV]
Electron Density, n_e	1.25 [cm^{-3}]
Debye length, λ_D	200 [m]

Using these conditions, the currents due to the plasma are calculated and subsequently used in Equation5.22 to determine the required emission current to offset the environmental currents. The required power is calculated with Equation (5.21) and is shown in Figure 5.20. At the negative maxima for EIMS potential, -30 kV, the power required is 0.6 W. This is a very reasonable value for even a smaller spacecraft at GEO. For positive potentials, only approximately 10 mW is required to maintain a +30 kV potential. From the orbit perturbation study in Chapter 3, it was found that 335 V is required to maintain inflation. For -335 V, the power required is 7 mW and for +335 V, only a fraction of a milliwatt. In eclipse, the power requirements are even smaller, as there is no photoelectron current.

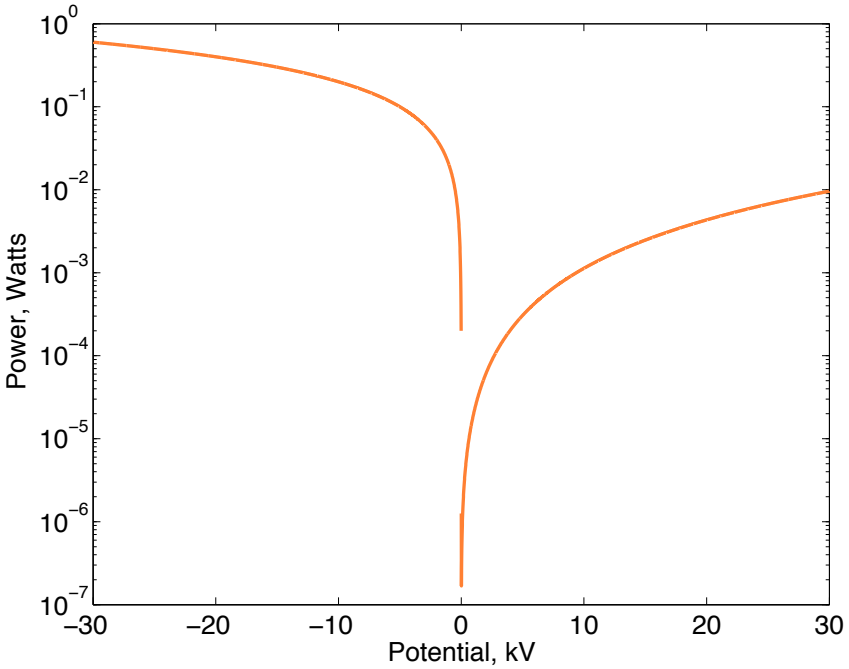

Figure 5.20: GEO Power requirements for maintaining a fixed potential using charge beam emission

5.4.2 LEO Power Requirements

In LEO, the cold, dense plasma has a significant effect on the charging of EIMS. The plasma at these altitude is four orders of magnitude hotter than at GEO. Table 5.4 shows the plasma conditions that are used for the LEO remote charging and charge emission simulations. As the plasma environment is much more aggressive than at GEO, there is a large increase in the power required to maintain a potential. Figure 5.21 shows the power required to maintain a range of craft potentials in LEO. To maintain a negative potential, the power requirements are likely to be in the hundreds of watts up to the kilowatt range. For a positive potential, the power requirements increase by approximately an order of magnitude, up to 10 kilowatts for maintaining a potential of 30 kV. When using charge emission to achieve and maintain a potential in LEO, charging negatively is therefore more advantageous with regard to power requirements. From the orbital perturbation study, voltage requirements were found for two different LEO orbits: 300 and 400 km. At a 300 km orbit, required voltage is 3.2 kV to offset perturbations. This requires 13 W to

Table 5.4: GEO plasma parameters for charging simulations

Electron temperature, $\mathcal{T}_e$	0.2 [eV]
Electron Density, n_e	1×10^5 [cm^{-3}]
Debye length, λ_D	0.01 [m]

charge negative or 570 W to charge positively. To meet the required 2.0 kV for the 400 km orbit, 5 W or 225 W are required for charging negatively or positively, respectively. These requirements may be feasible for smaller craft at LEO altitudes, as small satellites power capabilities range from a Watt up to a few Kilowatts.[80] Charging to the higher voltages considered, though, would be above the capabilities for a small satellite platform, therefore membrane stiffening needs to be further investigated if potentials at this level are required. Also to be considered for high power applications are the thermal effects on the membrane. Rapid charging or high currents could potentially melt the membrane materials, therefore experiments should be performed to maintain safe levels for charging.

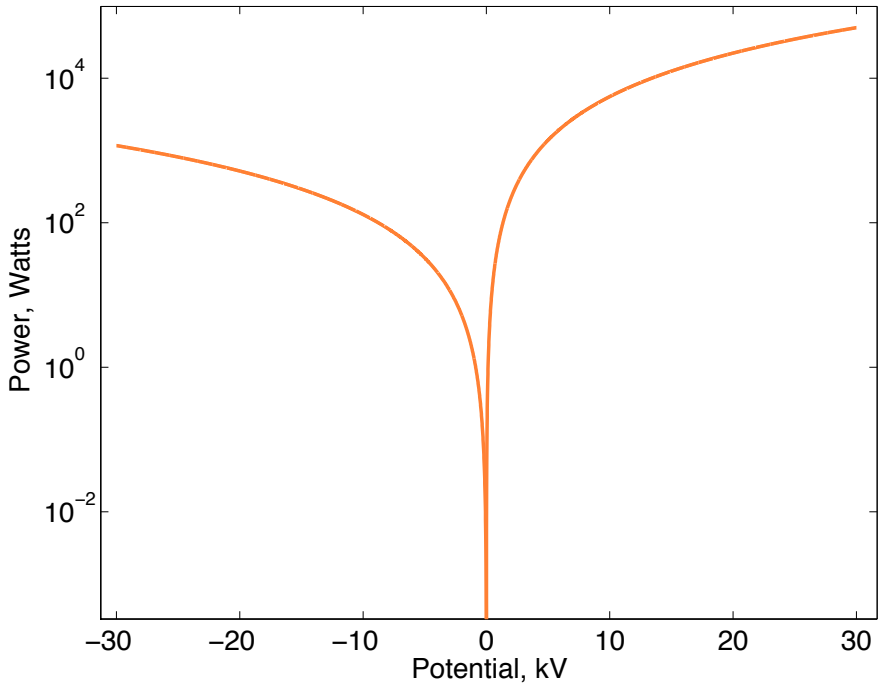

Figure 5.21: LEO Power requirements for maintaining a fixed potential using charge beam emission

5.4.3 Remote Charging Considerations

As a final consideration regarding the charging requirements for EIMS, a trade study is performed between beam current and beam energy for maintaining a potential using remote charging. Using Equation (5.9), the beam current and energy are varied to determine the resulting potential on the craft when equilibrium is reached. Here, GEO conditions are assumed for electron, ion, and photoelectron currents using Equations (5.2), (5.4), and (5.6).

The study shows that some combinations of current and energy are more advantageous than others. This is illustrated in the contour plot shown in Figure 5.22. Here, it is seen that there is a set of currents and energies which do not charge the membranes, although combination above and below can achieve high potentials. While it is likely that considerably high beam currents would be used than shown in the plot, it is important to recognize the trend when designing a laboratory or low current charging experiment.

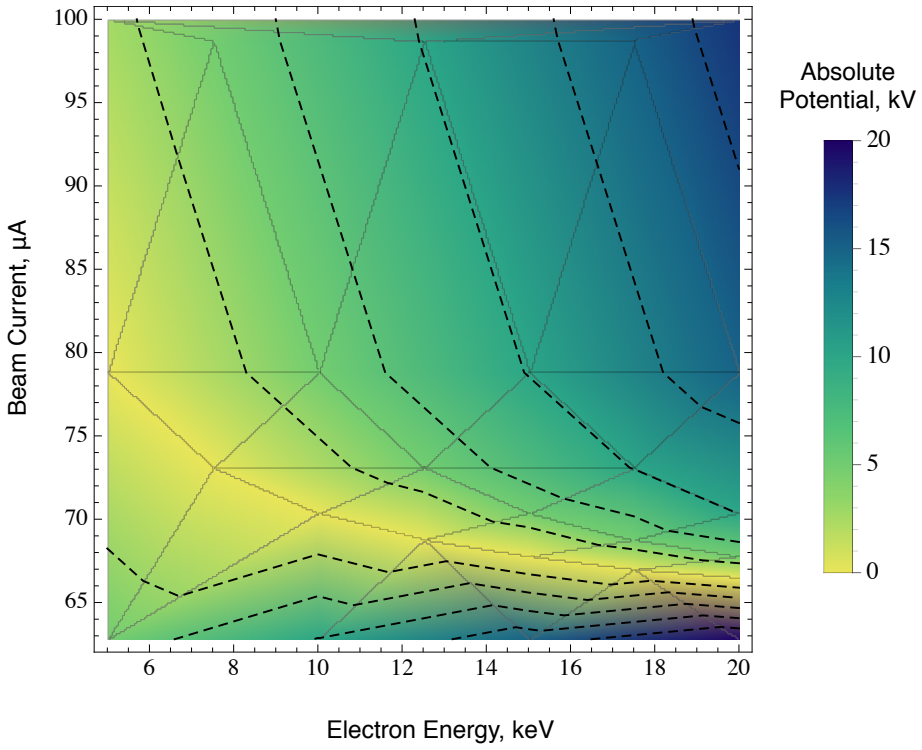

Figure 5.22: Trade study of current vs. beam energy for achieving potentials

Chapter 6

Conclusions

6.1 Summary of the Dissertation

This dissertation presents the concept of electrostatic inflation of membrane space structures. Although there has been brief mention in previous literature concerning the use of electrostatic forces for deployment purposes, there has not been extensive investigation. This research progressed the understanding of electrostatic inflation by identifying the biggest challenges, improving understanding of applications (e.g. non-precision structures), presenting and demonstrating concepts for feasible shapes, and furthering the understanding of plasma effects, charging methods, and power requirements. Some of the highlights from each chapter are summarized below.

In chapter 2, laboratory demonstrations in atmosphere and vacuum to show feasible concepts and demonstrate that electrostatic inflation can be used for deployment and shaping of membrane structures. Electrostatic inflation is easiest with smaller structures and membrane with cutouts which increase local charge densities.

Chapter 3 described some of the EIMS geometries considered (sphere, tube, 2-membrane sandwich) and explores the electrostatic solution of each with the 3D numerical software Maxwell 3D. A study of the required absolute potentials for EIMS to counteract membrane-normal compressive pressures from orbital perturbations is presented. First, the local charge density is related to the inflation pressure on the membrane. Voltage, however, is the parameter which is directly controlled on a spacecraft, therefore Maxwell 3D must be used to relate the charge density and the voltage.

Potentials on the membrane structures must be high enough to produce sufficient electrostatic pressures to counteract the differential pressures from gravity, solar radiation, and drag that would be experienced in orbit. In the geostationary orbit regime, the differential solar radiation pressure is the dominant perturbation. In low Earth orbit, atmospheric drag becomes dominant below approximately 500 km. Determination of differential orbital pressures allows for the calculation of the required charge densities for inflation. To determine the corresponding voltage requirements assuming the electrostatically inflated membrane structure is to maintain shape while experiencing orbital perturbations, 3D electrostatic solver software was used to numerically determine the electrostatic field solution. For a 1×1 m^2 structure in geostationary orbit, it was found that only hundreds of volts are needed to offset orbital perturbations. Active and even passive charging in geostationary orbits have far exceeded this number on several spacecraft. In LEO, potentials on the order of a few kilovolts are required. These determined potentials serve as a minimum to only offset disturbance pressures and larger values would be desirable to provide additional stiffness to the structure, especially during attitude maneuvers. Even these minimum values, however, are orders of magnitude smaller than what has been achieved on previous missions.

Chapter 4 addressed two issues related to EIMS in plasma: how does the plasma shield the electrostatic forces and does EIMS collapse or maintain shape in a charge flux. The plasma affects charged bodies through Deybe shielding, but the analytical Debye shielded force calculation is based on the assumption that the body has a low potential compared to the local plasma thermal energy. This assumption is quickly violated for charged craft in LEO and also in quiet GEO conditions. Numerical simulations allow for a more accurate solution to the forces and a modified 'effective' Debye length can be defined to allow quick use of the analytical equations. These effective Debye lengths are calculated for GEO and show that the effective Debye length can be several times larger than the classical Debye length for the electrostatic space applications. In LEO plasma conditions, the 'effective' Debye length can be more than an order of magnitude larger than the classically predicted Debye length. The LEO effective Debye lengths can therefore be up to the meter level, and the resulting Coulomb force improvement from reduced shielding may allow for LEO Coulomb

spacecraft applications such as inflation of membranes at cm level separations.

A vacuum chamber environment was used to perform experiments with a low-energy particle flow around various membrane structures. An interesting phenomena of structural vibrations was discovered between a charged membrane structure and a charged particle flow. A series of diagnostic tests were performed to eliminate sources of the vibrations, leading to a conclusion that the vibrations are caused by a coupling between the changing electrostatic fields surrounding the structure and the flow of electrons to and around the structure. Additionally, the application of EIMS for active radiation shielding is addressed and low-energy electron energy experiments are described. The EIMS structures are shown as efficient in shielding electrons nearly 99 percent of energy levels below or equal to structure charge levels.

In Chapter 5, two charging methods are explored for achieving desired potentials for EIMS: active charge emission and remote charging with an electron beam. To better understand the charging behavior, the secondary electron emission characteristics had to be determined for the metal coated polymers to be used for EIMS, as research has previous not addressed these specific material. The aim is to better understand which materials would be more advantageous to reach the desired potential levels required for electrostatic inflation of a membrane space structure. An experimental setup to measure the secondary electron yield for a material is described and results for secondary emission of aluminized Mylar and aluminized Kapton are presented. The two materials show similar trends and magnitudes, both following the approximate trend of a Sternglass curve and both show effects of oxidation from the interaction with the atmosphere.

Using the results from the secondary emission experiment, agreement was found between a simulation of remote charging in the vacuum chamber and experiment. Using an electron gun operating at 5 keV, charing was shown to approximately -550 V. The ion current from ionization in the chamber was shown to have a large impact on the charging.

Lastly, power requirements are explored for maintaining a fixed potential in a plasma. At GEO, power requirements are very reasonable at the milliwattt level, as the plasma has a small impact on charging. The photoelectron current is the dominate current to counteract in GEO.

In LEO, the dense plasma raises the power requirements to the Watt to hundreds of Watts for offsetting orbit perturbations. To reach potentials of tens of kiloVolts raises the requirement into the kiloWatt range, thus membrane stiffening should be considered as an alternative to maintaining constant inflationary pressure.

6.2 Recommended Future Work

There are many avenues for future work related to the concept of electrostatic inflation. Avenues exist in both fundamental research and practical investigation. Some of the recommended theoretical work includes:

- Finite element simulation of the multi-physics problem (electrostatic and structural). FEM can aid in understanding feasible shapes, as well as provide tools to study the effects of forces on torques on the inflated structure. Studying the structural response will enable quantifying required voltages to maintain an inflated structure that meets deflection requirements (may be mission dependent).
- 3D numerical plasma simulation to study the charging and charge flux effects on a charged membrane structure. One program which could be utilized is the VORPAL product from TechX.
- Quantification of required pressures for maintaining shape through an attitude maneuver.
- Study the effect of material thickness and thickness of the aluminum deposition layer on secondary electron emission and determine the most advantageous materials for EIMS.
- Understanding the dynamics of an EIMS system. Determine natural frequency of different configurations of an EIMS system and simulate the dynamics to understand control requirements.

Some of the recommended work that is necessary for practical application of EIMS are as follows:

- Investigate the packaging and deployment problem. Packaging must consider the effects of wrinkles on the membranes and how storage during launch will affect the deployment and shape.
- Determine specific mission scenarios in which EIMS can be a useful technology.
- Zero gravity flight experiment to study deployment and dynamics.

Bibliography

[1] Cover, J. H., Knauer, W., and Maurer, H. A., "Lightweight Reflecting Structures Utilizing Electrostatic Inflation," US Patent 3,546,706, October 1966.

[2] Gettliffe, G. V. and Inamdar, N. K., "High-Temperature Superconductors as Electromagnetic Deployment and Support Structures in Spacecraft," Tech. rep., Massachusetts Institute of Technology, Space Systems Lab, Oct. 2012.

[3] Straubel, M., Block, J., Sinapius, M., and Hühne, C., Deployable Composite Booms for Various Gossamer Space Structures, American Institute of Aeronautics and Astronautics, 2013/06/18 2011.

[4] Banik, J. A. and Murphy, T. W., "Synchronous Deployed Solar Sail Subsystem Design Concept," No. AIAA-2007-1837, 47th AIAA Structures, Dynamics, and Mechanics of Materials Conference, 2007.

[5] Cadogan, D. P., Lin, J. K., and Grahne, M. S., "Inflatable Solar Array Technology," No. AIAA-99-1075, 37t hAIAAAerospaceSciences Meeting and Exhibit, 1999.

[6] Cadogan, D. P., Stein, J., and Grahne, M. S., "Inflatable Composite Habitat Structures for Lunar and Mars Exploration," Acta Astronautica, Vol. 44, 1999, pp. 399–406.

[7] Freeland, R. E., Bilyeu, G. D., , Veal, G. R., and Mikulas, M. M., "Inflatable Deployable Space Structures Technology Summary," 49th International Astronautical Congress, Melbourne, Australia, Sept. 28 – Oct. 2 1998.

[8] Freeland, R. E., Bilyeu, G. D., Veal, G. R., Steiner, M. D., and Carson, D. E., "Large Inflatable Deployable Antenna Flight Experiment Results," Acta Astronautica, Vol. 41, No. 4–10, 1997, pp. 267–277.

[9] Jenkins, C. H. M., editor, Gossamer Spacecraft: Membrane and Inflatable Structures Technology for Space Applications, Vol. 191 of Progress in Astronautics and Aeronautics, American Institute of Aeronautics and Astronautics, 2001.

[10] Tripathi, R. K., Wilson, J. W., and Youngquist, R. C., "Electrostatic space radiation shielding," Advances in Space Research, Vol. 42, No. 6, 2008, pp. 1043–1049.

[11] Wertz, J. R. and Larson, W. J., Space Mission Analysis and Design, Kluwer Academic Publishers, Dordrecht, The Netherlands, 1991.

[12] "Space Transportation Costs: Trends in Price Per Pound to Orbit Space Transportation Costs: Trends in Price Per Pound to Orbit 1990-2000," 2002.

[13] Johnston, J. and Parrish, K., "Thermal-Structural Analysis of Sunshield Membranes," AIAA Gossamer Systems Forum, April 2003.

[14] Space Exploration Technologies, Falcon 9 Launch Vehicle Payload User's Guide, 1st ed., 2009.

[15] United Launch Alliance, Atlas V Launch Services User's Guide, March 2010.

[16] Wang, C., Du, X., Tan, H., and He, X., "A new computational method for wrinkling analysis of gossamer space structures," International Journal of Solids and Structures, Vol. 46, No. 6, 2009, pp. 1516 – 1526.

[17] Felippa, C. A., "Advance Finite Elements for Solids, Plates, and Shells," .

[18] Wertz, J., Spacecraft Attitude Determination and Control, D. Reidel Publishing Company, 1978.

[19] Olson, G., Murphey, T., and Thomas, G., Free Deployment Dynamics of a Z-Folded Solar Array, American Institute of Aeronautics and Astronautics, 2013/06/19 2011.

[20] Bittencourt, J. A., Fundamentals of Plasma Physics, Springer, 3rd ed., 2004.

[21] Verne, J., From the Earth to the Moon, 1865.

[22] Johnson, L. and et. al, "NanoSail-D: A solar sail demonstration mission," Acta Astronautica, Vol. 68, 2011, pp. 571–575.

[23] Furuya, H., Mori, O., Sawada, H., Okuizum, N., Shirasawa, Y., Natori, M., Miyazaki, Y., and Matunaga, S., Manufacturing and Folding of Solar Sail 'IKAROS', American Institute of Aeronautics and Astronautics, 2013/06/11 2011.

[24] Shirasawa, Y., Mori, O., Miyazaki, Y., Sakamoto, H., Hasome, M., Okuizumi, N., Sawada, H., Furuya, H., Matsunaga, S., Natori, M., and Kawaguchi, J., Analysis of Membrane Dynamics using Multi-Particle Model for Solar Sail Demonstrator "IKAROS", American Institute of Aeronautics and Astronautics, 2013/06/11 2011.

[25] "Peageo Satellite to Girdle Globe for Earth Mapping," NASA News Release 66N32083, NASA, June 1966.

[26] "Preliminary Mission Report: Spartan 207/Inflatable Antenna Experiment Flown on STS-77," Tech. rep., NASA Goddard Space Flight Center, Feb. 1997.

[27] Nock, K. T., Aaron, K. M., and McKnight, D., "Removing Orbital Debris with Less Risk," Journal of Spacecraft and Rockets, Vol. 50, No. 2, 2013/06/11 2013, pp. 365–379.

[28] Nock, K., Gates, K., Aaron, K., and McRonald, A., Gossamer Orbit Lowering Device (GOLD) for Safe and Efficient De-Orbit, American Institute of Aeronautics and Astronautics, 2013/06/11 2010.

[29] Nock, K. T., McRonald, A. D., and Aaron, K. M., "Balloon device for lowering space object orbits," United States Patent, Dec. 2004, Patent No. 6,830,222.

[30] MacEwen, H. A., editor, Stretched Membrane with Electrostatic Curvature (SMEC) Mirrors, Vol. 4849. SPIE, December 2002.

[31] King, L. B., Parker, G. G., Deshmukh, S., and Chong, J.-H., "Spacecraft Formation-Flying using Inter-Vehicle Coulomb Forces," Tech. rep., NASA/NIAC, January 2002.

[32] Schaub, H., Parker, G. G., and King, L. B., "Challenges and Prospect of Coulomb Formations," Journal of the Astronautical Sciences, Vol. 52, No. 1–2, Jan.–June 2004, pp. 169–193.

[33] Berryman, J. and Schaub, H., "Analytical Charge Analysis for 2- and 3-Craft Coulomb Formations," AIAA Journal of Guidance, Control, and Dynamics, Vol. 30, No. 6, Nov.–Dec. 2007, pp. 1701–1710.

[34] Schaub, H., Hall, C., and Berryman, J., "Necessary Conditions for Circularly-Restricted Static Coulomb Formations," Journal of the Astronautical Sciences, Vol. 54, No. 3–4, July-Dec. 2006, pp. 525–541.

[35] Natarajan, A. and Schaub, H., "Linear Dynamics and Stability Analysis of a Coulomb Tether Formation," AIAA Journal of Guidance, Control, and Dynamics, Vol. 29, No. 4, July–Aug. 2006, pp. 831–839.

[36] Wang, S. and Schaub, H., "Switched Lyapunov Function Based Coulomb Control of a Triangular 3-Vehicle Cluster," AAS/AIAA Astrodynamics Specialist Conference, Pittsburgh, PA, Aug. 9–13 2009.

[37] Seubert, C. R. and Schaub, H., "Tethered Coulomb Structures: Prospects and Challenges," Journal of the Astronautical Sciences, Vol. 57, No. 1-2, Jan.–June 2009, pp. 347–368.

[38] Seubert, C. R., Panosian, S., and Schaub, H., "Dynamic Feasibility Study of a Tethered Coulomb Structure," AAS/AIAA Astrodynamics Specialist Conference, Toronto, Canada, Aug. 2–5 2010, AIAA-2010-8131.

[39] Schaub, H. and Moorer, D. F., "Geosynchronous Large Debris Reorbiter: Challengs and Prospects," AAS Kyle T. Alfriend Astrodynamics Symposium, Monterey, CA, May 17–19 2010.

[40] Daniel F. Moorer, J. and Schaub, H., "Electrostatic Spacecraft Reorbiter," United States Patent, 2012, US 8,205,838.

[41] McPherson, D. A., Cauffman, D. P., and Schober, W., "Spacecraft Charging at High Altitudes - The SCATHA Satellite Program," AIAA Aerospace Sciences Meeting, Pasadena, CA, Jan. 20–22 1975.

[42] Mullen, E. G., Gussenhoven, M. S., Hardy, D. A., Aggson, T. A., and Ledley, B. G., "SCATHA Survey of High-Voltage Spacecraft Charging in Sunlight," Journal of the Geophysical Sciences, Vol. 91, No. A2, 1986, pp. 1474–1490.

[43] Olsen, R. C., "Record Charging Events from Applied Technology Satellite 6," J. Spacecraft, Vol. 24, No. 4, 1986, pp. 362–366.

[44] Katz, I., "Structure of the Bipolar Plasma Sheath Generated by SPEAR I," Journal of Geophysical Research, Vol. 94, No. A2, Feb. 1989, pp. 1450–1458.

[45] King, L. B., Parker, G. G., Deshmukh, S., and Chong, J.-H., "Study of Interspacecraft Coulomb Forces and Implications for Formation Flying," AIAA Journal of Propulsion and Power, Vol. 19, No. 3, May–June 2003, pp. 497–505.

[46] Kong, E. M. C., Kwon, D. W., Schweighart, S. A., Elias, L. M., Sedwick, R. J., and Miller, D. W., "Electromagnetic Formation Flight for Multisatellite Arrays," AIAA Journal of Spacecraft and Rockets, Vol. 41, No. 4, July–Aug. 2004, pp. 659–666.

[47] Benford, J., "Deployment of Ultralightweight Sails," Tech. rep., Microwave Sciences, April 2002.

[48] Lieberman, M. A. and Lichtenberg, A. J., Principles of Plasma Discharges and Materials Processing, John Wiley & Sons, 2005.

[49] Ansoft, User's Guide: Maxwell 3D, 11th ed., Jan. 2010.

[50] Leipold, M., Runge, H., and Sickinger, C., "Large SAR membrane antennas with lightweight deployable booms," 28th ESA Workshop on Space Antenna Systems and Technologies, 2005.

[51] Landau, L. D. and Lifshitz, E. M., Electrodynamics of Continuous Media, Vol. 8 of Course of Theoretical Physics, Addison-Wesley Publishing Company, Inc., 1960.

[52] Seubert, C. R. and Schaub, H., "Tethered Coulomb Structures: Prospects and Challenges," AAS F. Landis Markley Astrodynamics Symposium, Cambridge, MA, June 30 – July 2 2008, Paper AAS 08–269.

[53] Vallado, D. A., Fundamentals of Astrodynamics and Applications, Space Technology Library, Springer, 3rd ed., 2007.

[54] van, A. L. and Wielgosz, C., "Bending and buckling of inflatable beams: some new theoretical results," Thin-Walled Structures, Vol. 44, Mar. 2005, pp. 1166–1187.

[55] Gurnett, D. and Bhattacharjee, A., Introduction to Plasma Physics, Cambridge University Press, 2005.

[56] Garrett, H. B. and DeForest, S. E., "An Analytical Simulation of the Geosynchronous Plasma Environment," Planetary Space Science, Vol. 27, 1979, pp. 1101–1109.

[57] Lennartsson, W. and Reasoner, D. L., "Low-Energy Plasma Observations at Synchronous Orbit," Journal of Geophysical Research, Vol. 83, No. A5, 1978, pp. 2145–2156.

[58] Hastings, D. E. and Garrett, H. B., Spacecraft-Environment Interactions, Cambridge University Press, 1996.

[59] Stiles, L. A. and Seubert, C. R., "Effective Coulomb Force Modeling in a Space Environment," AAS/AIAA Astrodynamics Specialist Conference, Charleston, SC, Jan 31–Feb 2 2012.

[60] Pierrard, V., Goldstein, J., André, N., Jordanova, V., Kotova, G., Lemaire, J., Liemohn, M., and Matsui, H., "Recent Progress in Physics-Based Models of the Plasmasphere," Space Science Reviews, Vol. 145, No. 1, 05 2009, pp. 193–229.

[61] Thomsen, M. F., Denton, M. H., Lavraud, B., and Bodeau, M., "Statistics of plasma fluxes at geosynchronous orbit over more than a full solar cycle," Space Weather, Vol. 5, No. 3, 03 2007.

[62] Herr, J. L. and McCollum, M. B., "Spacecraft Environments Interactions: Protecting Against the Effects of Spacecraft Charging," Reference Publication 1354, NASA Marshall Space Flight Center, Nov. 1994.

[63] Murdoch, N., Izzo, D., Bombardelli, C., Carnelli, I., Hilgers, A., and Rodgers, D., "Electrostatic Tractor for Near Earth Object Deflection," 59th International Astronautical Congress, Glasgow, Scotland, 2008, Paper IAC-08-A3.I.5.

[64] Spillantini, P., Casolino, M., Durante, M., Mueller-Mellin, R., Reitz, G., Rossi, L., Shurshakov, V., and Sorbi, M., "Shielding from cosmic radiation for interplanetary missions: Active and passive methods," Radiation Measurements, Vol. 42, No. 1, 2007, pp. 14 – 23.

[65] Townsend, L. W., "Overview of active methods for shielding spacecraft from energetic space radiation," Physica Medica, Vol. 17, 2001, pp. 84–85.

[66] Whipple, E. C. and Olsen, R. C., "Importance of differential charging for controlling both natural and induced vehicle potentials on ATS-5 and ATS-6," Proceedings of the 3rd Spacecraft Charging Technology Conference, Nov. 12–14 1980, p. 887, NASA Conference Publication 2182.

[67] Sternglass, E. J., "Theory of Secondary Electron Emission by High-Speed Ions," Phys. Rev., Vol. 108, Oct 1957, pp. 1–12.

[68] Jonker, J. H., "On the Theory of Secondary Electron Emission," Philips Res. Rep. 7, 1952.

[69] Draine, B. T. and Salpeter, E. E., "Destruction mechanisms for interstellar dust," Astrophysical Journal, Vol. 231, July 1979, pp. 438–455.

[70] Lai, S. T., "An overview of electron and ion beam effects in charging and discharging of spacecraft," IEEE Transactions on Nuclear Science, Vol. 36, No. 6, Dec. 1989, pp. 2027–2032.

[71] Lai, S. T., Fundamentals of Spacecraft Charging, Princton University Press, 2012.

[72] Schaub, Hanspeter; Moorer, D. F., "Geosynchronous Large Debris Reorbiter: Challenges and Prospects," AAS Kyle T. Alfriend Astrodynamics Symposium, Monterey, California, May 2010.

[73] Insepov, Z., Ivanov, V., Jokela, S., Veryovkin, I., Zinovev, A., and Frisch, H., "Comparison of secondary electron emission simulation to experiment," Nuclear Instruments and Methods in Physics Research A, 2010, pp. 155–157.

[74] Sternovsky, Z., Elementary Processes in Dusty Plasmas, Ph.D. thesis, Charles University, 2001.

[75] Willis, R. F. and Skinner, D. K., "Secondary Electron Emission Yield Behaviour of Polymers," Solid State Communications, Vol. 13, 1973, pp. 685–688.

[76] Jeoung, J.-M., Lim, J.-Y., Kim, Y.-G., Seo, Y., Cho, G.-S., and Choi, E.-H., "Influence of Vacuum-Annealing Process on the Secondary Electron Emission Coefficient (γ) from a MgO Protective Layer," Japanese Journal of Applied Physics, Vol. 40, No. Part 1, No. 3A, 2001, pp. 1433–1434.

[77] Laikhtman, A. and Hoffman, A., "Enhancement of secondary electron emission by annealing and microwave hydrogen plasma treatment of ion-beam-damaged diamond films," Journal of Applied Physics, Vol. 91, No. 4, 2002, pp. 2481–2486.

[78] McDaniel, E. W., Collision Phenomena in Ionized Gases, John Wiley & Sons, Inc., 1964.

[79] Kim, Y. and et. al, Electron-Impact Cross Sections for Ionization and Excitation, National Institue of Standards and Technology, Aug. 1997.

[80] Clark, C. S. and Mazarias, A. L., "Power System Challenges For Small Satellite Missions," European Small Satellite Services Symposium, Sardinia, 2006.